Universität Bonn

Physikalisches Institut

First Conceptual Design and Studies for a Tracking Time Projection Chamber for the Belle II Experiment

Andreas Löschcke Centeno

Acknowledgements

Contents

Introduction

This thesis deals with simulating a tracking time projection chamber (TPC) for the Belle II experiment at the SuperKEKB accelerator and using the simulation for first studies.

The tracker for the Belle II experiment, the Central Drift Chamber (CDC), suffers from high occupancy due to large beam backgrounds. While at the current luminosity of the SuperKEKB accelerator the operation of the drift chamber is still possible, there is a possibility that the CDC performance will be inadequate at full design luminosity. Therefore, an upgrade of the tracking system of Belle II is developed as a contingency.

This project includes a TPC in the upgrade proposal as a replacement tracker for the CDC. In order to study the properties of a TPC operating in the Belle II experiment, the TPC is simulated within the Belle II software and analysis framework. Using this simulation the conditions for tracking can be investigated. Additionally, some of the physics benchmarks for the TPC are tested. Since the TPC cannot provide all the functions of the CDC, alternative solutions have to be proposed.

This thesis is a proof-of-concept for a tracking TPC for the Belle II experiment.

The Standard Model of Particle Physics

The Standard Model (SM) of particle physics is a description of the elementary particles of the Universe and the fundamental forces acting between them [1]. The particles can be classified in two categories: fermions and bosons. An overview of the elementary particles in the SM can be seen Figure 2.1.

Figure 2.1: Elementary particles from the Standard Model of particle physics [1]

2.1 Fermions

In total there are twelve fermions with each fermion having a corresponding antiparticle [1]. The fermions are half-integer spin particles and make up the visible matter in the Universe. The elementary fermions can be divided into quarks and leptons, depending on which forces they interact with.

Quarks

There are six known quarks (up, down, charm, strange, top, bottom) which come in three generations. In contrast to leptons, the quarks carry color charge and therefore interact via the strong interaction. Under the strong interaction the quarks form hadrons either as pairs of three, then called baryons, or as pair of quark-antiquark, then called a meson. Examples for baryons include proton and neutron, while examples for mesons include pions, B mesons, and the $\Upsilon(4S)$.

The quarks also carry electrical and weak charge and therefore interact via electromagnetism and the weak force [1]. Each generation of quarks comes with one quark with electrical charge of $+\frac{2}{3}$ in units of the elementary charge, and one quark with electrical charge of $-\frac{1}{3}$.

Leptons

As with the quarks, there are six known leptons which come in three generations [1]. In each generation there is one lepton which has an electric charge of -1 (electron, muon, tau) which thus interacts via the electromagnetic force, and one lepton which is electrically neutral, called neutrino, which thus does not interact via electromagnetism. Since the leptons do not carry color charge, the neutrino only interacts via the weak interaction making it extremely difficult to detect. With increasing generations the mass of the charged leptons increases, as is the case for the quarks. This means that only the fermions from the first generation are stable since the heavier fermions will decay into lighter particles. While the exact masses of the neutrinos are not yet determined, it is known that they are not massless due to the observed effect of neutrino oscillation. The neutrinos do not decay, but instead oscillate between their flavors.

2.2 Bosons

The elementary bosons in the SM are for the most part the gauge bosons of the fundamental forces which have a spin of 1 [1]. The gluon carries the interaction of the strong force, the photon is the force carrier for electromagnetism and the $W^{\pm}$ and Z^0 bosons are the force carriers for the weak force. Each force interacts with particles which are charged with respect to this force. For example, the photon, massless carrier of the electromagnetic force, only couples to particles which carry electric charge. In total eight gluons, which differ in their color charge, mediates the strong force which binds gluons together to form hadrons. The W^+, W^-, and the Z^0 bosons are massive particles which carry the interaction of the weak force. Due to their mass this interaction is only short ranged, hence the name weak force.

The Higgs boson with a spin of 0 is not a force carrier in the Standard Model, but instead is viewed as an excitation of the Higgs field which is responsible for giving the other elementary particles their masses [1].

Interactions of Charged Particles with Matter

Charged particles traversing a medium will lose some of their energy to the medium along their trajectory [2]. There are different effects of energy loss taking place, depending on the mass and energy of the particle. Generally, for particles heavier than the electron the dominant contribution for energy loss is ionization and excitation of the atoms in the medium in the mid-energy range and bremsstrahlung in the high-energy range.

The mean energy loss per track length $\langle \frac{dE}{dx} \rangle$ due to ionization and excitation can be described with the Bethe-Bloch formula (Equation 3.1). The variables are explained in detail in [2]. Figure 3.1 shows the mass stopping power, defined as $\langle -\frac{dE}{dx} \rangle$, as function of $\beta\gamma$ where $\beta = \sqrt{1 - \frac{1}{\gamma^2}}$ and $\gamma = \frac{E}{m}$ are the Lorentz factors, for a μ^+ traversing copper. The region described by Equation 3.1 starts at around $\beta\gamma \sim 0.1$ and ends at $\beta\gamma \sim 1000$. When plotting the mass stopping power against $\beta\gamma$ instead of the particles momentum, the behavior of the curve is largely independent of particle mass and is therefore similar for all heavy charged particles [2, 3].

$$-\left\langle \frac{dE}{dx} \right\rangle = K \frac{Z}{A} \rho \frac{z^2}{\beta^2} \left[\frac{1}{2} \ln \frac{2m_e c^2 \beta^2 \gamma^2 W_{max}}{I^2} - \beta^2 - \frac{\delta(\beta\gamma)}{2} \right] \qquad (3.1)$$

At $\beta\gamma \sim 3$–3.5 the curve reaches a minimum. A particle at that energy will lose a minimal amount of energy to the medium [3]. Since the Bethe-Bloch curve reaches a plateau of similar stopping power value at higher $\beta\gamma$, all charged particles with $\beta\gamma \geq 3$ are considered to be a Minimum Ionizing Particle (MIP) up to a $\beta\gamma$ where radiative effects need to be taken into account. Below this point, particles with low energy will lose their energy very quickly. This is responsible for the Bragg peak, where particles at the end of the trajectory deposit large amounts of energy in the medium.

In a typical particle collider with several GeV center-of-mass energy usually all charged particles long lived enough to reach the detectors are considered to be MIPs, except electrons since they are light enough that at typical collider energies that radiative losses need to be taken into account.

Since the energy loss is dependent on the particle mass, it can be used to identify different particles [3]. The plot in Figure 3.2 shows the measurement of dE/dx vs. the particle momentum from the ALICE experiment for different particles as a heat map. One can see that for some momentum regions particles like protons (p), electrons (e), pions (π), and kaons (K) can be separated quite well. The measurement of dE/dx is therefore a powerful tool for particle identification.
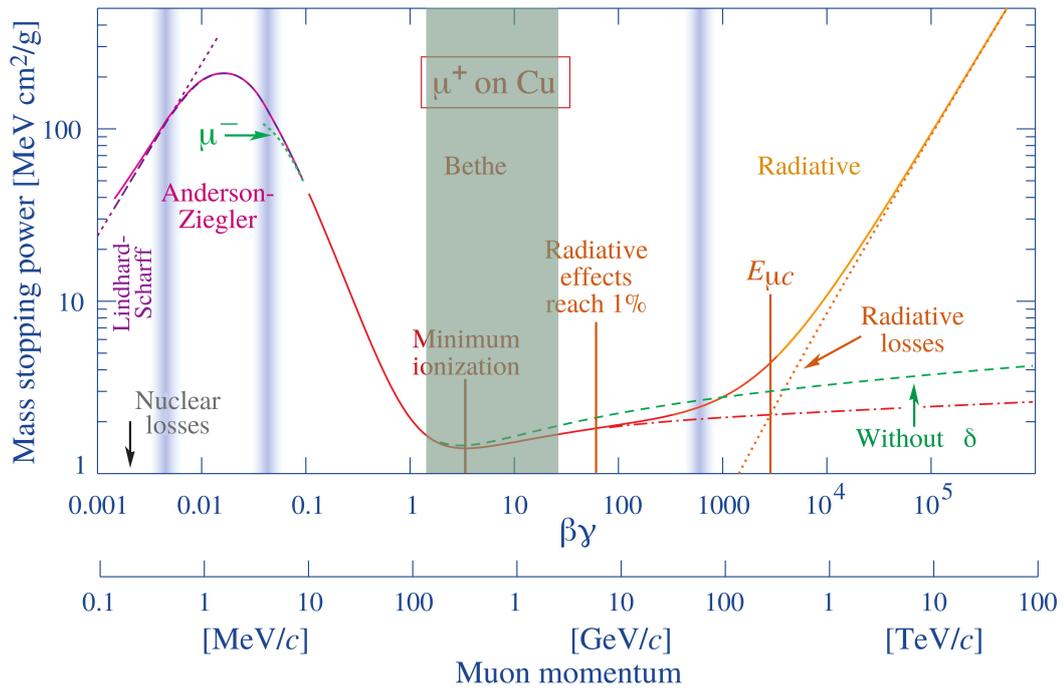
Figure 3.1: Mass stopping power for μ^+ in copper [2]. Particles are considered to be minimally ionizing at $\beta\gamma \geq 3$ up to $\beta\gamma \sim 1000$. Highlighted in green is the expected momentum range for pions in Belle II which are the most common charged particle from $\Upsilon(4S)$ events [4].
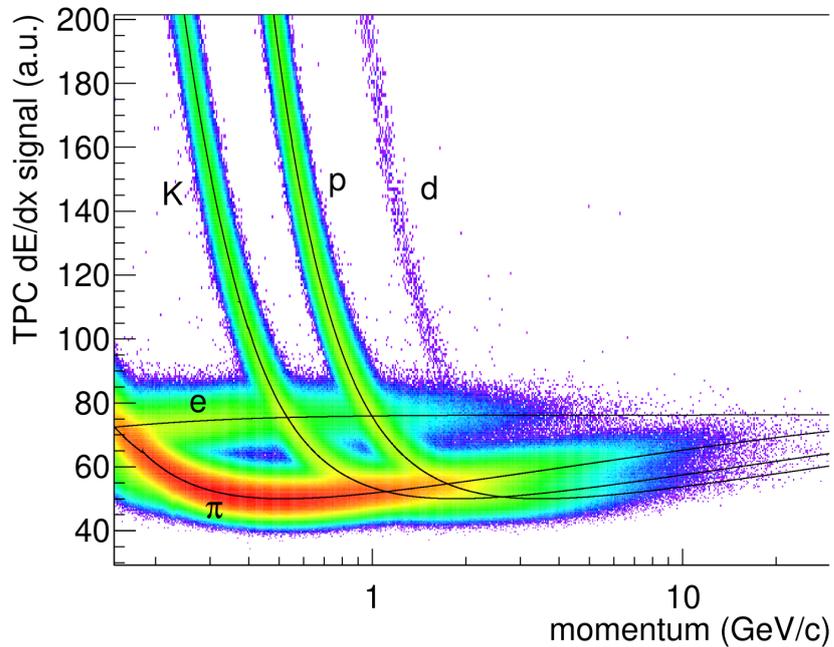
Figure 3.2: Measurement of dE/dx vs. momentum for different particles [5]. Depending on the momentum region, this information can be used to for particle identification. This signal only incorporates the energy loss from ionization and not from radiation.

Charged Particles in a Magnetic Field

When the momentum of a charged particle in a magnetic field has a component perpendicular to the magnetic field flux the Lorentz force acts on the particle, as illustrated in Figure 4.1 [6]. Due to this force the particle will perform a circular motion in the plane perpendicular to the magnetic field. The magnetic field is used in tracking detectors to measure momentum, and in some gaseous detectors to reduce diffusion.
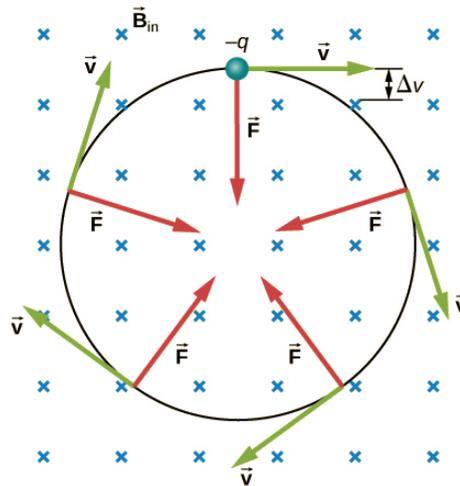
Figure 4.1: Lorentz force acting on a charged particle in a magnetic field [7]

4.1 Momentum Measurement

The circular motion of a charged particle can be used to determine the momentum transverse to the magnetic field [6]. This can be done by equating the Lorentz force to the centrifugal force in the case where the velocity (or the corresponding velocity component) is perpendicular to direction of the magnetic field,

$$qvB = \frac{\gamma m v^2}{r}, \tag{4.1}$$

where q is the particle charge, v the particle velocity, B the magnetic flux density, γ the Lorentz factor for the particle, m the particle mass and r the curvature of the trajectory. The particles momentum transverse to the field can then be obtained via

$$p_T = \gamma m v = qBr \tag{4.2}$$

Equation 4.2 can also be written as

$$p_T(\text{GeV}\,c^{-1}) = 0.3B(\text{T})r(\text{m}), \tag{4.3}$$

when using the given units.

If in a detector at a particle collider the magnetic field is aligned with the beam axis, the momentum transverse to the field is also the transverse momentum for the particle in the event.

The resolution on the transverse momentum σ_{p_T} then depends in large part on the accuracy with which the curvature of the track is reconstructed, which in term depends on the spatial resolution $\sigma_{r\phi}$ of the detector [3]. It can be shown that for a large number of measurement points N which are evenly distributed, the relative p_T resolution can be calculated via Equation 4.4, known as Gluckstern equation.

$$\left(\frac{\sigma_{p_T}}{p_T}\right)_{\text{meas}} = \frac{p_T}{0.3|z|} \frac{\sigma_{r\phi}}{L^2 B} \sqrt{\frac{720}{N+4}}, \qquad [p_T] = \text{GeV}\,c^{-1}, [L] = \text{m}, [B] = \text{T} \tag{4.4}$$

Here, z is the electric charge of the particle in units of the elementary charge and L is the length of the path in the detector, which is also referred to as "lever arm". From this it can be seen that in order to achieve a good p_T resolution one needs a good spatial resolution in order to reconstruct the track precisely for the fit of the curvature.

A strong magnetic field and a long lever arm, which enters quadratically, also help in improving the p_T resolution. This is due to the fact that a stronger curvature from the magnetic field and a longer curved track significantly improve the result of the curvature fit. For the same reason does relative momentum resolution rise with p_T. For large p_T values the track becomes straighter such it becomes increasingly difficult to correctly determine the curvature.

However, this is not the only term contributing to the overall p_T resolution. Due to multiple scattering of the primary particle the sagitta of the track which is used for reconstruction of the curvature is slightly altered [3]. It can be shown that for $\beta = \frac{v}{c} \approx 1$ the contribution of multiple scattering is approximately constant.

The total p_T resolution is then obtained by quadratically adding the two contributions:

$$\frac{\sigma_{p_T}}{p_T} = \sqrt{\left(\frac{\sigma_{p_T}}{p_T}\right)_{\text{meas}}^2 + \left(\frac{\sigma_{p_T}}{p_T}\right)_{\text{scat}}^2}. \tag{4.5}$$

Figure 4.2 shows the contribution of each effect to the total p_T resolution. For low p_T the constant multiple scattering term dominates over the position measurement, whereas the position measurement contribution causes a linear rise with p_T. Figure 4.2 also includes another contribution for low p_T particles. This contribution becomes relevant if the particle barely reaches into the detector. In that case the number of measurement points is reduced which makes determining the momentum more

difficult. In addition, the relative error in the spatial resolution becomes larger, leading to an increase in σ_{p_T}/p_T. This contribution is referred to as "reduced lever arm".
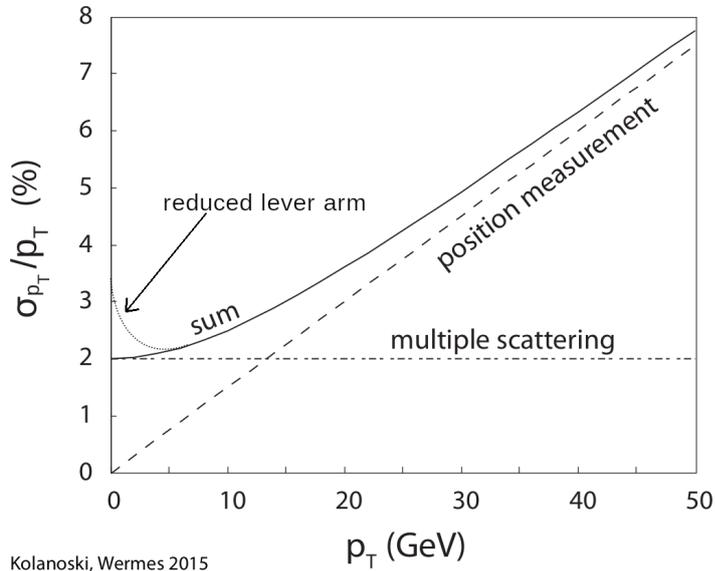
Figure 4.2: Contributions to the p_T resolution [3]. Multiple scattering contributes a constant term, while the position measurement adds a rise for p_T. Additional contribution from reduced lever arm at very low p_T

4.2 Diffusion

Diffusion describes the thermal motion of a particle or a group of particles which is statistical in nature, resulting in the spread of the particles [8]. For some gaseous detectors the diffusion of electrons from the ionization of the primary particle in the gaseous medium plays an important role.

When an electron drifts through a gas, it will change its direction periodically due to scattering with the gas molecules, which is an effect of diffusion [3]. Generally, diffusion is an unwanted effect since it makes it difficult to reconstruct the precise origin of the particle drifting through the gas. The displacement of the electrons with respect to their original position can be quantified by a diffusion coefficient which describes the spread of particles per time and strongly depends on the gas and under which conditions the gas is operated, like temperature, pressure and the electrical drift field.

If the drift direction of the particle coincides with the direction of the magnetic field, the diffusion can be suppressed. This principle is illustrated in Figure 4.3. In general, the particle stays closer to the original coordinates due to the fact that it is forced onto a circular motion by the magnetic field [6]. Therefore, for detectors that rely on the drift of electrons, it is desirable to have the drift direction aligned with the magnetic field.
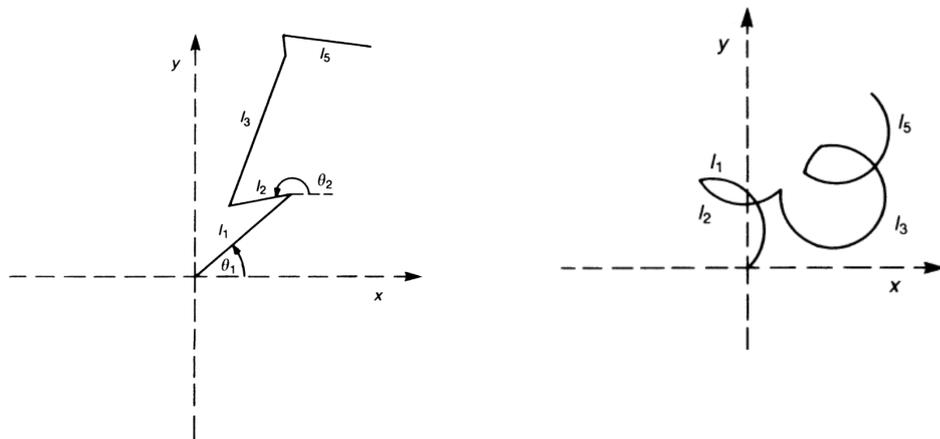
(a) Diffusion with no magnetic field in z direction

(b) Diffusion with a magnetic field in z direction

Figure 4.3: Due to the magnetic field the particle stays closer to its origin after scattering. [6]

SuperKEKB and the Belle II Experiment

The Belle II experiment is situated at the SuperKEKB accelerator in Tsukuba, Japan [9]. Belle II is the successor of the Belle experiment, which ran at the predecessor of the SuperKEKB accelerator, KEKB.
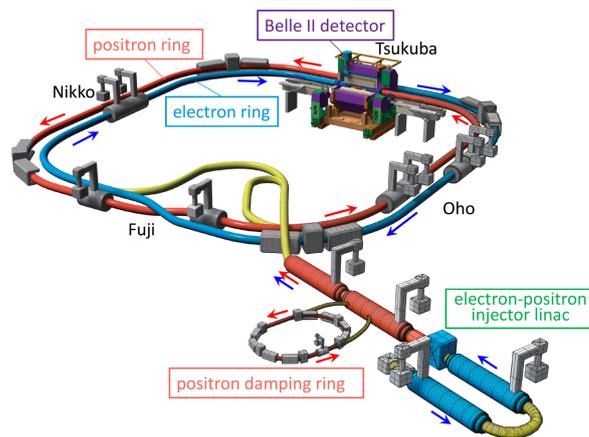
Figure 5.1: Schematic design of the SuperKEKB accelerator [10]

5.1 SuperKEKB

The SuperKEKB accelerator is the upgrade of the *B*-factory KEKB, where *B* mesons are produced at high luminosities. This is achieved by colliding electrons and positrons beams with asymmetric energies at a center-of-mass energy around the mass of the $\Upsilon(4S)$ resonance, which is a bound state of a $b\bar{b}$ quark pair [10]. Subsequently, the $\Upsilon(4S)$ decays into two *B* mesons nearly at rest in the laboratory frame [9]. The beam energies are 7 GeV for the electrons and 4 GeV for the positrons, leading to a boost of the center-of-mass system, allowing for studies of time-dependent charge-parity symmetry violation.

The current design luminosity for the SuperKEKB accelerator is $\mathscr{L} = 6.5 \times 10^{35}\,\mathrm{cm}^{-2}\,\mathrm{s}^{-1}$, thus pushing the luminosity frontier [11]. The SuperKEKB accelerator currently holds the record for the highest instantaneous luminosity of $2.4 \times 10^{34}\,\mathrm{cm}^{-2}\,\mathrm{s}^{-1}$ [12]. Figure 5.1 shows a schematic view of the

SuperKEKB accelerator. It consists of a low-energy ring (LER) for the positrons and a high-energy ring (HER) for the electrons [10]. The Belle II detector is located at the collision point of the beams.

5.2 Belle II Detector

The design of the Belle II detector is illustrated in Figure 5.2 alongside the coordinate system which is used for the detector in this thesis. It is a general purpose spectrometer with the goal of collecting $50\,ab^{-1}$ of integrated luminosity [13]. An overview of the detector's sub-components is given in the following.
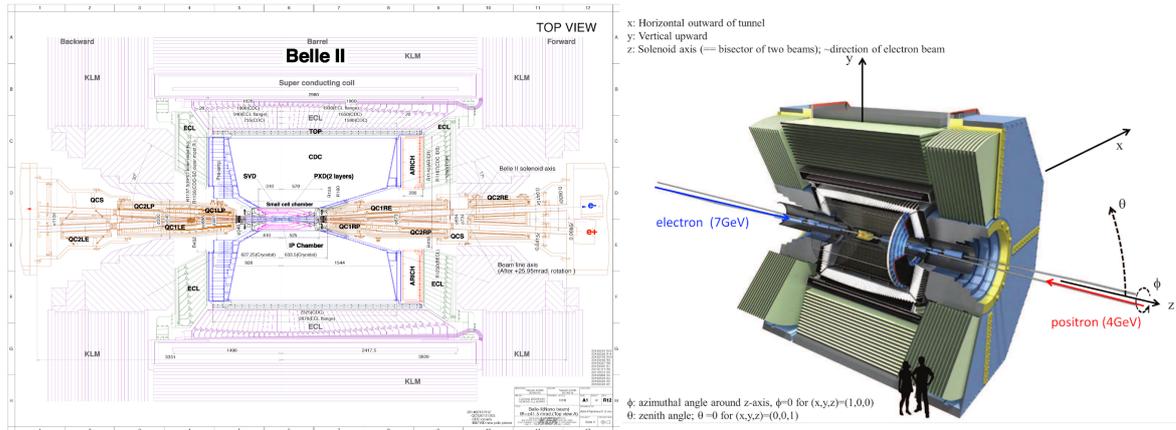
Figure 5.2: Left: technical drawing of Belle II detector design with focusing quadrupoles [14]
Right: Coordinate system of Belle II detector. The interaction point marks the origin of this coordinate system. [15]

PXD

The innermost detector is the pixel detector (PXD) [16]. It consists of two layer of silicon pixel sensors, based on DEPFET technology. This allows for very thin detectors down to $50\,\mu m$ which reduces multiple scattering. The PXD is part of the vertex detector alongside the SVD, which is the following sub-detector. Due to the high luminosity of the SuperKEKB accelerator the innermost vertex detector cannot be realized with strips due to high occupancy. Therefore, for the innermost detector two layers of pixel sensors were chosen at radii of $14\,mm$ and $22\,mm$ in the coordinate system defined in Figure 5.2. The layers consists of several "ladders" consisting of two sensors which are arranged as illustrated in Figure 5.3.

SVD

The silicon vertex detector (SVD) is also part of the vertex detection for the two *B* meson decay vertices, but additionally measures vertices of subsequent decays [16]. The SVD consists of four layers of double-sided silicon strip sensors, such to keep the cost and amount of readout channels for such a detector in a reasonable range compared to a pixel detector. Like the PXD, the SVD layers are constructed from several "ladders". Due to the forward boost in the collision, the SVD sensors are

(a) Arrangement of PXD sensor modules [16]

(b) Layout of SVD layers with PXD layers in black [16]
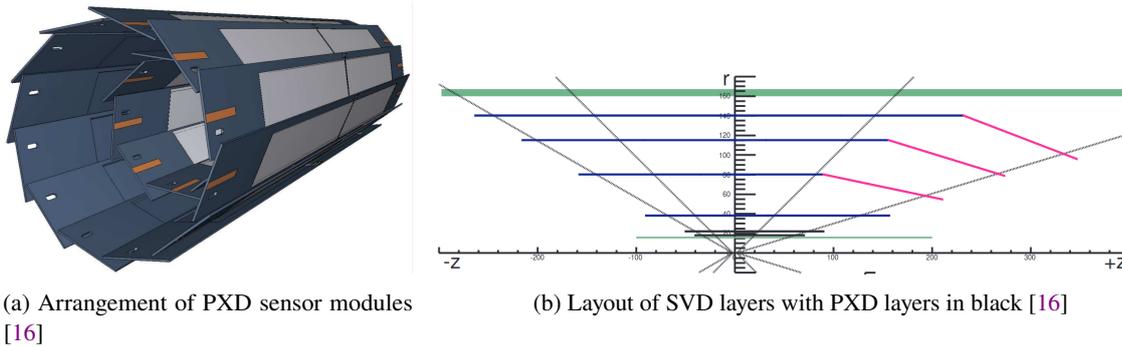
Figure 5.3: Design of the vertex detectors, PXD and SVD

slanted in the forward region in order to minimize the material traversed by the particles in forward region by increasing the incident angle thus reducing material budget. Additionally, this reduces the number of wafers needed. This shape of the SVD is illustrated illustrated in Figure 5.3.

CDC

The central drift chamber (CDC) is the tracking detector for Belle II. It is described in more detail in section 5.3.

TOP

In the barrel region of the detector the time-of-propagation detector (TOP) is used for particle identification (PID) [16]. The TOP uses quartz bars placed around the outer wall of the CDC in which the time of propagation of Cherenkov photons, which are reflected internally inside the quartz, is precisely measured by micro-channel plate photo-multipliers (PMT). The PID is done by measuring differences in arrival times between photons from different particles.

ARICH

In forward region the PID is done by the Aerogel Ring-Imaging Cherenkov detector (ARICH) [16]. The ARICH consists of two aerogel radiator layers of a few cm thickness with different refractive indices in which Cherenkov light is created, followed by the expansion volume of around 20 cm to allow for expansion of the Cherenkov ring for achieving the required resolution for the Cherenkov angle. Afterwards, there are position sensitive photo sensors which can detect single photons with a granularity of a few mm.

ECL

The electromagnetic calorimeter (ECL) needs to measure the energy and angular coordinates of photons with high efficiency since a large fraction of decay products from the B-Meson are π^0s which decay into two photons [16]. Additionally the ECL is used for electron identification and K_L^0 detection alongside the KLM. For the calorimeter CsI(Tl) was chosen a scintillating crystal. They are arranged in a barrel region ($r = 125 - 162$ cm) and annular endcaps at $z = -102$ cm and 196 cm.

KLM

The K_L and muon detector (KLM) is the outermost sub-detector of Belle II [16]. It consists of alternating layers of active detector material and iron plates which serve as passive material for shower creation in the calorimeter and as magnetic flux return for the superconducting solenoid which is located between the KLM and the ECL in the barrel region. The barrel region of the KLM uses resistive plate chambers while in forward and backward endcaps use scintillator strips.

5.3 CDC

5.3.1 Geometry

The CDC is the main tracker for the Belle II detector [16]. It is a wire chamber which consists of 56 layers of wire which are grouped into nine "superlayers". The superlayers differ by having an alternating configuration of axial and stereo wires. This allows for 3-dimensional reconstruction of particles which pass multiple superlayers. This configuration is illustrated in Figure 5.4. In total there are 14 336 gold-plated tungsten sense wires of 30 μm diameter in the He-C_2H_6 filled chamber, which has an inner radius of 160 mm and an outer radius of 1 130 mm. The innermost sense wire, belonging to superlayer 0 (SL0), is located at a radius of 168 mm. Since the innermost layer is expected to have by far the highest occupancy due to beam backgrounds and the wall effect (production of charged particles in wall of the CDC), the sense wires in SL0 have a higher density than in the other superlayers, as illustrated in Figure 5.4. Additionally, SL0 consists of eight layers of sense wires instead of six layers like all other superlayers.
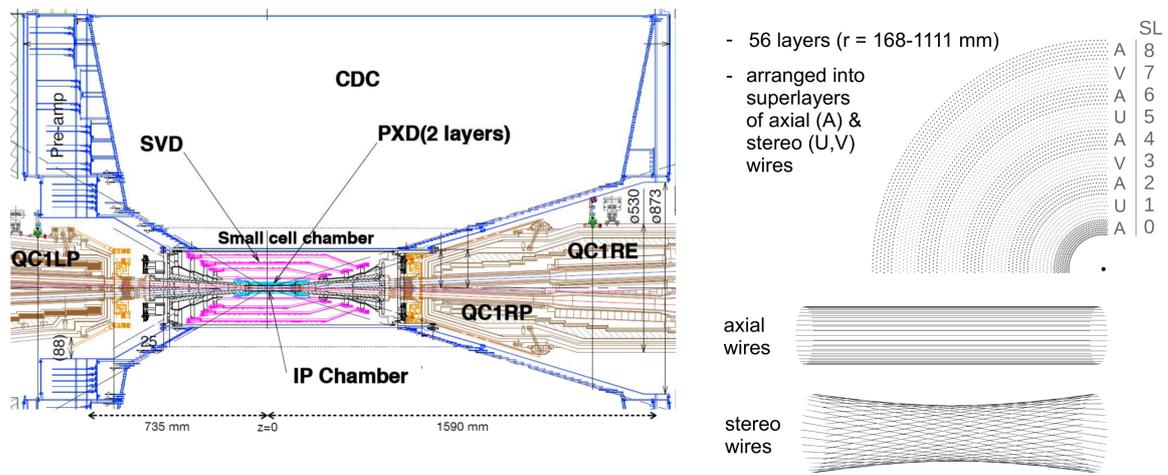
Figure 5.4: Design and wire configuration of the CDC [17]. The skew of the stereo wire configuration is exaggerated.

5.3.2 Tracking with the CDC

Since the CDC is located within the magnetic field of the superconducting solenoid, the charged particle tracks will be curved, due to the Lorentz force acting on the particles. From the curvature

of the track the particle's transverse momentum can be determined, see chapter 4. For this purpose, the track has to reconstructed at least in the $x - y$ coordinates. However, the CDC is capable of reconstructing all three dimensions of a track which is needed for track finding in combination with the other sub-detectors in order to reconstruct the full momentum of the particle.

The $x - y$ information of the track can be determined precisely by the timing information of the electron drift from ionization to the anode wire, where the electron is accelerated due to the $1/r$ electric field of the wire. Thus, the electron is amplified by creating secondary charge until the signal becomes large enough to be read out. The CDC reaches a transverse spatial resolution of $\sigma_{r\phi} = 100\,\mu m$.

If a charged particle traverses multiple superlayers the stereo angle from every other superlayer can be used to reconstruct the z coordinate of the hit. The CDC reaches a resolution of $\sigma_z = 2\,mm$ in z direction.

An important metric for the performance of the CDC is the achieved transverse momentum resolution σ_{p_T}, describing how well the true p_T value is reconstructed.

Apart from the p_T resolution, the track finding efficiency is an important measure for the CDC, since it is the first step in the full track reconstruction [4]. The track finding efficiency is defined as fraction of tracks which were found and correctly matched to the Monte Carlo tracks.

Apart from measuring charged particle tracks, the CDC also serves as a trigger for charged particles since there is little delay between a particle traversing the CDC and the signal, and it provides PID information by measuring the energy loss per track length dE/dx [16].

5.3.3 Limits of the CDC

The beam background (described in more detail in section 10.6) at the SuperKEKB accelerator is much higher than anticipated originally in the design phase of the CDC [18].

Studies regarding the limits of the CDC once SuperKEKB reaches design luminosity are still ongoing. Some concerns include:

- aging of the wires in the He-C_2H_6 gas mixture

- gain degradation due to aging and space charge effect, leading to worse resolution

- occupancy in inner layers

- cross talk

- radiation hardness of front-end electronics

The last two items are already being addressed and worked on by the Belle II CDC group by proposing new radiation-hard readout electronics.

However, the occupancy especially will be a challenging factor. With a high amount of beam background the wires in the inner region will have a large hit rate. This will lead to a combinatoric increase in the number of possible tracks where it becomes less likely to reconstruct the correct track.

Figure 5.5 shows the sum of all scaled background components at the original design luminosity of $\mathscr{L} = 8 \times 10^{35}\,cm^{-2}\,s^{-1}$ [16]. The y-axis shows the hit rate per wire plotted against the layers, where the vertical dotted lines denote the start of a new superlayer. The horizontal line roughly depicts the limit of $200\,kHz$ per wire up to which it is believed that tracking is still possible [18, 19]. This limit comes from the space charge of He/C_2H_6 ions which have a drift time of roughly $0.5\,ns$ in the standard

drift cell of SL1–8. Therefore, the wire hit rate needs to be kept below 200 kHz in order to keep the electrons from experiencing the field distortion due to the ions.
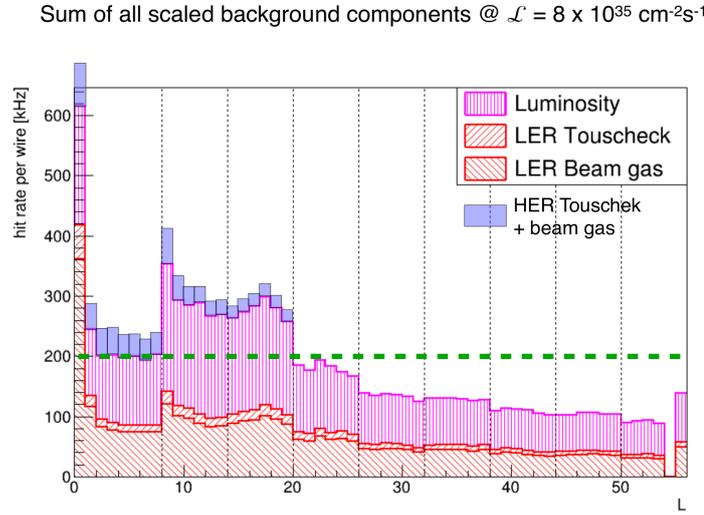
Figure 5.5: Background hit rate per wire for the CDC at design luminosity, showing that the hit rate in the first three superlayers exceeds the limit up to which it is believed that tracking is still reliably possible [19]

The aging due to polymers attaching themselves to the wires and the effect of ions on the charge transport lead to a decrease in gain [3]. The gain degradation is seen in the dE/dx calibration, leading to a deterioration in PID resolution. The hit efficiency, which is the fraction of registered electrons from the total amount of created electrons, might also decrease, worsening the tracking performance. [20]

Since it is expected that the CDC might not be able to maintain the required performance in tracking, PID and triggering at full design luminosity, this study deals with conceptual design for a time projection chamber as a contingency for a replacement of the CDC for the Belle II experiment. The working principle of such a detector is described in section 6. This project started from an idea shared by Carlos Marinas to Peter Lewis [21]. Some of the reasons for replacing the CDC with a time projection chamber are outlined in section 7.1.

Time Projection Chamber

6.1 Working Principle

A time projection chamber (TPC) is a tracking detector in which a volume, typically a cylindrical volume for high energy particle colliders, is filled with a gas which is ionized by high energetic, electrically charged particles due to Bethe-Bloch ionization [3]. The created space charge is separated via an electric field such that the electrons and ions drift towards the anode and cathode, respectively. For a cylindrical TPC the anode is placed at one of the endcaps, the cathode can either be placed at the endcap opposing the anode, or it can be located within the TPC, thus creating two separate drift volumes for the space charges where the other endcap acts as second anode. In most cases, the electrons are read out, when they reach the amplification zone at the anode, since the electrons will reach their electrode much faster than the ions due to higher mobility in the gas. Figure 6.1 shows an illustration of the working principle of a TPC.
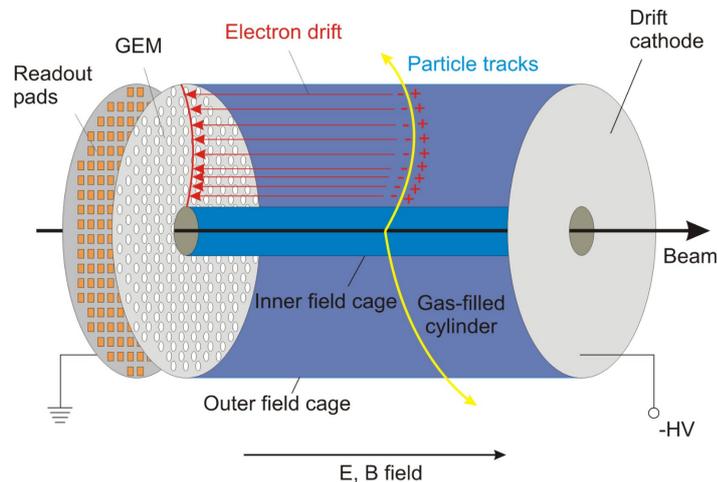
Figure 6.1: Working principle of a TPC with electrons from ionization due to the charged particle drifting towards the readout region [22]

The projection on the readout plane yields the $x - y$ information of the track. By measuring the electron drift time using a either a trigger signal or accelerator information as start signal, it is possible

to gain information on the z coordinate of the electrons creation point [3] . Thus, the track position can be reconstructed in three dimensions. This requires precise knowledge of the drift velocity. Therefore, it is desirable to have a very homogeneous electric field which can be achieved by operating a field cage in the TPC.

In the presence of a magnetic field parallel to the electric field, the transverse momentum can be determined from the curvature of the track. Additionally, the magnetic field reduces transverse diffusion of the electrons during drift, thus improving spatial resolution of the detector in the $x - y$ projection (see chapter 4).

A TPC can also be used for PID using the $\mathrm{d}E/\mathrm{d}x$ distribution, which is the energy loss per track length, since a TPC can measure the energy loss precisely by counting the number of created space charges.

6.2 Amplification Region

The amplification region of a TPC can take multiple forms. Figure 6.2 shows a fairly traditional example for the amplification using multiple stages of wires. Due to the electric field going with $1/r$ the electrons are accelerated enough between two scatters to ionize the scattering atom, thus creating an avalanche of electrons which creates a signal strong enough to be read out. The ions created in the amplification of electrons drift back towards the drift volume due to their charge. Since they have a low mobility, these ions would stay in the drift volume for a long time. If a large number of ions accumulates in the drift volume they can disturb the electric field, thus impeding on the space-drift velocity relation. In order to avoid this, a gating layer can be incorporated which in open mode will let the electrons from the drift volume and the ions from the amplification pass, while in closed gate mode the back-flowing ions are mostly absorbed. This is shown in lower and upper part of Figure 6.2, respectively.

6.2.1 GEMs

A modern alternative to wires for the amplification are gas-electron-multipliers (GEMs) [3]. GEMs are thin Kapton foils with a layer of copper on both sides and perforated with holes. Figure 6.3(a) shows an example for a GEM foil of 50 μm thickness with 5 μm copper layers. By applying a voltage across the copper electrodes a strong electrical field is created within the holes of the GEM in which the electrons are accelerated, thus creating secondary electrons by ionization. This process is illustrated in Figure 6.3(b).

One advantage of GEMs is that they have an intrinsic suppression of ion back-flow since some of the ions are neutralized at the surface of the GEM, as illustrated in Figure 6.3(b). Using this, it is possible to operate the TPC without a gate when using multiple GEMs in a stack with a specific hole configuration, as is the case for the ALICE TPC upgrade [25].

6.2.2 Micromegas

Micromesh gaseous structures (Micromegas) are a gaseous parallel plate detector with a narrow amplification stage, which also uses a thin micromesh foil for the amplification of electrons [26]. The micromesh, acting as cathode, is typically placed 50–100 μm above the anode.
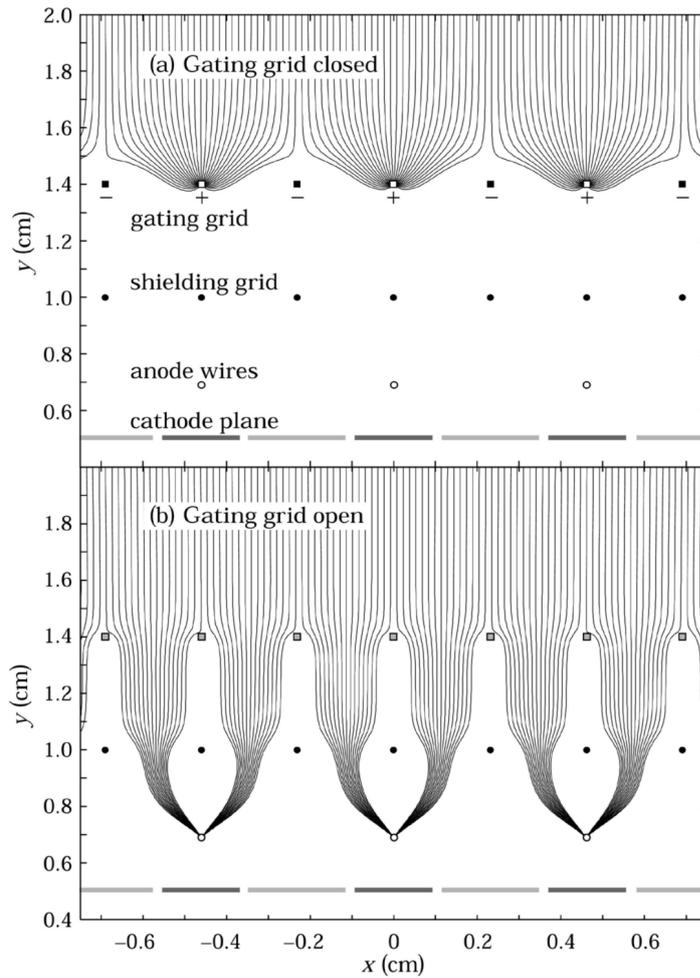
Figure 6.2: Electric field lines for closed and open wire gate [23]

Figure 6.4 shows the electrical field lines for this setup and and an image of the micromesh from a scanning tunneling microscope. This particular image is from the GridPix detector which is a special type of Micromegas where the mesh is aligned with the pixel of the underlying chip, which in this case is the Timepix3 chip [27]. Since the distance between the mesh and the pixels is only 50 µm the charge from the amplification will not spread to neighboring pixels through diffusion as long as the amplification is not too large. In the case that only one primary electron enters the hole it is possible to detect single primary electrons with high efficiency, leading to a high energy resolution. Combined with the excellent spatial resolution of the Timepix3 chip due to the pixel size of 55 µm it is possible to measure the energy loss per track length (dE/dx) directly.
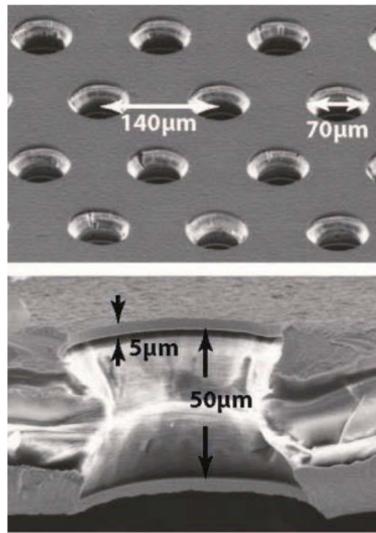
(a) Image of a GEM from a scanning tunneling microscope (above), enhanced cross section of a hole (below) [3]
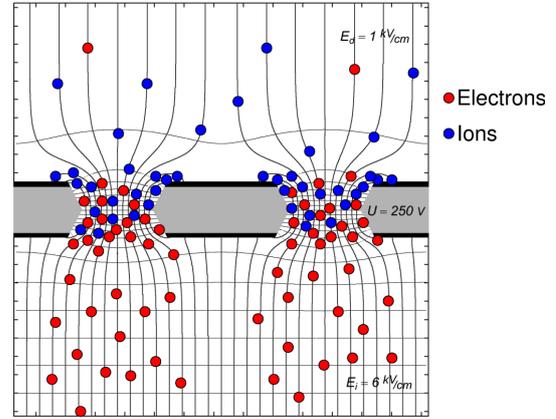
(b) Schematic illustration of gas amplification in a GEM [24]. The electrons create an avalanche after being accelerated by the field in the GEM hole. The ions either drift back into the drift volume or are absorbed by the GEM.

Figure 6.3: Working principle of a GEM
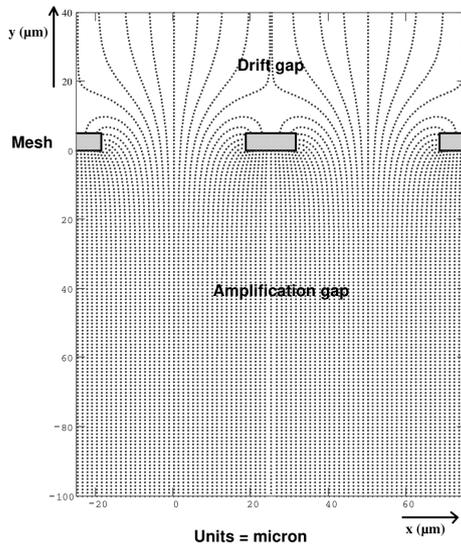
(a) Electrical field lines in a Micromegas [26]
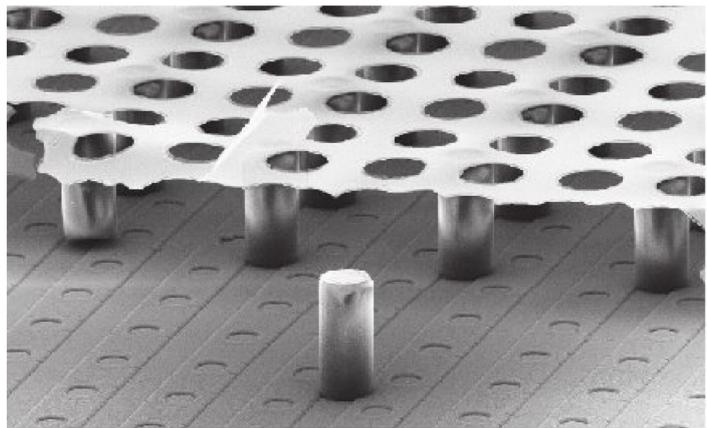
(b) Image of the InGrid setup where mesh and pixels are aligned [27]

Figure 6.4: Working principle of a Micromegas

Upgrade Proposal

This chapter introduces the argument for replacing the CDC with a TPC and discusses potential advantages and disadvantages.

7.1 TPC as replacement for the CDC

Replacing the CDC requires another type of full 3D tracker, which the TPC is. The TPC provides a large number of sampling points leading to excellent momentum resolution and dE/dx measurements for each track [3]. Since it mainly consists of a gas-filled volume it has low material budget while still covering a large fraction of the solid angle.

Since the occupancy of a TPC depends on the number of voxels (volumetric pixels) it can be a lot more tolerant for background than the CDC. Replacing the CDC with a full silicon tracker would not be realistic given the cost of such a detector. Additionally, there has already been a lot of research conducted for tracking TPCs with fairly similar tracking conditions, this research can be used as a starting point for the development of a Belle II TPC.

There are certain downsides to replacing the CDC with a TPC, which are discussed briefly here.

One of the main concerns is that a TPC cannot provide a trigger for the experiment. The CDC is a crucial part of the level 1 trigger (L1) for Belle II requiring a maximum trigger rate of 30 kHz, a fixed trigger latency of 5 μs and a timing precision below 10 ns [28]. The CDC trigger searches two- or three-dimensional track segments which can happen very fast since the hits arrive with almost no delay at the wires. In the case of the TPC the hits need to travel for several micro-seconds before being registered at the readout plane. Therefore, a candidate for a new component to the L1 trigger needs to be investigated in order for the TPC to be realistic replacement of the CDC. This study only deals with the simulation of the TPC, however, Appendix A briefly introduces a proposal for a time-of-flight extension for the TOP which could potentially serve as source of trigger.

Due to the large drift times in the TPC and the high luminosity of the SuperKEKB accelerator a large amount of overlap between events is to be expected. It is therefore necessary to investigate the amount of event overlap in the TPC and estimate whether correct hit-event assignment will still be possible. This study is described in more detail in chapter 10. An idea for assigning tracks to their respective events is outlined in section 10.4.

Another consequence of the high event rate is that gating might not be possible for the TPC in order to reduce the ion back-flow In this case the readout of the TPC would have to continuous, similar

(a) CDC geometry in the current setup [14]

(b) Layout of the proposed upgrade by expanding silicon and replacing the outer part with a TPC
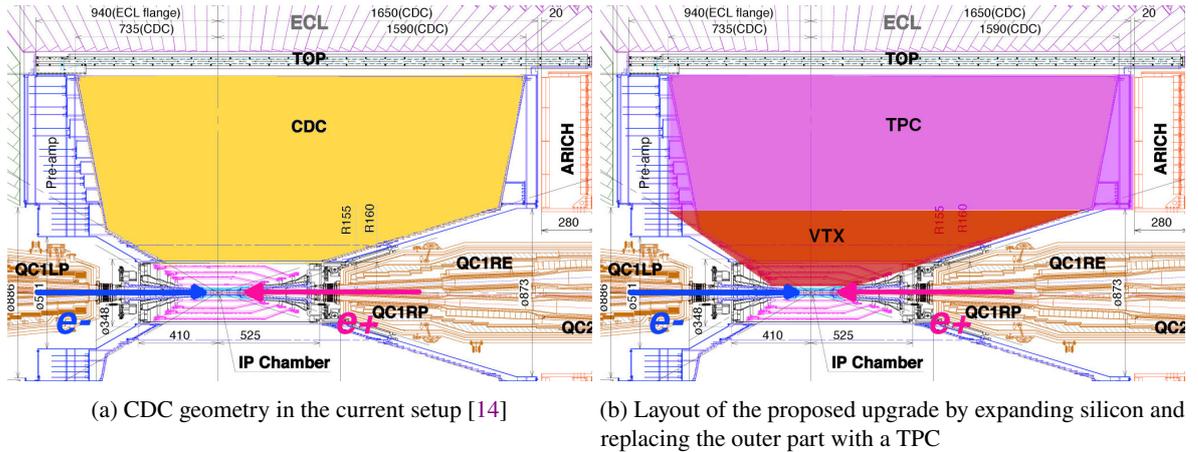
Figure 7.1: Geometry comparison for the upgrade proposal with the current setup

to the proposed ALICE TPC upgrade [25]. Whether this is possible depends on the ion back-flow characteristics and limits on field distortion due to ions which are studied in section 10.6.1.

This thesis is supposed to be a proof-of-concept for a TPC as replacement for the CDC. The entire study is based on the simulation of the TPC in the Belle II framework. Since this will only be a first-order approach some simplification will be made along the way. Additionally, optimization of most parameters is secondary to this study.

The timescale for this project is currently still open-ended. It is therefore not clear, if this upgrade scenario could happen during the duration of the Belle II experiment or if is more suitable for a possible Belle III scenario. In the former case, the replacement would need to occur during one if the upcoming Belle II shutdowns. In the year 2026 there will be a shutdown of SuperKEKB for an upgrade of the focusing quadrupoles in the interaction region for increasing the luminosity [29]. It does not seem realistic to have a fully developed TPC by then. Afterwards, there are plans to further increase the luminosity for 2030 and beyond [29]. These are more achievable dates and a TPC upgrade should be targeted for this period.

7.2 Geometry

The TPC is designed to replace all but the first three superlayers of the CDC. Due to the presence of the focusing quadrupoles around the CDC at the inner superlayers, this region is not suited to be replaced by a TPC, since it does no allow for a straight endcap [16]. Instead, this region could be covered by an upgrade of the silicon detectors. A project dealing with such an upgrade is the VTX upgrade, a project which is already underway. It is described in more detail in section 7.3. The upgrade scenario including TPC and VTX is illustrated in Figure 7.1.

The tight geometrical constraints from the Belle II detector lead to relatively fixed dimensions for the TPC, which are listed in Table 7.1. The total θ acceptance, measured at the inner radius of the TPC, is not a good measure for the true acceptance of the TPC, since tracks which only pass the inner corner cannot be properly be reconstructed. Therefore, the acceptance based on the outer edge is also given. The true acceptance will depend on the track finding ability of the pattern recognition algorithm for the TPC and will probably lie in between these acceptances.

TPC Geometry	Coordinates in Belle II detector
Inner Radius	44.65 cm
Outer Radius	109.6 cm
Forward Endplate	159.07 cm
Backward Endplate	−83.62 cm
Total θ acceptance	$15° < \theta < 152°$
Outer edge θ acceptance	$34° < \theta < 128°$

Table 7.1: Dimensions of the TPC due to geometrical constraints

Since the ARICH PID system is situated in the forward region (see Figure 7.1), it is important to keep material in front of the ARICH to a minimum [16]. The readout of the TPC therefore has to be placed in the backward region where there is no PID system [16]. This does not allow for a TPC with a central high voltage electrode but instead it needs to be a single drift volume, leading to large drift times.

7.3 VTX

The current vertex detector (VXD) consists of the PXD and the SVD described in section 5.2. Current extrapolations for the VXD occupancy at nominal peak luminosity show that the VXD will operate within the required limits but without much margin [29]. Therefore, studies for a short-term VXD upgrade for the 2026 shutdown have already started. The vertex detector (VTX) is a newly proposed sub-detector designed to completely replace the current VXD. It takes the form of 5 or 7 fully pixelated silicon layers in the barrel region and optionally two forward disks. Its layout is shown in Figure 7.2. Compared to the current system the VTX will have to achieve at least the same tracking performance with even lower material budget and achieve a higher radiation hardness. [29]
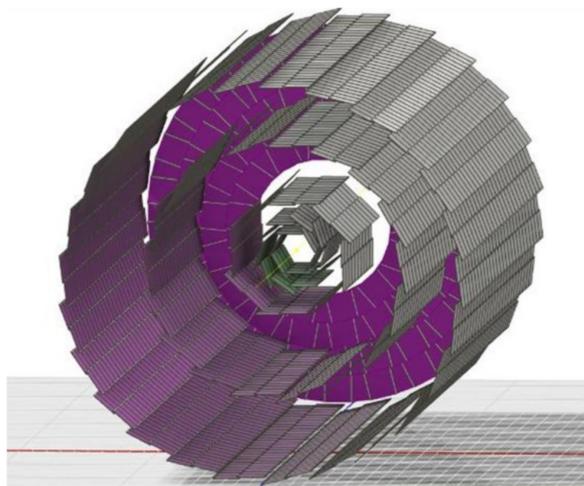
Figure 7.2: 5 layer configuration of the VTX upgrade [29]

For this purpose several sensors are being investigated. In Bonn there are investigations going on using a depleted monolithic active CMOS sensor, the TJ-Monopix 2, as small and low power-consuming pixel sensor for all layers [29]. Those pixels would have a size of $30 \times 30\,\mu\text{m}^2$ with an integration time of 25 ns. The prototype for a Belle II specific chip, called OBELIX, is expected for 2022.

Further information for the VTX can be found in Ref. [29], [30] and [31].

Simulation of the TPC

For this study, the TPC is simulated within the Belle II Analysis Software Framework `basf2` containing the code specifically created for Belle II such as the basic software framework, detector simulation split into each sub-detector and some analysis tools.

Each Belle II sub-detector code comes in its own package [32]. It contains several pre-defined sub-directories which are needed for the simulation. The `data` directory contains the description of detectors geometry. The `dataobjects` are the classes which can be stored in the output files. `Modules` are tools which help in processing the data from an event (simulation). The modules can be independently loaded on-demand and their order is defined by the user in the Python steering file, as illustrated in Figure 8.1. Examples for such modules include first steps for finding clusters or tracks, but also the Digitizer which will be expanded upon in section 8.2.1.
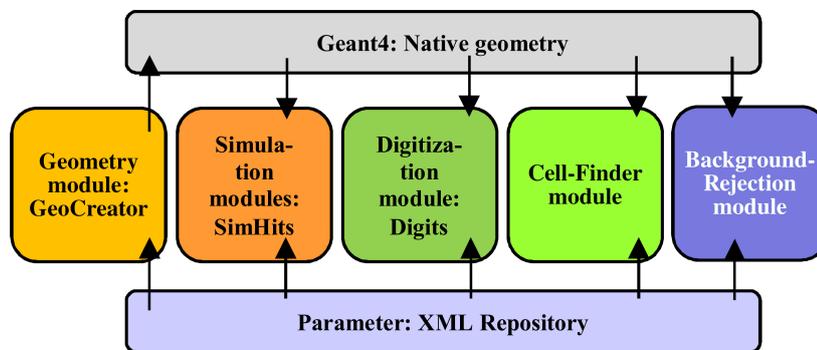
Figure 8.1: Chain of a `basf2` job with time going from left to right. Geometry parameters are taken from a `xml` repository and used for the simulation. [33]

The detector geometry is described in section 7.2. For the first part of the simulation additional operational parameters need to be specified.

8.1 Operational Parameters

For the choice of operational parameters like the gas mixture and drift field the TPC prototype by the LCTPC collaboration for the ILC can be used as a starting point since the tracking requirements are

comparable [34]. Therefore, the T2K gas mixture (Ar:CF_4:iC_4H_{10} (95:3:2)) at atmospheric pressure, which the LCTPC collaboration proposes for their TPC, is used for this simulation [35]. This particular gas mixture allows for fast drift velocities, while keeping diffusion in the drift volume relatively modest [36].

The drift field is chosen such to maximize the drift velocity in order to reduce event overlap in the TPC. For this purpose, a MAGBOLTZ simulation was conducted by Jochen Kaminski of the LCTPC collaboration. The results of his simulation can be seen in Figure 8.2. The value for the optimal drift field E_D is listed in Table 8.1 alongside the resulting values for the drift velocity v_D and the longitudinal and transverse diffusion coefficients σ_{long} and σ_{trans} respectively.

Operational Parameter	Optimal Value
E_D	289 V/cm
v_D	7.89 cm/μs
σ_{long}	200 μm/cm$^{0.5}$
σ_{trans}	84 μm/cm$^{0.5}$

Table 8.1: Results from the MAGBOLTZ simulation for the optimal operational parameters

With a drift velocity of $7.89\,\mathrm{cm}\,\mu\mathrm{s}^{-1}$ and a maximal drift length of 242.69 cm one TPC length is worth 30.75 μs of drift.

8.2 Simulation

8.2.1 Simulation Chain

The detector simulation for Belle II is done within the basf2 framework utilizing GEANT4 for the simulation of particles interacting with the detector. Each sub-detector has its geometry details stored in an xml file. In the case of the TPC detector this file contains the size of the TPC as well as the contents of the gas mixture. Additionally, other relevant details can be stored in corresponding xml files, like readout characteristics or additional parameters for the gas mixture.

This data is read and stored by a corresponding geometry class, TPCGeometry in the case for the TPC, which passes the information to the GeoCreator class. In this class the sub-detector is build using GEANT4 and its corresponding syntax. Within GEANT4 the SensitiveRegion is defined for the sub-detector in which hits through particle interactions are generated. In the case of the TPC the SensitiveRegion takes the form of the gas mixture which in a real detector is ionized by traversing particles. The hits which are created in the SensitiveRegion along a GEANT4-step are stored in the framework as SimHits which contain Monte Carlo information relevant to the hit. This includes the coordinates and creation time of the hit in the global detector coordinate system, as well as the PDG code of the particle creating the hit and anything else of use which is added to the SimHit class.

The SimHits are then passed to modules created for each sub-detector for further processing. The most important module is the DigitizerModule which turns the SimHits with truth level information into Digits which contain detector level information, meaning that they represent the detector output[1]. For the TPC the Digits include effects like drift and diffusion as well as the granularity

---

[1] Other examples for modules for the TPC include the background rejection and 3D cell creator
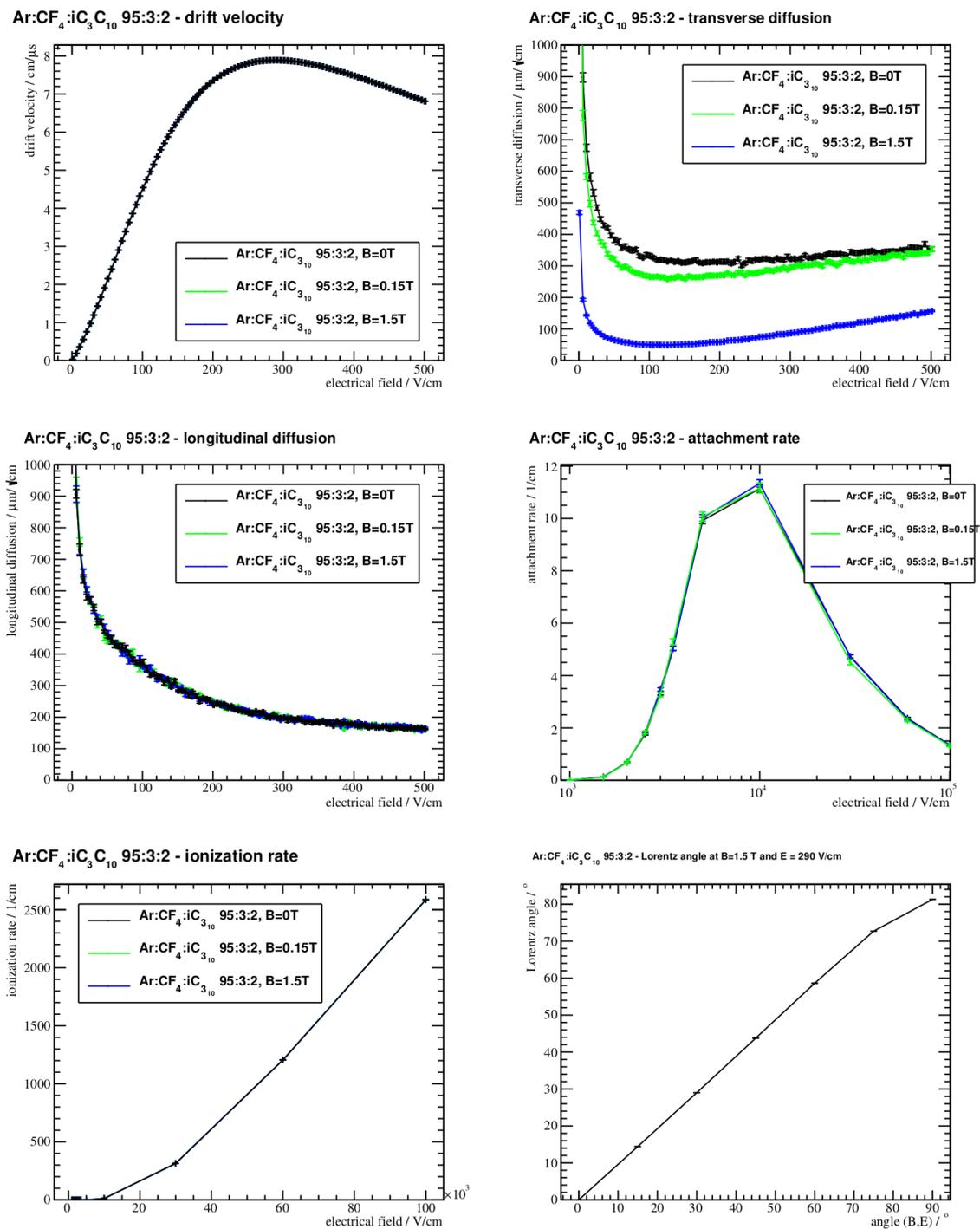
Figure 8.2: MAGBOLTZ simulation for optimal working point of electrical field for various parameters [37]. Maximal drift velocity achieved at $E_D = 289\,\mathrm{V\,cm^{-1}}$

of the readout plane. Gas mixture parameters like diffusion coefficient and drift velocity but also geometry parameters like the position of the readout plane for conversion of the z-coordinate to drift length l_{drift} need to be passed to the `DigitizerModule`. This is done by the `GeometryPar` which reads operational parameters like temperature, pressure, drift velocity, and diffusion coefficients, both longitudinal and transverse (σ_{long} and σ_{trans} respectively) from the `xml` files.

A simplified flowchart for the simulation chain for the `basf2` simulation is presented in Figure 8.1.

8.2.2 Diffusion

Since the charge transport is not simulated in `basf2`, there is no direct way of implementing diffusion of the charge while drifting towards the endplate of the TPC. However, since the drift properties of the gas are well known due to the simulation results from Figure 8.2, the diffusion can easily be modeled. So instead of simulating the drift, this process is modeled by applying Gaussian smearing to the coordinates of ionization in the `TPCDigitizerModule`. The coordinates after smearing the represent the reconstructed hits.

The effect of this smearing can be seen in Figure 8.3. The first images show the projection of Hits (which are the `SimHit` representing truth level information) and Digits (Hits after the `DigitizerModule` representing detector level information) on the readout plane in $x - y$ direction for 10 example muon tracks in the momentum range of $1 - 4\,\text{GeV}$.

The diffusion is simulated using a simple approach: the x, y and z coordinates are randomized by drawing a random number from a Gaussian distribution which has the coordinates as mean value and $\sigma_{\text{diff}} \cdot \sqrt{l_{\text{drift}}}$ as width, where $\sqrt{l_{\text{drift}}}$ is the drift length and σ_{diff} is the corresponding diffusion coefficient, σ_{long} for diffusion in z direction and $\sigma_{\text{trans}}/\sqrt{2}$ for diffusion in the transverse $x - y$ plane. The factor of $1/\sqrt{2}$ compensates for the fact that diffusion in x and y is treated independently.

Using the Gaussian approach for the diffusion it is possible for Hits close to the cage for the TPC to diffuse "outside of the TPC volume". Hits which show such behavior are considered lost and are not stored as Digit. Thus, there is no one-to-one relation between Hits and Digits. The fraction of Hits lost this way is roughly 0.08 %. The hit efficiency is one important parameter for the $\text{d}E/\text{d}x$ resolution of the TPC which is studied in section 9.1.

8.2.3 Readout Parameters

The efficiency with which single electrons are detected also depends on the choice of readout. For the readout there is a choice between using readout pads, strips, or pixels, while for the amplification wires, GEMs, or Micromegas are possible.

The highest performance in spatial resolution can be achieved with pixel chips with an integrated grid for amplification, as is the case for the GridPix detector, described in section 6.2.2, which is one proposed readout strategy for the LCTPC [27]. Since there is no charge sharing between the pixels, one can assume binary readout, meaning that it is only of interest whether a pixel was hit or not. So instead of measuring the charge by counting the clock cycles above a threshold, only the threshold passing time is used. This allows for a lower data throughput of the detector. Assuming a clock frequency of 40 MHz a threshold passing time resolution of 25 ns can be achieved. With the operational parameters from section 8.1 this results in a spatial resolution of $\sigma_z = 2\,\text{mm}$ in z direction.

(a) Hits of 10 muon tracks

(b) Digits of 10 muon tracks

(c) Close-up comparison between Hits and Digits
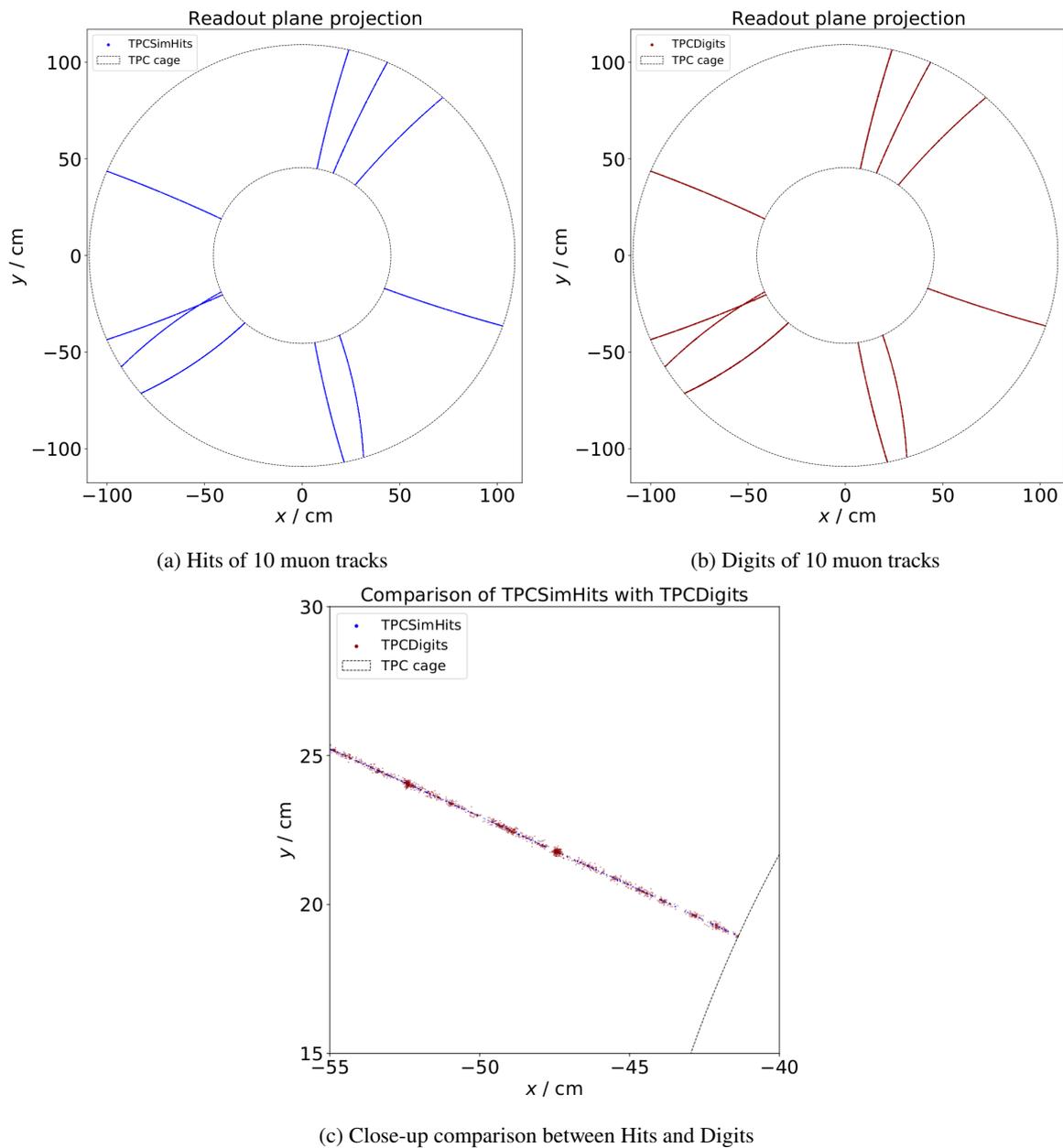
Figure 8.3: Direct comparison between Hits and Digits for 10 muon with momenta in the range of 1-4 GeV.

Since the GridPix detector has a pixel pitch of 55 μm the same can be assumed for the Belle II TPC. With this readout electron efficiencies of around 90 % were achieved [27]. For the Belle II TPC a value of 95 % is assumed.

Track Investigation

With the simulation of the TPC set up, first studies regarding tracking and particle identification can be conducted, in order to investigate if the TPC can match or perform better than the CDC in those categories. This chapter shows some of the results and findings of those studies.

9.1 dE/dx

It is useful to compare the performance of the TPC to the CDC that the TPC is designed to replace. The dE/dx resolution is of special interest, since the TPC has a larger inner radius than the CDC and therefore particles need a larger transverse momentum p_T in order to reach the TPC from the interaction point. For particles with transverse momenta sufficient to reach the CDC but not the TPC this dE/dx information is lost.

This study of dE/dx is done by simulating 5 000 of each muons, pions, kaons, protons, and electrons with momenta varying from 100 MeV (just about reaching the TPC) up to 3 GeV (commonly largest momenta for particles from B meson decay [4]). For each track dE/dx is calculated by dividing the total energy loss in the track by the track length. dE/dx is therefore averaged over the entire track and plotted in Figure 9.1 as a scatter plot vs. the Monte Carlo (MC) particle momentum, which is truth level information from GEANT4. It is compared directly to a dE/dx simulation for the CDC to which the TPC plot has been adapted.

While the separation looks clearer in the TPC plot one has to keep in mind that the statistic is higher for the CDC, and crucially, the simulation of the TPC is simplified. Most importantly, the hit efficiency in this study is still considered to be close to 100 %, meaning that practically all electrons from the ionization are read out. A loss in electrons would act as a scale factor of the measured energy loss compared to the true energy loss, and such would decrease the achievable energy resolution. Additional effects like field distortions which are not yet simulated also play in role in degrading the dE/dx resolution. However, as first study this shows promising results.

From the dE/dx information one can further calculate the number of created hits using the work function for the T2K gas mixture. For track finding purposes the number of hits per cm, i.e. dN/dx, is of interest. This can be seen as a histogram in Figure 9.2 for the same particles as in Figure 9.1. For the MIP region there seem to be between 50 and 100 hits per cm.
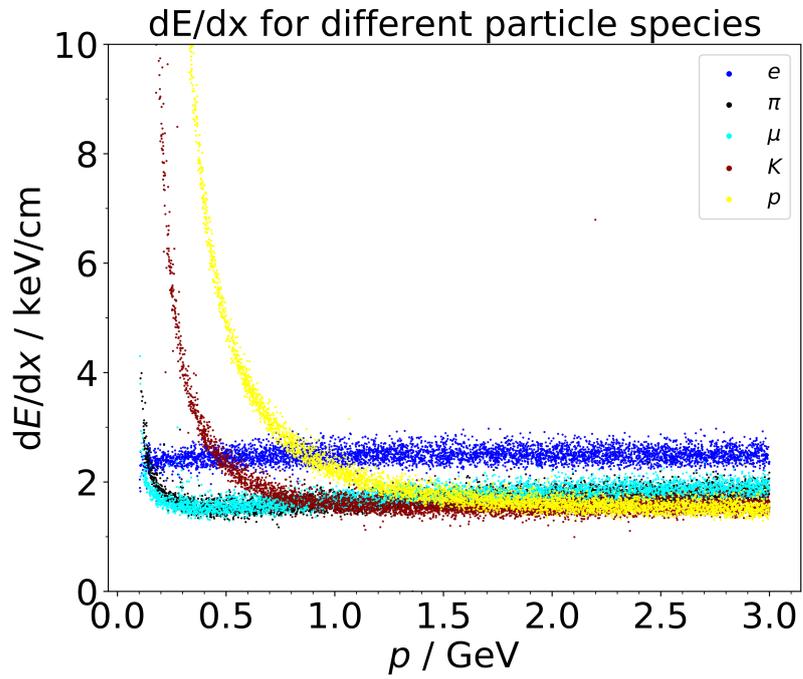
(a) dE/dx simulation for the TPC
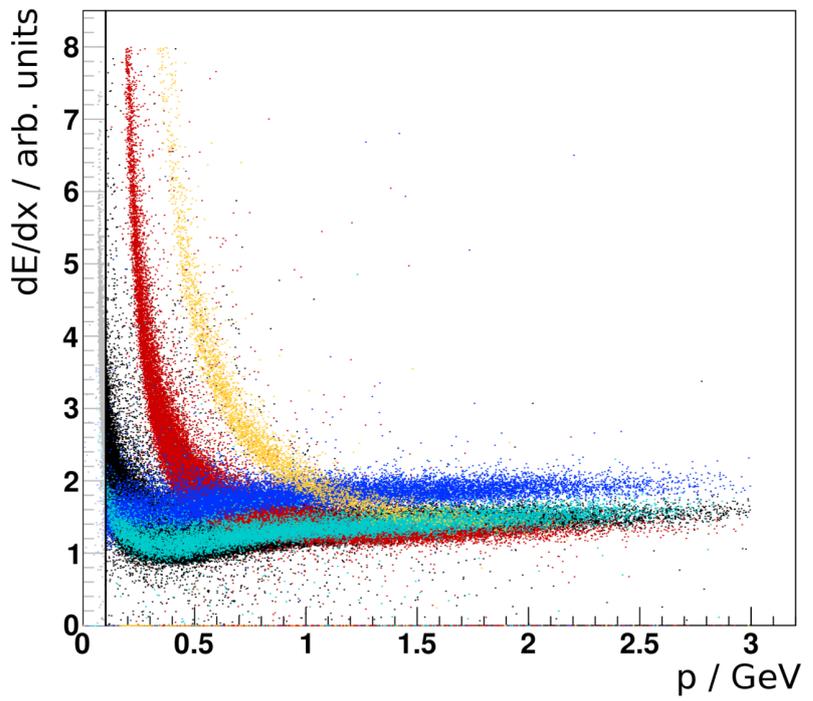
(b) dE/dx simulation for the CDC [38]

Figure 9.1: dE/dx from simulation for the TPC and CDC. Low p_T part which does not reach the TPC is low-lighted in the CDC plot.
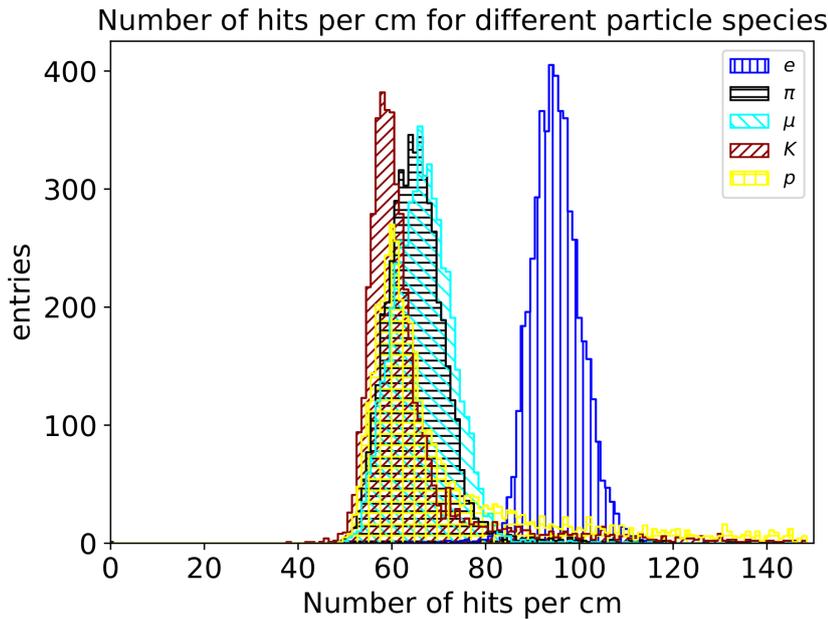
Figure 9.2: Distribution for the number of hits per cm

9.2 Micro-Curlers

The general behavior of the TPC can be further investigated by generating 100 pions tracks with momenta in the range of 0.2 to 10 GeV which can be seen in Figure 9.3. In this plot, one can notice spots of large energy deposition, which upon closer inspection are revealed to be created by secondary electrons. One of theses spots is show close up in Figure 9.4(a) while the side view for the TPC volume is shown in Figure 9.4(b). In this side view the coordinates are given in the global Belle II coordinate system, where the interaction point is located at $(0, 0, 0)$. For this TPC, with single side readout, the z coordinate is equivalent to a time coordinate since hits close to the backward endplate will reach the readout first. This is an important concept which will be used in the display of event overlap in chapter 10.

The electrons in Figure 9.4 are trapped inside the magnetic field such that they keep their $x - y$ position while they travel large distances in z-direction through the TPC volume. They can either be produced as δ-electrons, where the micro-curler is attached to a track, or as Compton-electrons, where the micro-curler stems from the trajectory of a photon which is not visible in the TPC [39].

These large amount of energy deposits create a huge number of background hits, increasing the amount of data produced by the TPC. These tracks are not interesting for reconstruction, since they offer no useful information, but instead would increase the computing time [39]. Therefore, these hits need to be filtered consistently.

A first approach to this problem is to segment the TPC readout plane into $2 \times 2\,\text{cm}^2$ cells, inspired by the size of the Timepix3 chips, and discard the hits if their number exceeds a certain threshold [27]. This method would allow for hits to be rejected at the hardware level, such that they would not be read out to begin with, thus greatly reducing the data throughput of the TPC.

This approach was used for a $\Upsilon(4S)$ event which can be seen (unfiltered) in Figure 9.5. The side view for this event reveals that there are four micro-curlers present in this event.
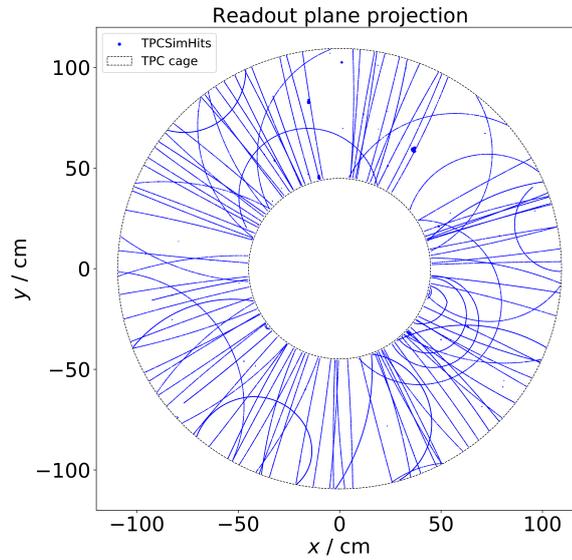
Figure 9.3: 100 pion track projected onto the readout plane
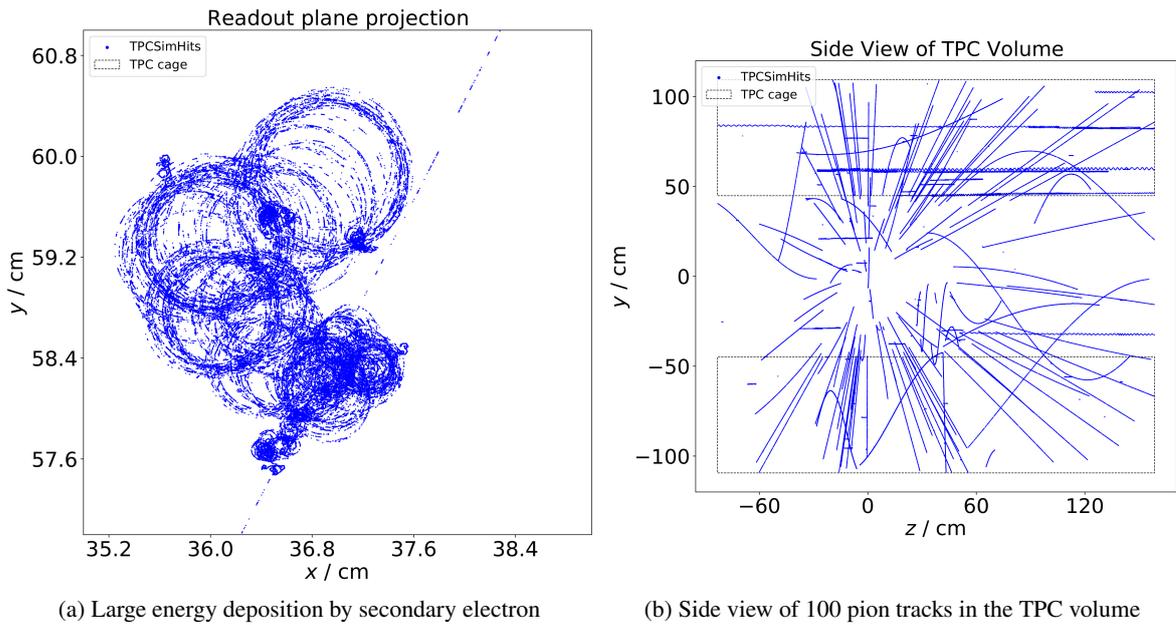
(a) Large energy deposition by secondary electron

(b) Side view of 100 pion tracks in the TPC volume

Figure 9.4: Investigating the large energy deposits by micro-curlers

For the first approach the cell grid was applied to the readout plane without regarding geometrical limits the readout chips will experience in a real TPC, since this is meant as a proof-of-principle. The rejection with a threshold of 1 000 hits in this case can be seen in Figure 9.6. These plots show that indeed most micro-curlers are correctly identified with the exception of the shortest one which probably is not long enough to generate enough hits to pass the threshold. However, it is not very

(a) Readout plane projection for an Υ(4S) event   (b) Side view for the same Υ(4S) event
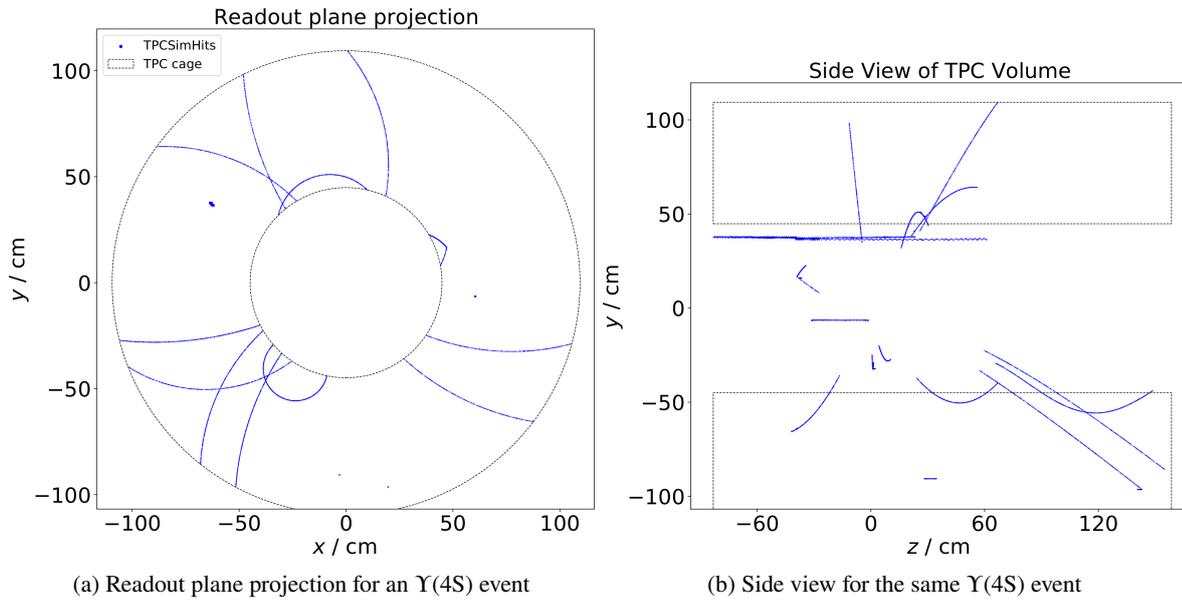
Figure 9.5: Υ(4S) event on which mirco-curler rejection is tested on

efficient to cut the cell over the entire length of the TPC volume. Therefore, for track finding the next step would be to segment the TPC volume into 3-dimensional cells of size $2 \times 2 \times 2\,\text{cm}^3$ and find connected cells in the z direction. An improved version of the micro-curler rejection was implemented by Christian Wessel as part of his PhD thesis based on the aforementioned concepts like the number of hits in the cell or the amount of adjacent cells in z-direction [31]. First results for this method of rejecting micro-curlers are showcased in section 10.7.

9.3 Summary

The dE/dx resolution of the TPC shows promising results, however this study will have to be repeated once the field distortions from space charge are fully simulated.

Identifying and rejecting micro-curlers seems to be a common problem for TPCs [39]. A first geometrical approach seems like a good solution to this problem. A more complete rejection algorithm is presented in section 10.7. The effect of micro-curlers on the tracking conditions of the TPC will be investigated in chapter 10.

(a) Readout plane projection with applied cell rejection

(b) Side view with applied cell rejection

(c) Close-up for a rejected cell
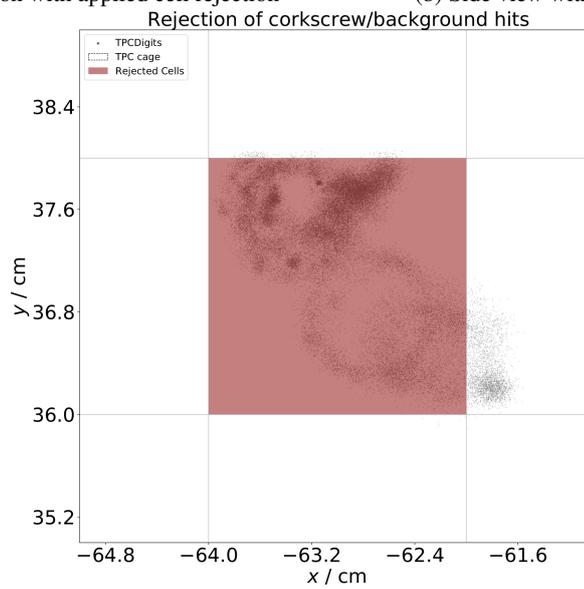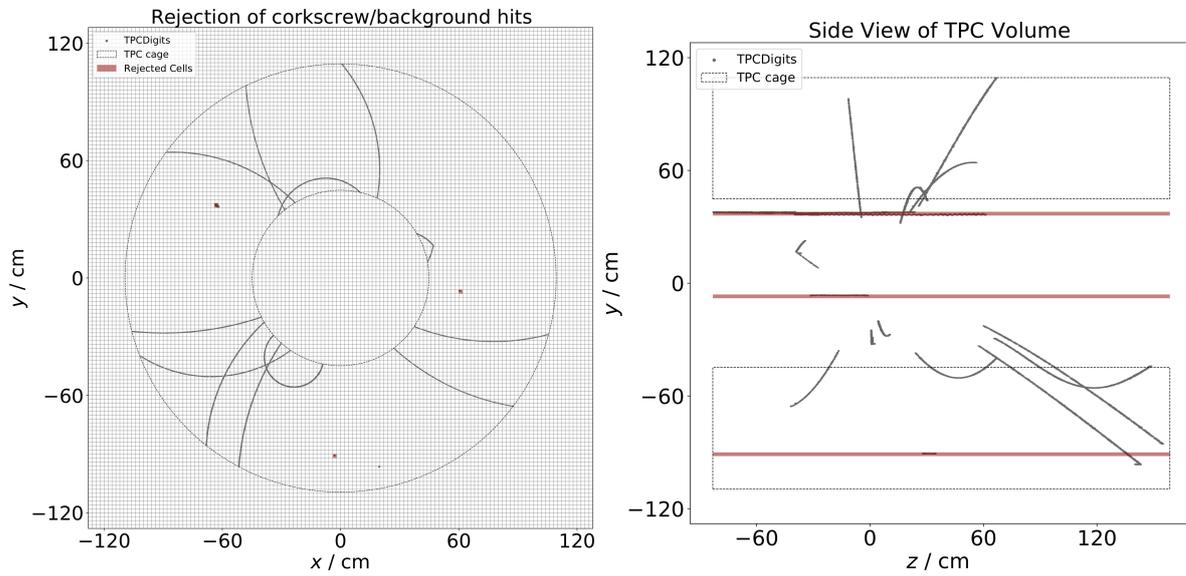
Figure 9.6: Rejection of cells based on hit counts

Event Overlay

Since the maximal possible drift of electrons in the TPC lasts about 30 µs and at Belle II design luminosity bunch crossings happen roughly every 4 ns, there is a large overlap of events in the TPC volume to be expected [10]. It is therefore necessary to investigate the amount of overlap of tracks between events. Since the `basf2` framework is event based, it is not suited well for creating overlapping events in a TPC-like volume. Therefore, the decision was made to move the event overlay procedure to standalone code. This procedure would include generating separated physics events, calculating the event rates for these processes such that they could be placed in time relative to a triggered $\Upsilon(4S)$ event, applying correct diffusion relative to each hits drift length, and creating an event overlay display.

Using this display important studies for the development of the TPC can be conducted. It can be used to study the event pileup and the resulting requirements for a track finding algorithm and hit-event association. Additionally, it might shine some light on the to-be-expected ion back-flow, leading to a more specific design choice for gating in the TPC.

10.1 Physics Event Rates

In order to place the correct amount of events for one physics process into the TPC volume, the event rates have to be calculated based on their cross section and the Belle II luminosity. Table 10.1 shows the cross sections for the most important physics processes at Belle II [9], as well as their rates in a time window of 60 µs at the original full design luminosity of $\mathcal{L} = 8 \times 10^{35}\,\mathrm{cm}^{-2}\,\mathrm{s}^{-1}$. While one TPC drift volume is equivalent to approximately 30 µs, for the overlay it is important to consider the rate in a time window twice as large, since events which happen before and after the triggered $\Upsilon(4S)$ can overlap with the main volume. This idea is illustrated in Figure 10.1. This Figure shows three TPC volumes worth of drift. In Figure 10.1(a) the central volume, in which the signal $\Upsilon(4S)$ event takes place, is marked in purple, and its interaction point is a red dot. This purple area represents the volume in which tracks from this event which passed the trigger can occur, in other words, it is the volume one is interested in. Figure 10.1(b) shows two additional events which take place close in time. For the sake of this illustration they are of no further interest. One event took place before the triggered event and is therefore at a lower z-coordinate (equivalent to earlier time) while the other happened after the interesting event, with a higher z coordinate (later time). Those fringe events are placed such that only a few tracks actually overlap with the main volume. If their interaction point lies closer to the interaction point of the main event, the overlap will be considerably larger. In Figure 10.1(c) the

Physics process	σ/nb	Events per 60 μs	Tracks per event	Tracks per 60 μs
Υ(4S)	1.110±0.008	0.0533±0.0003	11	0.59
Bhabha	300±3	14.4±0.1	2	28.80
$u\bar{u}$	1.61	0.077	8	0.62
$d\bar{d}$	0.4	0.019	8	0.15
$s\bar{s}$	0.38	0.018	8	0.15
$c\bar{c}$	1.3	0.062	10	0.62
$\gamma\gamma$	4.99±0.05	0.240±0.002	4	0.96
$\mu^+\mu^-$	1.148	0.055	2	0.11
$\tau^+\tau^-$	0.919	0.044	2	0.09
$e^+e^-e^+e^-$	39.7±0.1	1.9056±0.0005	4	7.62
$e^+e^-\mu^+\mu^-$	18.9±0.1	0.9072	4	3.63

Table 10.1: Cross sections for physics processes [9] and the resulting rate for a time window of 60 μs with a rough estimate for the number of tracks in each process type [17], [40]. Number of tracks per 60 μs does not include acceptance of the TPC. Highest contribution in background tracks is to be expected from Bhabha scattering and 4ℓ final states.

color marks the region where there can be an overlap of track with the main event. Of course, if the interaction point falls into the purple region of the main event, the overlap will be very large. But also events with interaction point in the blue region can have an overlap. In total the colored area is two TPC volumes long, which is about 60 μs.[1]

Table 10.1 also shows a rough estimate for the number of track for each physics events which mostly was obtained from detector simulation of 10 000 events [40]. Based on this and the rate per 60 μs it is possible to calculate an estimate for the average number of tracks one expects to see in the TPC volume. Its value is 43.34, the error has been omitted due to the inconsistency in the errors for the cross sections. One should take into account that this number is based solely on cross sections and luminosity, there are no considerations for the acceptance of the TPC. Therefore, the case for the real TPC could be lower.

With the correct event rates the overlay of physics events can be accurately carried out.

10.2 Creating the Overlaid Data

In the first approach, beam backgrounds are not included in the overlay. One Υ(4S) event, which it is assumed has been triggered on, is placed manually at time t_0 central in the triggered volume, which encapsulates the entire Υ(4S) event. For each physics process in Table 10.1 including Υ(4S) events, the number of events to be placed close in time to the triggered event is generated using a Poisson distribution with the number of events per 60 μs as the mean value. The corresponding number of events for each process is then randomly selected from the set of generated separate events for each process, while ensuring that no event is picked multiple times.

---

[1] In the illustration the colored regions are based on the interaction point of the event instead of the arrival time of the earliest hits of the signal event which is the base for the z-coordinate
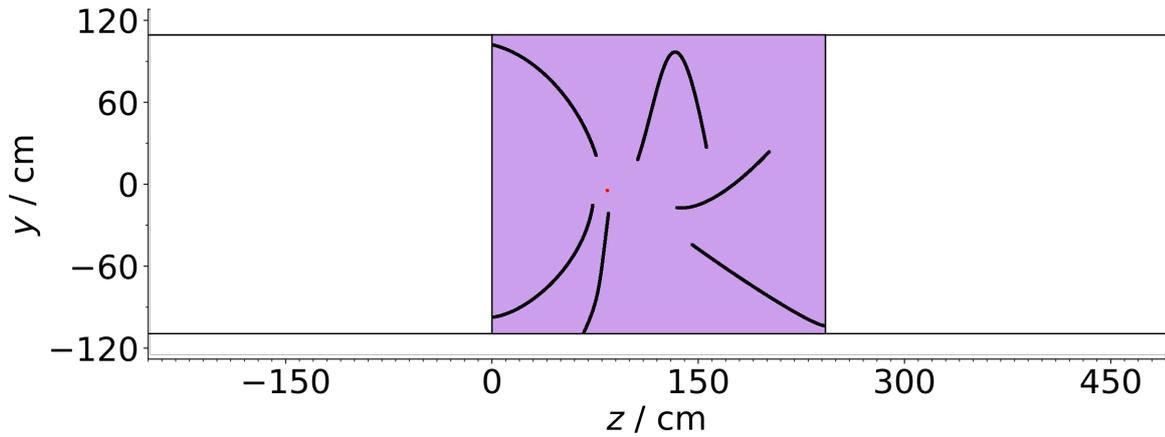
(a) TPC volume of a triggered $\Upsilon(4S)$ event in side-view. Area in which tracks from this event can occur are colored purple
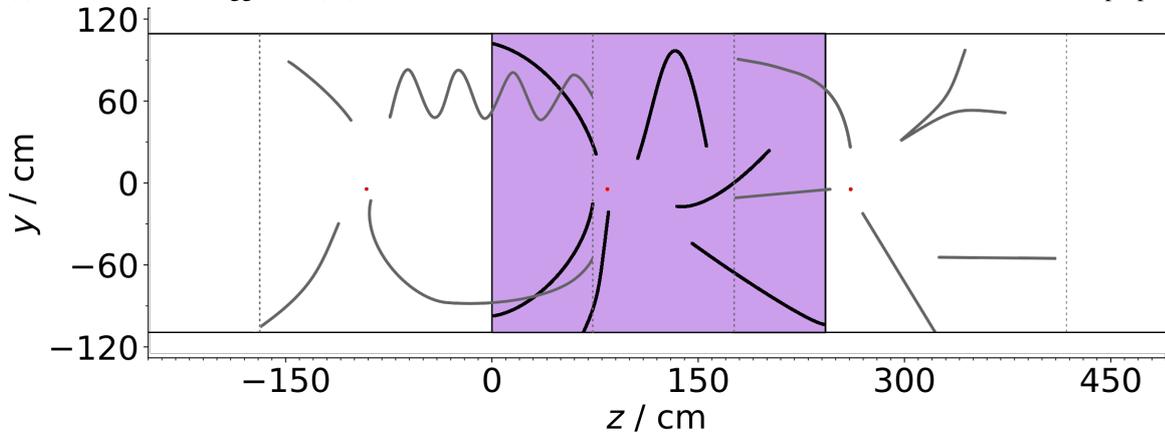
(b) TPC volume of triggered $\Upsilon(4S)$ event with additional events that took place earlier and later (hits and corresponding TPC volume in gray)
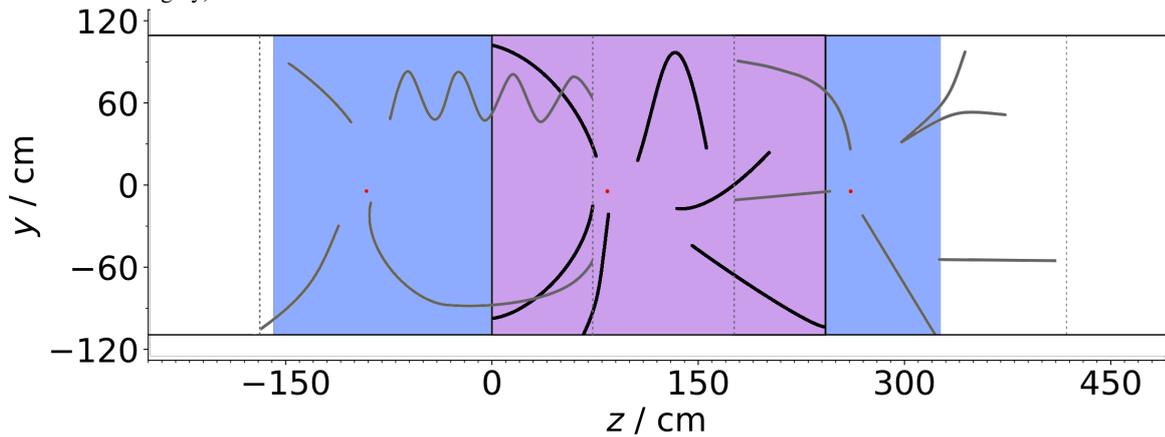
(c) TPC volume of triggered $\Upsilon(4S)$ event with additional events. Events with interaction point in colored area (blue or purple) can have overlapping tracks with the main $\Upsilon(4S)$ event

Figure 10.1: Illustration of the time frame in which overlap with the triggered volume can take place

From the event files the relevant information, like the Hit coordinates, GEANT4 trackID, and MC particle PDG code, is read. While the trackID and PDG code can be written into the output file directly, the coordinates have to be placed in time and be applied diffusion to.

As described previously, events which happen both before and after t_0 can have overlapping tracks in the TPC volume, therefore, the time window for placing the background events is in total two TPC volumes worth of drift, which are approximately $60\,\mu s$. This corresponds to $7\,454$ bunch crossings before and after t_0 assuming the time between bunch crossing to be $t_{bc} = 4.205\,ns$, which can be calculated using the circumference of the SuperKEKB accelerator $C = 3\,016.315\,m$ and the number of bunches in the accelerator $n_b = 2\,500$ [10]. This value is using the original design luminosity of $\mathscr{L} = 8 \times 10^{35}\,cm^{-2}\,s^{-1}$, which since then has been updated to the more moderate goal of $\mathscr{L} = 6.5 \times 10^{35}\,cm^{-2}\,s^{-1}$ [16], [11]. The studies are done with the original design luminosity.

Before the hits are placed randomly in time by generating a random integer in the range of -7454 to 7454 denoting the bunch crossing index, the diffusion is applied. This has to be done before-hand since after placing the event to a certain time stamp the z-coordinate will be transformed to a value relative to t_0 and is therefore no longer a good measure for the drift length. As implemented in the TPCDigitizer, the hits which would diffuse outside of the TPC volume in radial direction are considered lost. Since the event overlay deals with a continuous volume, this loss is not implemented for longitudinal diffusion. This allows for hits to diffuse into or out of the main volume in z-direction.

10.3 Event Overlay Display

In order to develop a good understanding of event overlap in the TPC volume, it is helpful to visualize the overlap. Such a display would show tracks of all events taking place during the time window of the triggered Υ(4S) event, in a way such that different contribution can be easily distinguished. With the intention to illustrate the idea of events overlapping with the triggered volume, the display in Figure 10.2 shows not only the main volume containing the Υ(4S) event, but also the two TPC volumes adjacent to the triggered volume. The different background processes are categorized by interaction and color-coded. The events are additionally split up by event type and displayed separately in Figure 10.3.
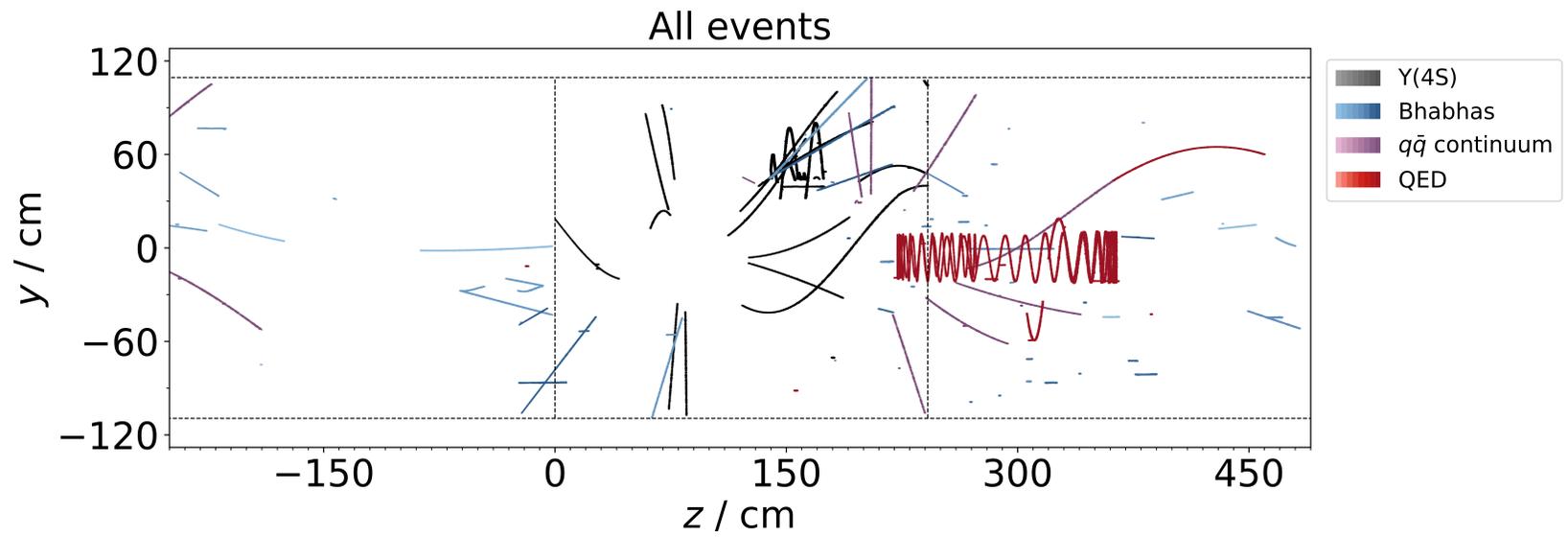
Figure 10.2: Event overlay display with triggered $\Upsilon(4S)$ event in the central volume
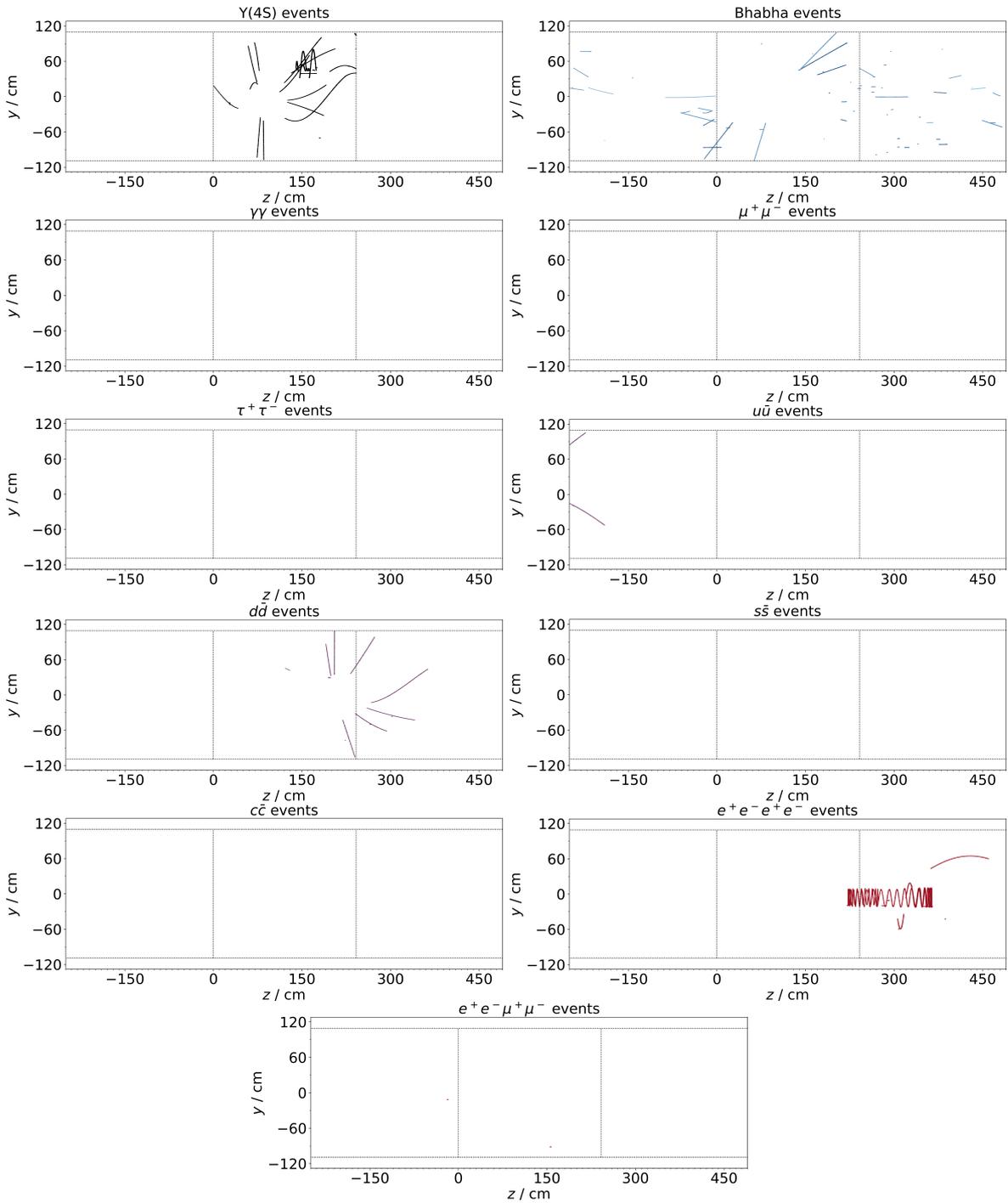
Figure 10.3: Contribution to overlay from each physics process shown separately

In order to visualize the entire extent of the overlaid events, the background events were also placed in regions where there can be no overlap in tracks with the triggered central volume. Otherwise the edges of the outer TPC volumes would have looked deceptively empty.

42

(a) Sum of tracks from different processes

(b) Close-up of the sum of tracks from different processes, excluding most contributions from QED events
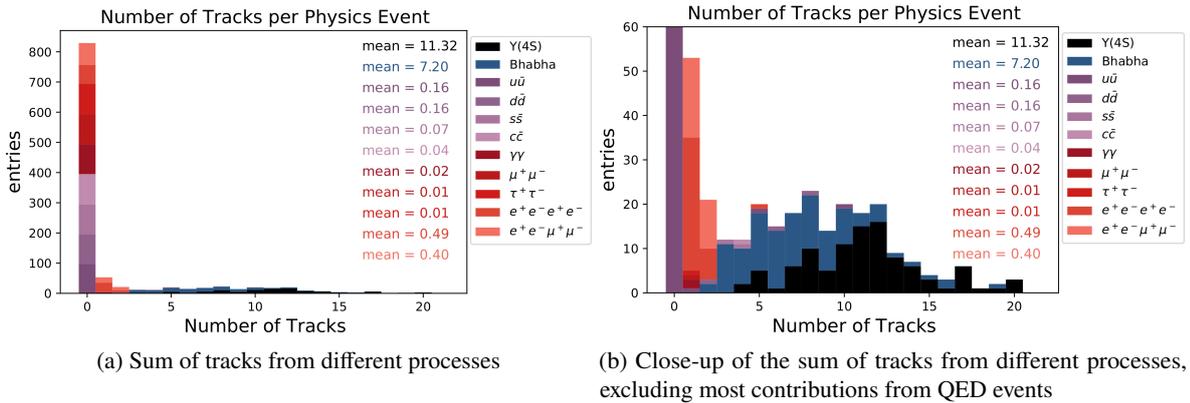
Figure 10.4: Sum of tracks in triggered TPC volume for all physics processes in Table 10.1. Mostly no tracks from QED or $q\bar{q}$ events in the TPC, but large contribution from Bhabha scattering events.

More examples for event overlay displays can be seen in Appendix B.

10.4 Track Rate

Using 100 overlaid events, an estimate for the number of tracks for each physics process in a TPC volume, triggered on an $\Upsilon(4S)$ event, can be determined. The data is limited to the region of the main TPC volume and subsequently the number of unique tracks, using unique combinations of the GEANT4 trackID and the physics process type as well as the event index in the set, is counted.

In order to avoid counting tracks from δ electrons which receive their own trackID in GEANT4 there is a strict cut on the trackID for electrons. The GEANT4 trackID starts at 1 for the primary particles and counts up for all secondary particles. For Bhabha events the cut on the trackID for electrons specifically is ≤ 2, only allowing for the primary scattering electrons to be counted. For all other events the cut for electron trackID is ≤ 4 meaning that the electron needs to be a primary or one of the first secondary particles. This cut is chosen with having the 4ℓ events in mind, but it also means that some secondary electrons from other events like the $\Upsilon(4S)$ are not counted. Therefore, the result for the number of tracks for those events will be slightly too low, however, compared to the amount of δ electrons this is a minuscule effect.

The resulting distributions are shown as stacked histogram in Figure 10.4. The corresponding mean values represent the number of tracks including TPC acceptance assuming that is has been triggered on a $\Upsilon(4S)$ event. Most of the times there are no tracks from continuum and QED events while there are consistently more than 2 tracks from all the Bhabha events happening simultaneously in the TPC volume.

Of further interest is the total number of tracks in the volume, including and excluding the tracks from the signal $\Upsilon(4S)$. These distribution for the 100 overlay-events can be seen in Figure 10.5. From this one can tell that approximately 10 tracks need to be filtered by a track finding algorithm.
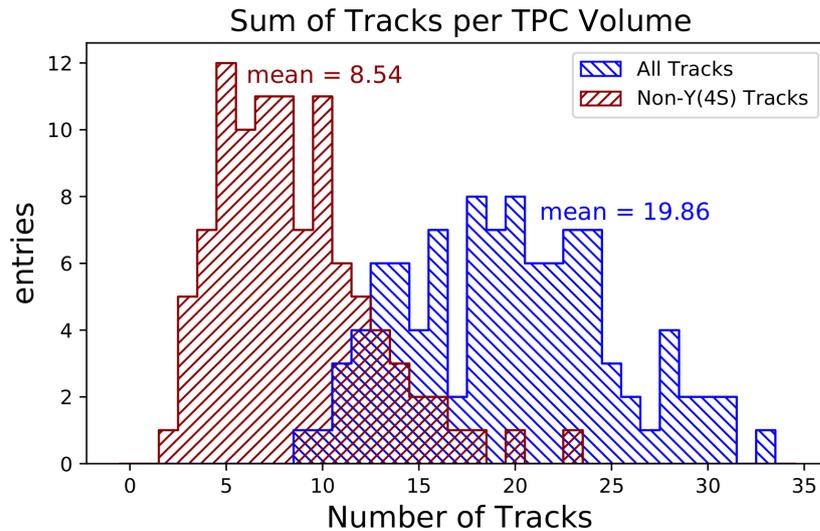
Figure 10.5: Total sum of tracks in the triggered TPC volume including and excluding the Υ(4S) tracks

10.5 Track-Event Association

A track finding algorithm has not yet been implemented for the TPC. One of its main tasks, apart from finding the tracks, is to assign the tracks to the correct event (bunch crossing). One way this information can be obtained is by using the result for the vertex reconstruction from the track fitter. However, this approach only works for tracks pointing towards the interaction point.

Another way to assign tracks to events which works for all tracks is to use the width of the track due to diffusion since this will depend on the drift length and not directly on the reconstructed z-coordinate. The former is reconstructed by measuring the drift time of the electrons from the ionization. This requires a trigger signal for starting the measurement. A track which has been drifting in the TPC for some time might therefore have the same reconstructed z-coordinate as a track from the triggered event, but will have additional drift length which is not measured. Since the width of the diffused track depends only on the drift length, this can then be used to correctly distinguish between events. This idea is illustrated in Figure 10.6. For overlapping tracks it shows the effect of diffusion on the width of track based on the drift length.

10.6 Beam Background

For an accurate representation of the conditions in a Belle II TPC beam backgrounds have to be included. There are three types of relevant beam background which can come from both beam lines, HER and LER.

Touschek Scattering

Touschek scattering is the scattering of two electrons (or positrons) within one bunch [41, 42]. While scattering the electrons convert a small transverse momentum of the particles into a large longitudinal momentum. Those particles are then lost since one will have too large of a momentum, while the
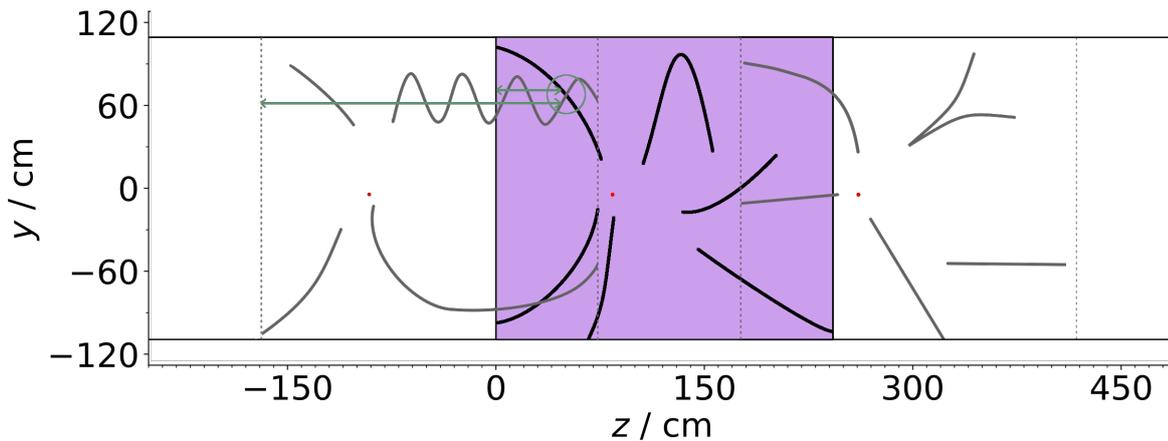
(a) Overlapping tracks with different drift length (marked in green)
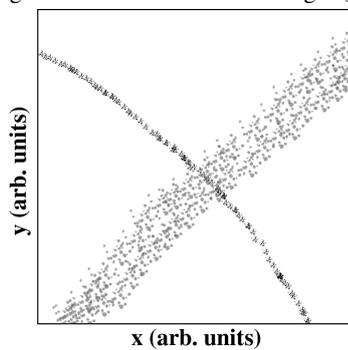
(b) Close-up of diffused tracks in $x-y$ projection (green circle)

Figure 10.6: Illustration of the effect of diffusion on overlapping tracks with different drift lengths. The gray track belongs to an earlier event and has therefore a large drift length. The black track belongs to the triggered event and has a short drift length. Based on the diffusion one can distinguish the tracks even though they have the same reconstructed z coordinate (provided that drift time measurement starts with the trigger for the central (black) event).

other has too little. Eventually, they will hit the beam pipe where they can generate a particle shower. If this happens close to the interaction point the shower can leak into the detector.

Beam-gas Scattering

Due to elastic Coulomb scattering with the residual gas in the beam pipe the particles in the accelerator can experience a change in their momentum [43]. This type of background is also referred to as Coulomb background. Again, these particles are lost from the bunch and can hit the beam pipe near the detector which picks up the particle shower as background.

Bremsstrahlung

Bremsstrahlung background is likewise an interaction of the bunch particles with residual beam gas [43]. In this case, inelastic scattering due to deflection in the electric fields of gas nuclei causes the

Background process	Rate in MHz	Events per 60 μs
Brems HER	2.46479	147.89
Brems LER	8.2928	497.57
Coulomb HER	16.335	980.10
Coulomb LER	191.641	11 498.46
Touschek HER	0.242353	14.54
Touschek LER	119.409	7 164.54

Table 10.2: Rate for background processes and the resulting rate for a time window of 60 μs. Highest contribution in beam background is to be expected from Coulomb and Touschek scattering in the LER

particles to emit Bremsstrahlung. If the energy loss is large, the particle is over-bent by the focusing magnets and in term hits the beam pipe and is lost.

The background files for the TPC have been created using input files from the Belle II BG19c campaign. The rates for the used backgrounds in Table 10.2 have been taken directly from these input files. The overlay for the beam background follows the same procedure as the physics event background. In this case however, the beam background is only placed in time regions where actual overlap with the main event can occur, in order to keep the amount of hits placed at a reasonable level. For this reason, the outer edges in Figure 10.7 are not filled with background hits.
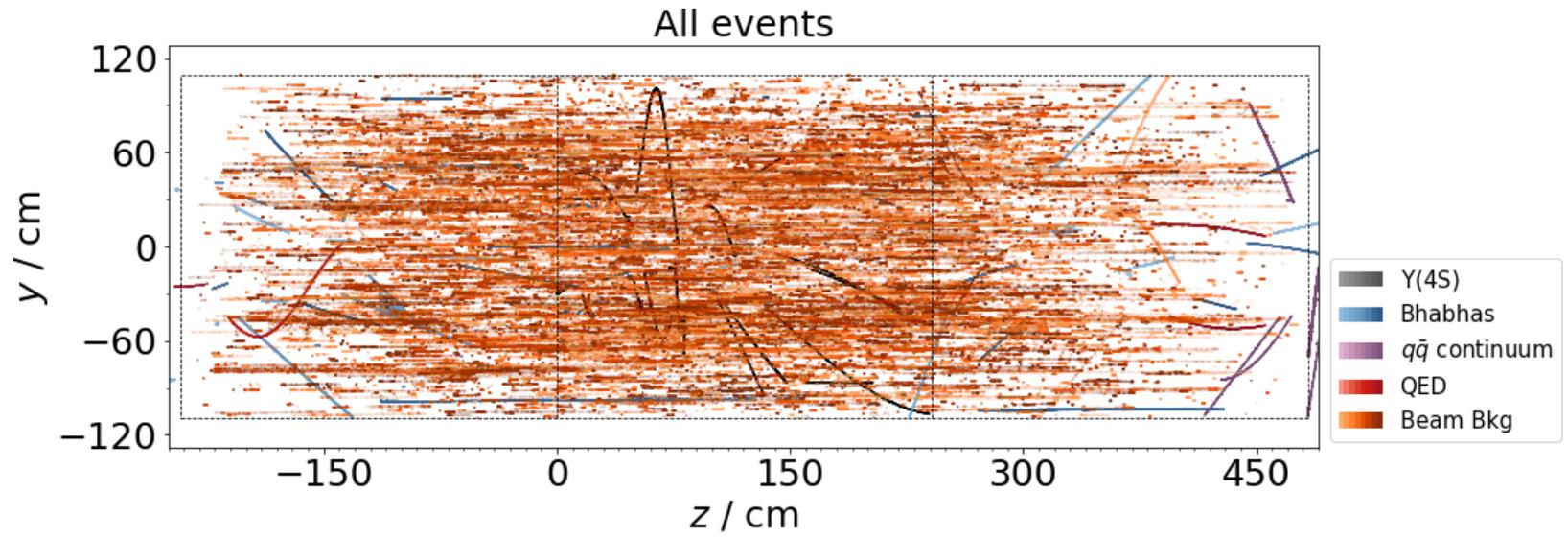
Figure 10.7: Side view of TPC overlay with beam background

As expected from the rates in Tables 10.1 and 10.2 the beam background dominates the amount of hits. This can be problematic if the charge density within the TPC becomes too large, thus creating field distortions. Furthermore, these beam background hits potentially increase the data throughput of the TPC drastically.

The number of hits can be investigated by repeating the study from section 10.4 counting the number of hits in one TPC volume (30 µs of drift), instead of the number of tracks. This was done with a sample of 23 files, since it was quite computationally expensive to create the overlay files including beam background.
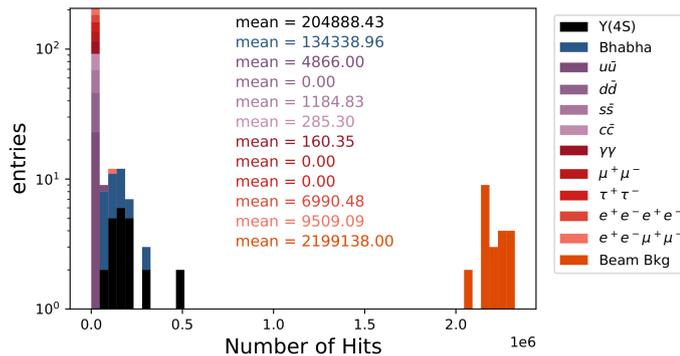
Figure 10.8: Histogram of the number of hits in one TPC volume, dominated by beam background.

The resulting plot showing a histogram of the number of hits appearing in the TPC volume from each source can be seen in Figure 10.8. The beam background contribution dominates the number of hits by roughly a factor of ten. Summing all contributions the total number of hits in one TPC volume (with a signal Υ(4S)) is about 2.5×10^6.

Large amount of hits are not desirable in a TPC, since the space charge can distort the electric field and thus incriminate the drift length-to-drift time relation, effectively worsening the spatial resolution. This space charge is mainly created by ions since they have a lower mobility in gas and therefore occupy the drift volume for a longer time [3].

Using the overlay with beam background, an estimate for the number of ions in the drift volume can be made.

10.6.1 Ion Density

Since the amount of beam background for the upgrades of the collider are unknown, the calculation of the ion density is done with a safety factor of ×5 of beam background. What ×5 beam background looks like in the overlay can be seen in Figure 10.9. This plot is only for illustration purposes. The actual calculation was done with 21 files with normal background where the amount of hits was multiplied by 5, since the computational time and effort was too high to produce multiple files with ×5 background.

The ion density in the drift volume depends in large part on the ions created in during the readout amplification drifting back into the drift volume for the electrons. To calculate the ion density one needs some first-order assumptions for readout parameters. In this case, the gain and the ion back-flow for the GridPix are needed. For the calculation a operational gain of 2 000 is assumed, while the ion back-flow is assumed to be 1 % [37].
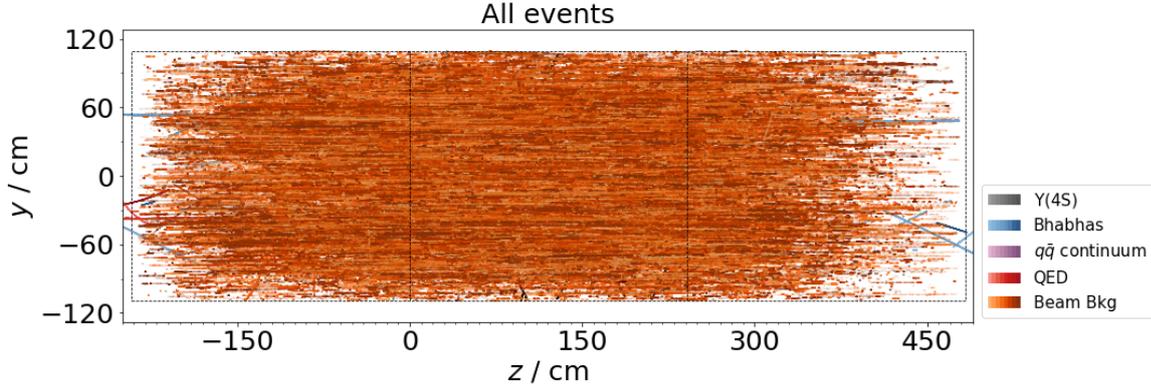
Figure 10.9: TPC with ×5 beam background for illustration purposes
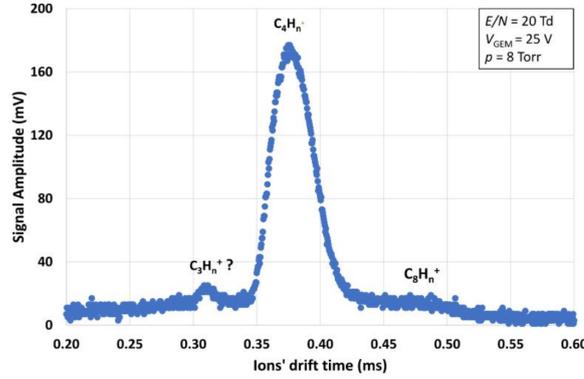
Figure 10.10: Typical drift spectrum for ions from the T2K gas mixture at $p = 8$ Torr [44].

According to Ref. [44] the ion drift for the T2K gas mixture at atmospheric pressure is dominated by $C_{12}H_n^+$ clusters from isobutane ($iC_4H_n^+$). In Ref. [44] the test of ion mobility were done in a pressure of 8 Torr, where the dominating ions were $C_4H_n^+$, which form $C_{12}H_n^+$ in atmospheric pressure. Figure 10.10 shows the drift spectrum of the T2K gas mixture at a pressure of 8 Torr. The measured mobility was $\mu = 2.14\,\mathrm{cm^2\,V^{-1}\,s^{-1}}$. Assuming ideal gas this scales to $203.3\,\mathrm{cm^2\,V^{-1}\,s^{-1}}$ at atmospheric pressure. In an electric field of $289\,\mathrm{V\,cm^{-1}}$ this equates to a velocity of $587.537\,\mathrm{\mu m\,\mu s^{-1}}$. This means that the back-drifting ions from the amplification of one TPC volume ($30.75\,\mathrm{\mu s}$) reach $1.763\,\mathrm{cm}$ into the drift volume. In this disc they have a number density of $4\,633.628\,\mathrm{cm^{-3}}$, or a charge density of $\rho = 0.742\,\mathrm{fC\,cm^{-3}}$.

There is no direct way of telling whether this is tolerable since neither the electric field nor distortions from ions are simulated for the drift. But one can compare this to charge densities in other TPCs. For the LCTPC there are not any confirmed results for the charge density including beam background and ion back-flow. Therefore, these values are compared to the charge density of the PANDA TPC [45]. Figure 10.11 shows the expected charge density in the drift volume. In equilibrium the charge density lies in the range of 20 and $65\,\mathrm{fC\,cm^{-3}}$. Therefore, the value $0.742\,\mathrm{fC\,cm^{-3}}$ seems to be acceptable for operating a TPC.
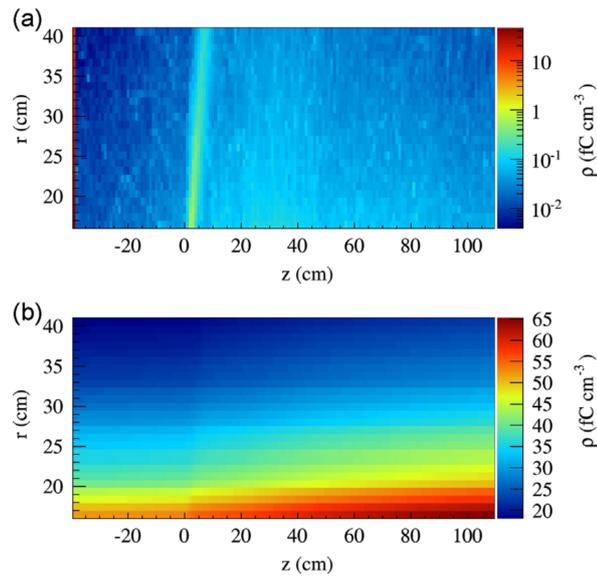
Figure 10.11: Charge density in the PANDA TPC [45]: a) shortly after an event (disk of charge at $z = -40\,\mathrm{cm}$). b) final equilibrium.

The PANDA TPC uses a triple GEM stack for the amplification with the goal of achieving $150\,\mu\mathrm{m}$ spatial resolution in $x - y$-direction. They experience an ion back-flow of $0.25\,\%$ corresponding to 4 back-drifting ions per electron at a gain of $2\,000$.

10.7 Simple Background Rejection

While the charge density might not be a limiting factor for operating the TPC, the conditions presented in Figure 10.7 are extremely difficult for tracking. However, the beam background hits in Figure 10.7 mainly produce micro-curlers as tracks. Those tracks are fairly easy to identify since they are mostly horizontal in z-direction and isolated in the $x - y$-projection, as is showcased in Figure 10.12.

Identifying micro-curlers and removing them from tracking is a common process in track finding for TPCs [34]. Here, a first implementation of a pattern recognition algorithm by Christian Wessel is presented [31]. Since this a only a proof-of-concept, this method of rejection is called `SimpleBackgroundRejection`.

10.7.1 Pixel Dead-Time

The goal is to implement a background rejection which is oriented on the readout structure such that it can be implemented on a hardware level. For this purpose, the readout structure and some of its parameters have to taken into account in the event overlay code. This allows for testing some of the readout parameters which have not been considered before. Of special interest is the pixel dead-time from processing the signal from the electrons arrival at the readout chip. The Timepix3 chip measures charge by counting the number of clock cycles where the signal exceeds a set threshold [27]. If hits arrive at the same pixel close in time, they extend the amount of time the charge is exceeding the threshold such that no new measurements can be started, hence creating dead-time for the pixel.
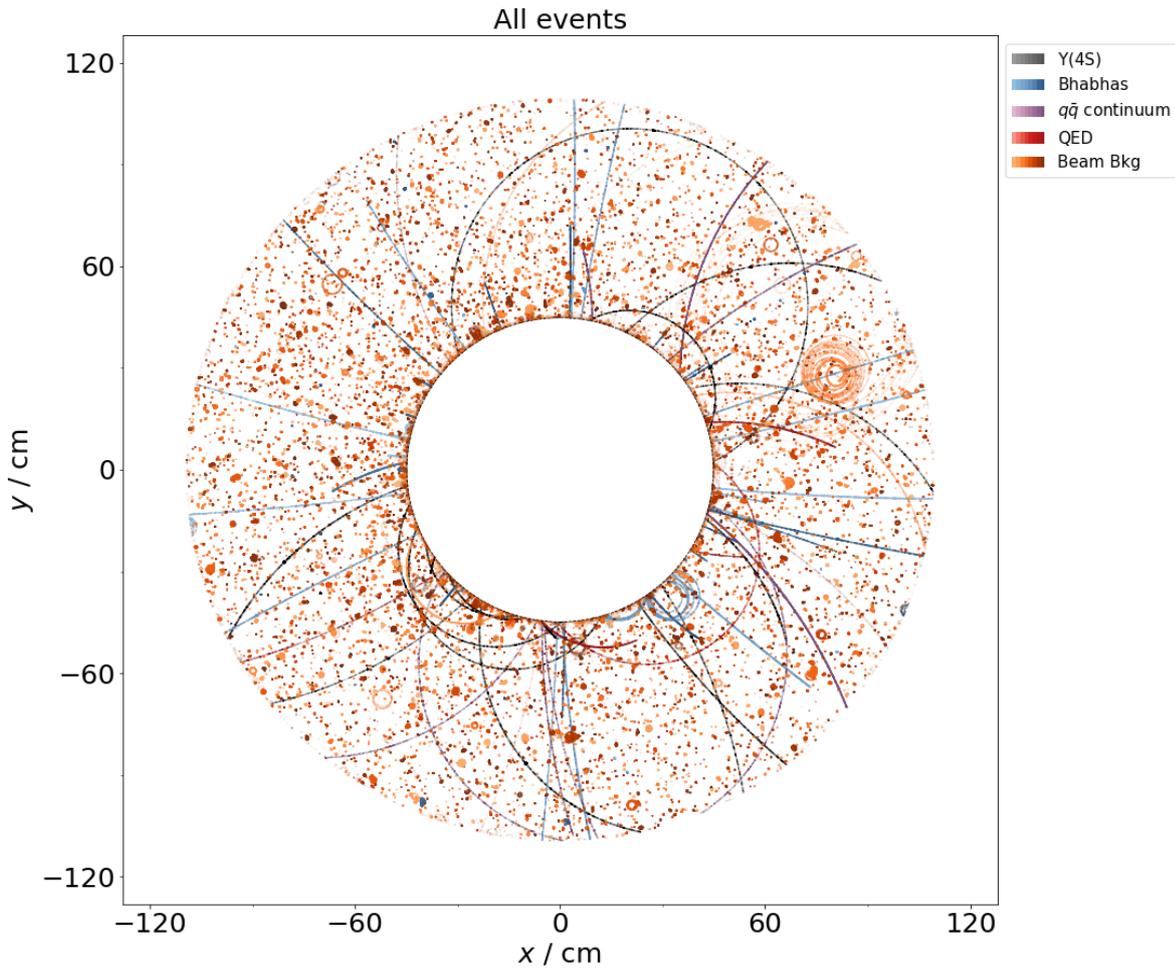
Figure 10.12: Front view of TPC overlay with beam background

The dead-time varies between pixel designs. For the Timepix3 chip, a dead-time in the order of 1 µs can be assumed [37]. The effects of dead-time are thus tested for dead-time values of 500 and 2 000 ns. Naturally, the hit efficiency also depends on the pixel size and pitch. In Timepix3 the pixel size is 55 µm, for this study pixel sizes of 50, 200 and 1 000 µm were used. Since the effect of pixel dead-time is to be studied, other charge loss effects like recombination during drift and field distortions close to the TPC wall or due to slow ions are not included in this study.

The hit efficiency for the TPC can be defined as

$$\epsilon_{\text{hit}} = \frac{\text{registered hits}}{\text{total hits}},$$

but a large number of hits lost to dead-time will belong to micro-curler from beam background which are mostly not interesting for physics analyses. Therefore, the hit efficiency is defined as the fraction

of hits from the triggered event which are registered. In this case the triggered event is always the $\Upsilon(4S)$ event:

$$\epsilon_{\text{hit}} = \frac{\text{registered signal } \Upsilon(4S) \text{ hits}}{\text{total signal } \Upsilon(4S) \text{ hits}}.$$

This was then calculated using 20 files for each combination of dead-time and pixel size. The results for the hit efficiency can be seen in Figure 10.13. As expected the hit efficiency decreases for a larger dead-time. It is very interesting to see that the hit efficiency does not decrease by a large amount for large pixel sizes. Having a large pixel size with a negligible effect on hit efficiency, and by extensions on the dE/dx resolution, can greatly reduce the number of readout channels. However, large pixels might have an effect on other physics deliverables like the p_T resolution. This is investigated further in chapter 12.
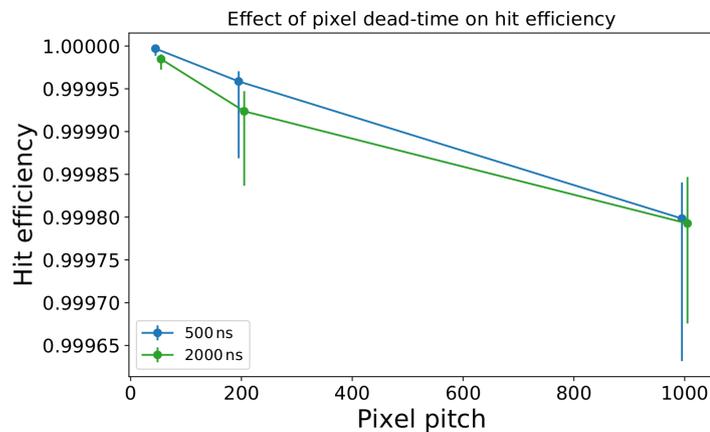
Figure 10.13: Hit efficiency for $\Upsilon(4S)$ hits in the TPC volume including effects from pixel dead-time. For visualization the data points are slightly shifted in the x-axis.

However, the dead-time is not the only source of hit loss. By definition, the background rejection is designed to discard large number of hits. So apart from testing the effectiveness of the rejection method, the effect on hit efficiency has to be tested as well.

10.7.2 Algorithm for Background Rejection

This algorithm was implemented by Christian Wessel [31]. It is showcased there nonetheless, because it is a important result for tracking in the TPC. The algorithm is based on dividing the TPC volume into $2 \times 2 \times 2\,\text{cm}^3$ cells and conducting a neighbor search for those cells. Cells including their hits can then be rejected if they are connected in z in one spot (micro-curlers) or completely isolated (energy deposits by photons [39]). The size of the cells is inspired by the size of the GridPix readout chip [27]. Having a crude but simple method of identifying micro-curlers allows for this rejection method to be applied at the hardware level. In this case most of the hits from the micro-curlers do not need to be read out, significantly reducing the data throughput.

(a) TPC volume with beam background hits before applying `SimpleBackgroundRejection`

(b) TPC volume after applying `SimpleBackgroundRejection`
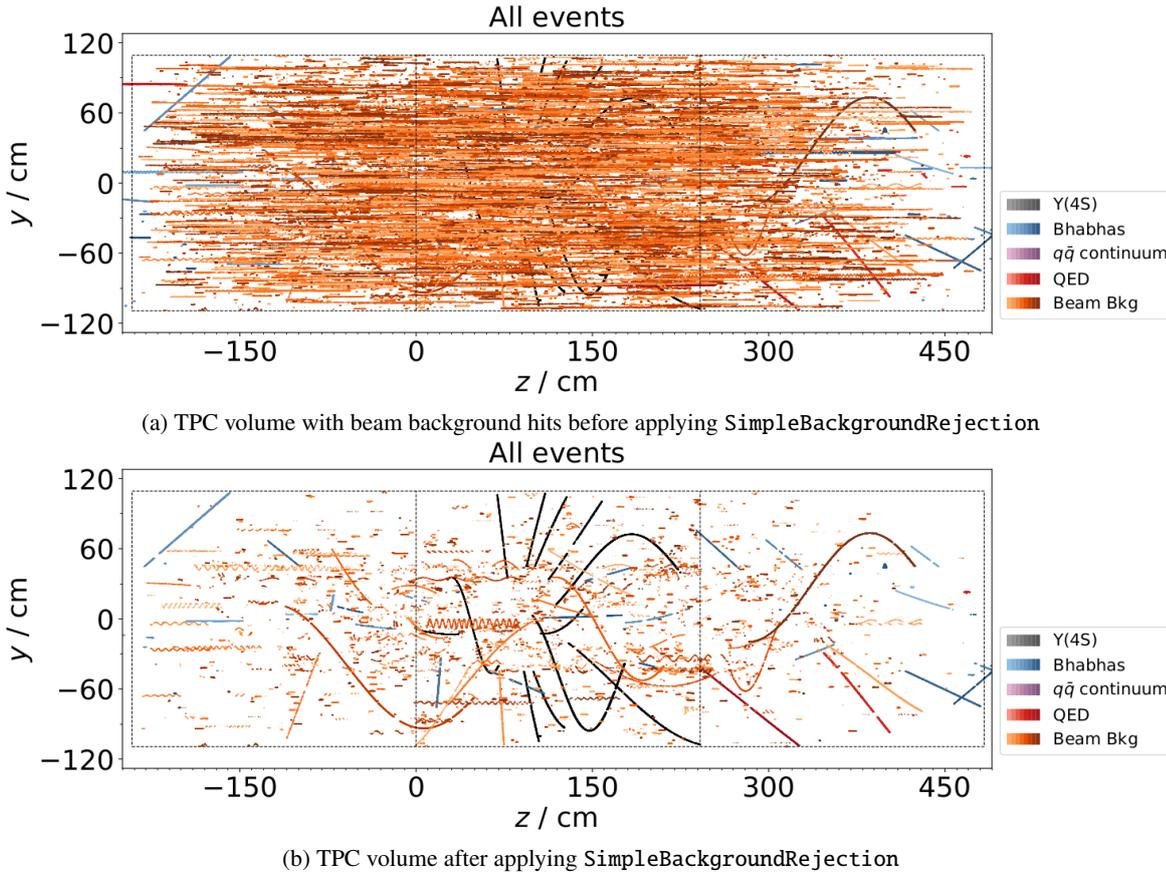
Figure 10.14: Demonstration of the `SimpleBackgroundRejection`. Majority of background hits are removed, revealing underlying events.

Figure 10.14 demonstrates the effect of the `SimpleBackgroundRejection`. As showcased, the majority of background hits are correctly removed and the tracks from the physics events are left. The background rejection efficiency, which is defined as

$$\epsilon_{\text{SBR}} = \frac{\text{No. of beam background hits rejected by } \texttt{SimpleBackgroundRejection}}{\text{Total no. of beam background hits}},$$

has value of $\epsilon_{\text{SBR}} = 0.928^{+0.03}_{-0.07}$ which calculated by averaging over 20 files of overlay.

Some of the limitations of the `SimpleBackgroundRejection` are also visible in Figure 10.14(b). Large micro-curlers spreading over more than one cell in $x - y$ are not removed. Additionally, a few hits from tracks of the $\Upsilon(4S)$ event are lost, presumably because there was a micro-curler in the same cell. Since this is a first approach to rejecting micro-curlers from beam background, solutions for these limitations have yet to be designed. As a proof-of-principle this method clearly shows a promising solution to the problem of beam background micro-curlers.

Applying this method of rejection might have a considerable effect on the dE/dx resolution, since it reduces the hit efficiency. Therefore, the hit efficiency including the losses from the `SimpleBackgroundRejection` are studied next.

10.7.3 Hit Efficiency Including `SimpleBackgroundRejection`

For the hit efficiency including the losses from the losses from the `SimpleBackgroundRejection` the same definition as for the pixel dead-time (section 10.7.1) is used, by only considering the hits from the signal ($\Upsilon(4S)$) event. In principle, the hit efficiency can be studied for various pixel sizes, like in section 10.7.1, however since the rejection of hits is done on the cell level, the pixel size plays a very little role in the hit efficiency. Therefore the hit efficiency is calculated for a pixel size of $200\,\mu m$ averaged over 20 overlay files. The result for the hit efficiency is $0.75^{+0.03}_{-0.06}$. Again, only charge loss from the `SimpleBackgroundRejection` and pixel dead-time are taken into account for quantifying these effects contribution to the hit efficiency.

The hit efficiency after `SimpleBackgroundRejection` decreases a lot compared to the hit efficiency in section 10.7.1. This is not surprising, since the `SimpleBackgroundRejection` rejects hits in entire $2 \times 2 \times 2\,cm^3$ cells instead of individual pixels. A hit efficiency of 75 % is likely not sufficient for operating the TPC [21]. Therefore, this rough rejection method needs further optimization. Based on studies for the LCTPC it should be possible to achieve $\epsilon_{SBR} = 0.99$ while only losing 3 % of signal hits [46].

The `SimpleBackgroundRejection` works effectively for removing small micro-curlers from the data, however, the micro-curlers still produce a large amount of hits in the TPC volume. While the ion density does not seem to be a limiting factor (section 10.6.1) it is not desirable to have this large amount of hits present in the drift volume. However, the amount of hits created by the micro-curlers might not be entirely accurate since the electric field responsible for the drift was not included in the simulation so far. Its inclusion should have a net effect on the micro-curlers. This study is the content of chapter 11.

Electric Field & Simulation Anomaly

In the first stages of the analysis the simulation did not include any simulation of electric field for the TPC. The drift of the electrons from the ionization to the readout plane was not simulated, but modeled since the drift properties of the gas are well known. Primary particles are high energetic enough and spent so little time that the effect of the electric field could be neglected.

However, due to the occurrence of the micro-curlers it was of particular interest to see the effect of the electric field on the amount of charge deposition from said micro-curlers. Therefore, the operational field value of $E_D = 289\,\mathrm{V\,cm^{-1}}$ was included into the simulation.

11.1 Expected Effect

Since section 10.6 established that the micro-curlers from beam background are a major source of background hits, this particular study set out to investigate whether the electric field could decrease the number of hits deposited by micro-curlers. Figure 11.1 illustrates the desired effect of the electric field on a micro-curler from an electron. The beam backgrounds hits consist of roughly 97 % electrons, 1 % positrons and the rest comes from atoms from the gas.

Due to the acceleration of the secondary electrons in the z direction, the path of the micro-curlers would be significantly shortened, thus leading to less charge creation and reducing the total number of hits in the drift volume.

For micro-curlers traveling in the opposite direction the electric field would act as deceleration, thus reducing their energy such that they stop producing hits earlier.

For positively charged micro-curlers (positrons from pair production) the effect would be the same in opposite direction. Once the positrons are stopped, recombination with an electron in the gas is likely [3].

11.2 Implementation

The electric field was implemented into the Geant4 simulation by creating a custom field manager which overwrites the global `basf2` field manager for the extend of the TPC volume. The implementation was done following the instructions in Ref [47]. There, a detailed description of the algorithms for computing the direction of a particle within an electromagnetic field can be found. The main idea
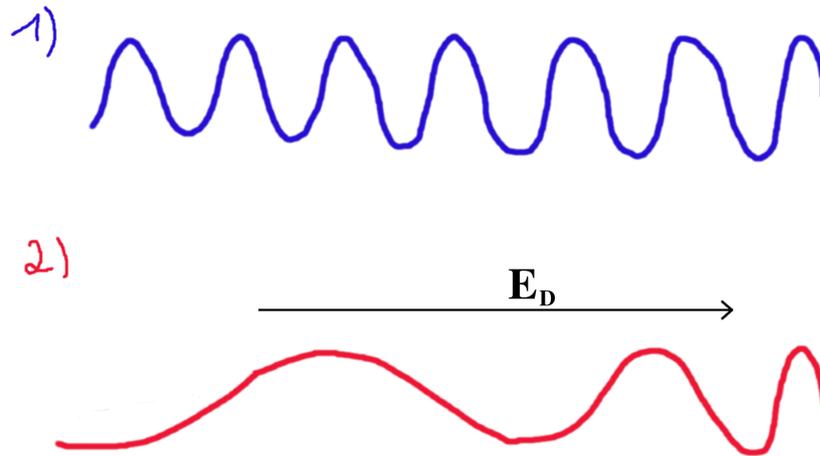
Figure 11.1: Possible effect of electric field on electron micro-curlers: 1) No electric field leads to large track length of the micro-curler.
2) With an electric field, the electron micro-curler will be accelerated in opposite direction, thus having a shorter path in the TPC volume leaving fewer hits.

is that a GEANT4 stepper integrates the equation of motion numerically. The equation of motion is generated automatically from the field values. There are several choices for the GEANT4 stepper, either general purpose steppers or steppers specialized for certain fields.

The electric field is implemented as completely homogeneous field with a field value of $289\,\text{V cm}^{-1}$ and the magnetic field from the Belle II solenoid is largely homogeneous at $1.5\,\text{T}$ [48]. For mostly homogeneous electromagnetic fields the fifth order Runge-Kutta stepper `G4DormandPrince745` is well suited [47]. Therefore, this stepper is used for the simulation.

11.3 Back-turners

The implementation was tested by simulating low energy muons with purely transversal momentum. The effect of the field could then be investigated by observing the muons movement in longitudinal direction.

When testing the properties of the electric field, strange processes could be observed. As seen in the side projection of the TPC in Figure 11.2(a), a $90\,\text{MeV}$ muon starts at a z-coordinate of 0, moves towards the backward endplate and the turns around at the end of the TPC and continues its path in the drift field. The drift towards the endplate is expected due to the electric field, however, it is not understood why the muon turns around and starts accelerating against the direction of the field. While multiple scattering can explain some changes in the direction of the muon, it seems unlikely that it would lead to acceleration against the electric field. Additionally, large scatters should be visible in the $x - y$-projection. As Figure 11.2(b) shows, there are no large kinks in the track in the $x - y$ projection.

Figure 11.3 shows the z-coordinate as a function of the energy deposition time. From this, one can tell that the muon is accelerated towards the readout plane, but then stops at around $80\,\text{ns}$ and turns back. From there, the muon is accelerated back towards the creation point with some deceleration along the way. It is not quite clear what could cause such behavior.

(a) Event where the muon turns around in the TPC drift volume

(b) $x - y$ projection of the same event with no major kinks in the track
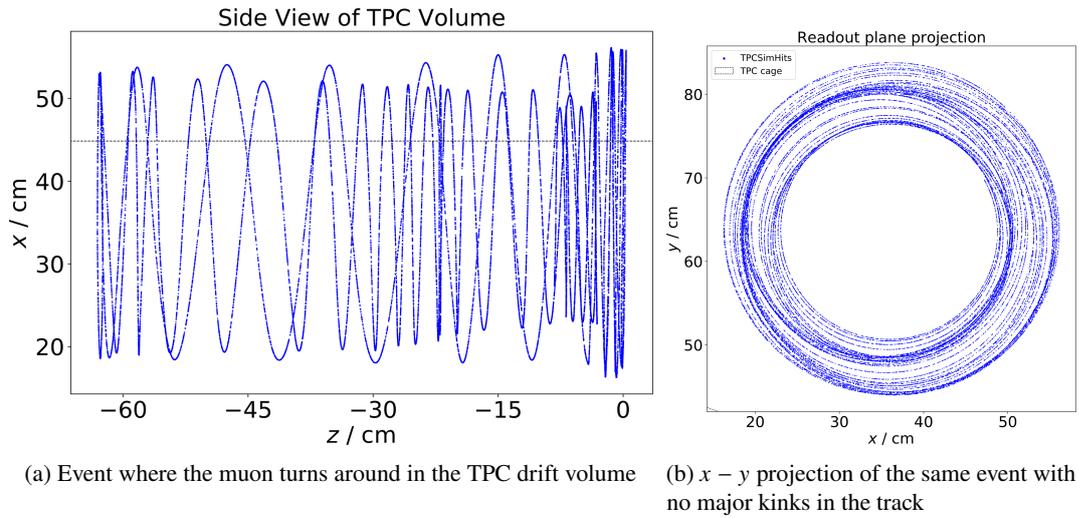
Figure 11.2: One example for a muon turning around unexpectedly in the TPC volume

(a) Event where the muon turns around in the TPC drift volume

(b) Visualization of temporal behavior of the z-coordinate. The turning around of the muon is clearly visible.
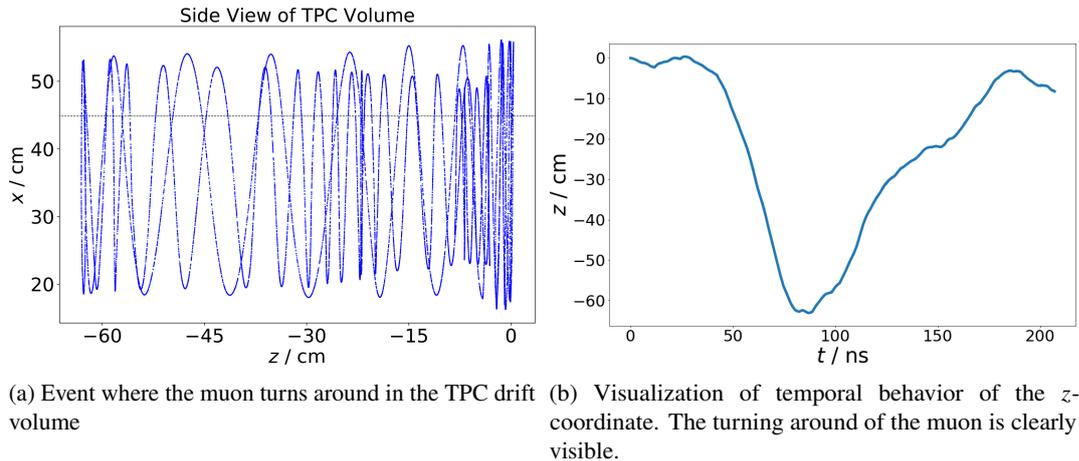
Figure 11.3: One example for a muon turning around unexpectedly in the TPC volume. This behavior was observed for multiple low energy muons. In GEANT4 the particles track ends when it has lost all its energy, since then it no longer can create hits.

Since the magnetic field is largely homogeneous and the electric field completely homogeneous it does not seem likely that the turn is due to edge field effects but rather the implementation of the field itself. Therefore, this process is investigated in more detail. For this purpose, a muon with no longitudinal momentum but only a transversal momentum of $90\,\mathrm{MeV}$ is simulated in the TPC for various scenarios.

11.3.1 GEANT4 Stepper

In GEANT4 the stepper is responsible for calculating the trajectory of the particle in the detector by numerically integrating the equation of motion [47]. For the implementation of the electric field in the `basf2` simulation a new GEANT4 stepper had to be specified, because the standard stepper for the

Belle II simulation is suited only for purely magnetic fields. Instead, the Runge-Kutta based stepper `DormandPrince` was used, which is said to be "efficient and robust" [47]. Since this represents a change in the simulation procedure, the stepper was investigated first.

Other steppers for electromagnetic fields recommended in Ref. [47] are tested, all of which are Runge-Kutta based. In order to properly compare the different values the same random-seed is used for each simulation. It should be pointed out here, that the behavior has been observed for a variety, but not all, of random-seeds.

To visualize the course of the particle track for different steppers, the muons position in z-direction is plotted against time t. This can be seen in Figure 11.4, which shows that all stepper yield the same numerical result. Since they are all Runge-Kutta based this does not come as a surprise. However, since these are the steppers officially recommended for electromagnetic fields, no further steppers have been tested, as this would have been out of scope for this project.
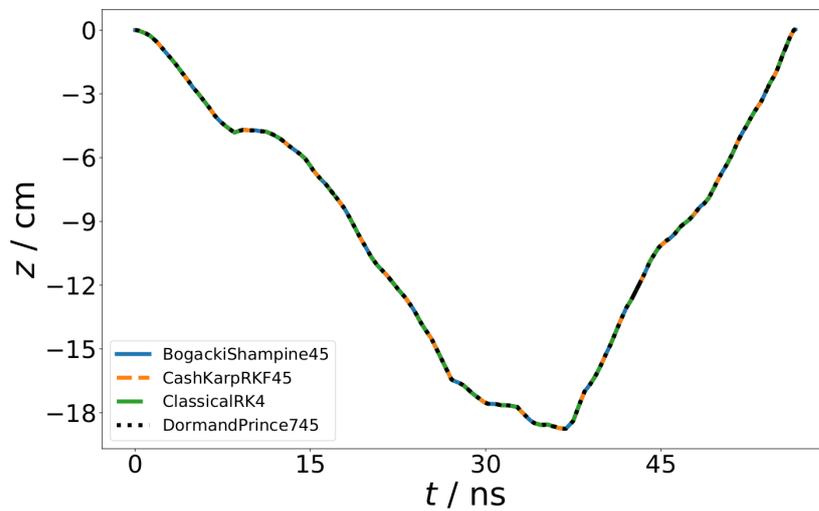
Figure 11.4: z vs. t for the same muon using different Runge-Kutta based GEANT4 stepper. Since the result is always the same, either a Runge-Kutta based stepper is not the right choice, which seems unlikely, or the problem lies elsewhere. Here, the muon does not reach the end of the TPC but instead turns around earlier.

11.3.2 Electric Field

Since using different steppers did not yield different results, the implementation of the electric field is reexamined as well. The muon is simulated for different strengths of the electric field and again compared in a z-vs-t diagram for the same random-seed. The field strengths in the legend of Figure 11.5 are given in units of V/cm. The entry "Electric0" denotes that the field is implemented with a field strength of $0\,\mathrm{V\,cm^{-1}}$, while for the entry "ElectricNo" the implementation for the electric field was completely taken out. In other words, the simulation was reversed to the state before the addition of the electric field.

As can be clearly seen in Figure 11.5, not only is this process independent of the electric field strength but also of the mere presence of the field. This indicates that this might not be a problem with the implementation of the electric field for the TPC after all, but is instead a more common observation.
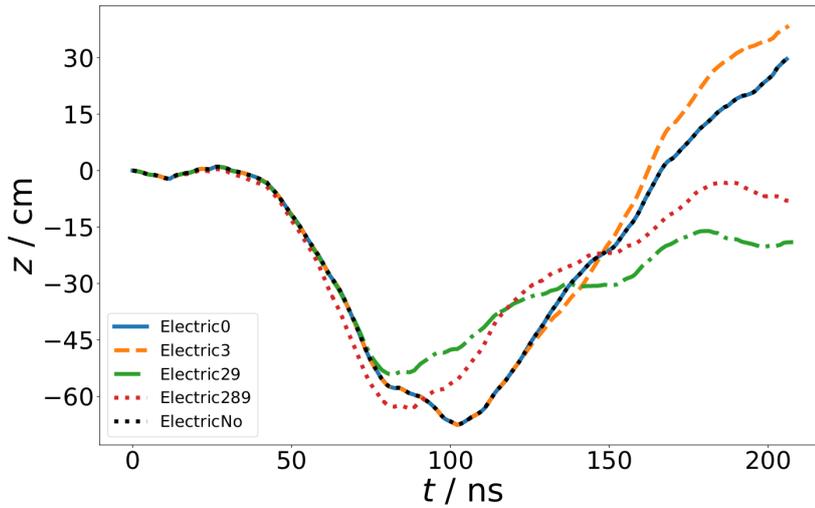
Figure 11.5: z vs. t for the same muon using different electrical field strengths. Entry "ElectricNo" indicates that the simulation was reversed to version without any implementation of the electric field. The effect of particles turning around is clearly independent of the electric field implementation.

Indeed, the same behavior was found for a particle in the CDC by Christian Wessel. Figure 11.6 shows an image from the `basf2` visualizer for the Belle II detector. The image shows the ionization done by the muon in cyan color, the blue hits are from electron ionization, presumably from the muon decay. The SVD is shown in orange.
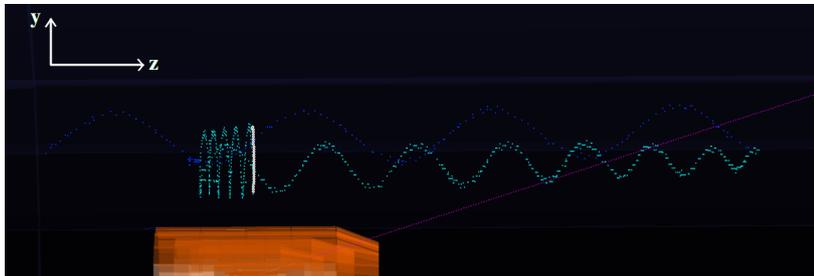
Figure 11.6: Back-turning particle observed in the CDC, indicating that this is not a problem with the TPC implementation. [40]

Here, again the particle unexpectedly turns around within the CDC. In the CDC this behavior can definitely not be explained with the electric field since the configuration is very much different to the TPC. In each wire cell of the CDC the electrical field points in direction of the amplification wire such that no homogeneous field occurs in the CDC. This leaves the origin of this process still unknown, as this is not a known bug with the GEANT4 simulation [37].

11.3.3 Pressure

Although multiple scattering is unlikely to be the source of the turn, as stated earlier, it is worth to investigate this a bit more. One way this can be done is by alternating the pressure of the gas in the

TPC volume. In case of very low pressure, there should be close to no scattering events with gas molecules. For this purpose, the simulation for a muon of 90 MeV transverse momentum was repeated with a pressure of 1 Pa and additionally with a pressure of 301 325 Pa to see the opposite effect. For the simulation at 1 Pa the work function of the gas had to be reduced drastically, since otherwise there would have been no hits in the TPC since no ionization can take place. This way, even though the average energy loss in each step was very small, it was sufficient to create large amount of hits.
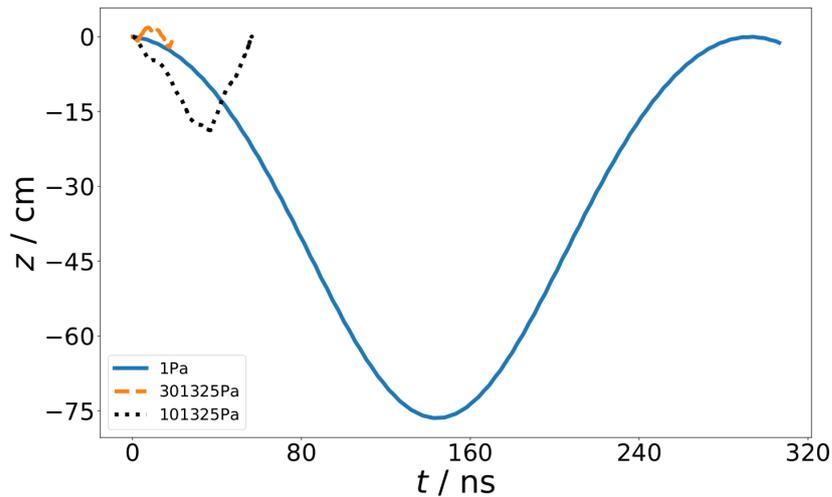
Figure 11.7: z vs. t for the same muon using different gas mixture pressures. Muon in 1 Pa turns back, even though there are no particles with which to scatter, indicating that the turn is a problem in the simulation.

Again, Figure 11.7 shows the z-coordinate plotted against time of energy deposit for simulations with different parameter values but same random-seed. Here, a clear separation between the cases can be observed. The muon in approximately triple operational pressure deposits energy very quickly and comes therefore relatively early to a stop. The muon in operational pressure of 1 atm lives considerably longer. It does experience a turn in its trajectory, but does not come close to the TPCs endplate.

The most interesting case is the muon in 1 Pa. The first thing to notice is that the muon is accelerated towards the endplate. Since there are close to no molecules in the TPC, this would have to be the effect of an electric field. However, here again the muon turns around. It is worth noting that the behavior of the z coordinate behaves like a sinusoidal curve as if there was an external alternating field applied to the detector, although there is no such field in Belle II. The particle reaches far in direction of the endplate and lives much longer than the others. The longevity is probably not accurate for a muon in these conditions, since the time it will take the muon to deposit all its energy very much depends on the work function of the field. For the simulation in 1 Pa the work function was reduced manually in order to see hits in the TPC. Therefore, it cannot serve as an accurate representation of the muons lifetime for this study. In reality, the muon would probably decay before it could deposit all energy.

That the same muon in atmospheric pressure turns around earlier than in 1 Pa could at first indicate that indeed scattering plays a role in the turn. However, opposed to that is the fact that the muon in 1 Pa turns around at all. So while scattering can play a role, it cannot be the only contribution.

11.4 Conclusion

The electric field was implemented in hopes to reduce the amount of hits introduced by micro-curlers. Instead, surprising behavior for low momentum particles was found. The cause for this is not clear, but since this is not a known physics effect, it must be a problem in the simulation. Since this behavior was found in the TPC as well as in the CDC it might be a problem with GEANT4 of with `basf2`. This hypothesis is supported by the simulation at low gas pressure.

It is not clear what effect this has on the amount of hits in the TPC. Not all particles turn around at the same coordinates and not all particles turn around at all. Therefore, it is difficult to quantify this effect. Clear is however, that the desired effect of having fewer hits by beam background micro-curlers cannot be guaranteed.

Since this is not a commonly known process, it might be worth investigating this further. However, this is out of scope for this study.

p_T Resolution

One important benchmark for the performance of the TPC and the upgrade proposal is the achieved p_T resolution σ_{p_T}/p_T, since the CDC plays a large part in reconstructing the transverse momentum p_T for charged particles. This value for various transverse momenta can be extracted for the TPC alone, or TPC+VTX which is the full upgrade proposal.

The p_T study with only TPC can be used to study the effects of electron efficiency and point resolution. Electron efficiency denotes which fraction of ionization electrons is registered as a hit, whereas the point resolution indicates with which spatial resolution the electron was registered.

When comparing the achievable p_T resolution with the Belle II detector performance the VTX is included in the simulation. This will also serve as study on which detector contributes how much to the overall p_T resolution.

12.1 Track Fitting

For this study, a simulation with 1 000 muons with fixed p_T was done, where the muons were created uniformly in θ in the range of 40 to 140°, which is approximately the acceptance where the muons reach the outer wall of the TPC provided they have enough transverse momentum.

In a fully implemented sub-detector the p_T resolution could be simulated by fitting a track to a track candidate from a pattern recognition algorithm. The fitted tracks would then be compared to ideal Monte Carlo tracks. A Monte Carlo track matcher would match the fitted tracks to the ideal tracks, check which tracks would have been found by the pattern recognition and calculate performance metrics like track finding efficiency, track finding purity, clone rate and fake rate. The p_T is estimated from the fit of the track.

For the TPC there does not yet exist a pattern recognition algorithm for finding tracks. Therefore, the module which creates the ideal Monte Carlo tracks is used to emulate pattern recognition tracks. As a result, the matcher will find a perfect match for each track with perfect purity and fake rate. This also means, that the track fit to the ideal candidate is a best case scenario for a TPC track.

The value for the p_T resolution for one particular p_T is obtained by subtracting the true p_T value, `pt_truth`, from the fitted value for p_T, `pt_estimate`. In a histogram for 1 000 muons this resembles a Gaussian distribution, as seen as an example in Figure 12.1. A Gaussian function is then fitted to this histogram and the result for the width parameter and its uncertainty are used as σ_{p_T} and its
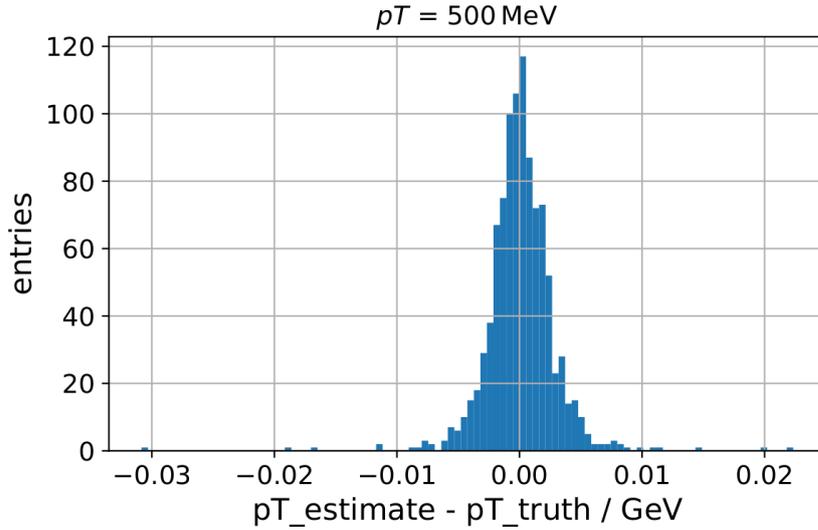
Figure 12.1: Distribution of `pt_estimate − pt_truth`. From a fit of a Gaussian function p_T resolution and its uncertainty can be obtained.

corresponding parameter uncertainty. To get the desired relative p_T resolution, these values are divided by the corresponding p_T value.

12.2 TPC-Only

As stated earlier, the p_T resolution is measured for various electron efficiencies and point resolutions. First, only the TPC is included in the simulation with no silicon detector in the inner region.

The electron efficiency emulates the geometry of the readout chip's active area as well as other losses, for instance recombination during drift. Those contributions are separated into different parameters. The parameter for the readout geometry ϵ_{ro} is kept fixed at a value of 0.81, while the other parameter ϵ is varied. The two parameters contribute to the total electron efficiency ϵ_{tot} as

$$\epsilon_{\mathrm{tot}} = \epsilon_{\mathrm{ro}} \times \epsilon$$

Throughout this study the term electron efficiency is used solely for the second parameter, since the total electron efficiency is secondary to this study. Separating the contributions of the electron efficiency allows for easier comparison to other readout strategies if the point resolution is known.

The altering of the point resolution is achieved by varying the pixel pitch[1]. The connection between spatial point resolution σ and pixel pitch d is [3]

$$\sigma = \frac{d}{\sqrt{12}}.$$

For the electron efficiency, values of 50, 75 and 95 % were chosen, and for the pixel pitches values of 50, 200 and 1 000 µm. In addition, the p_T resolution was also calculated for two more scenarios:

---

[1] Pixel pitch and size are identical in the simulation.

- *ideal*: ideal scenario with 100 % electron efficiency, no diffusion and close to no digitization (discretization of coordinates due to pixel size), realized with a pixel pitch of $\sqrt{12}\,\mu m$

- *idealDiff*: similar to *ideal* with the only difference that diffusion is activated

In this case, *ideal* represents the optimal p_T resolution with `basf2` using this particular geometry of the TPC, whereas *idealDiff* represents an ideal detector with no limits on technology and cost.

12.2.1 Fixed Electron Efficiency with varying Pixel Pitches

Figure 12.2 shows the p_T resolution with an electron efficiency of 95 % for the selected pixel pitches. The curves follow the expected behavior from Figure 4.2. For large p_T, the p_T resolution rises linearly with p_T. For lower p_T values the contribution of multiple scattering (MS) starts to play a role. At very low p_T one can also see the effect of the p_T acceptance of the TPC which results in a reduced lever arm.

In Figure 12.2 the p_T resolution is also shown for the *ideal* and *idealDiff* cases, which both have a perfect "effective measurement resolution", meaning that they reoncstruct the coordinates of the ionization to high precision. Having those two cases helps to separate the effects contributing to the measurement resolution which is responsible for the linear rise. Comparing *idealDiff* to the *ideal* case shows the effect of diffusion on the measurement resolution. The *ideal* curve thus only shows the rise in the p_T resolution due to the increasing difficulty of reconstructing the curvature of an almost straight track. However, in Figure 12.2 this rise does not occur, since the momentum range is not large enough. This means the *ideal* curve actually shows the constant term of MS in the p_T resolution with a deterioration due to the reduced lever arm term at low p_T.

Looking at the p_T resolution for a TPC with physically possible operational parameters, one can see that the p_T resolutions for the pitches of 50 and 200 µm are on par with the resolution for *idealDiff*. These cases have comparable electron efficiencies and mainly differ in pixel pitch. This shows that the p_T resolution is only impacted by pixel pitch once the value exceeds the effect of diffusion. With a transverse diffusion coefficient of $84\,\mu m/cm^{0.5}$ and a maximal drift length of 242.69 cm the width of the diffusion cloud becomes 1 308.59 µm for electrons which start drifting at the forward endcap. For most particles the drift length is shorter. When using a pixel pitch of 1 000 µm the track needs a drift length of 141.72 cm for diffusion to become on the same order as the pixel pitch. This is about 3/5 of the TPC volume. Whereas for a 200 µm pitch the diffusion for track is larger starting with 5.67 cm, which is a much lower value, since it rises quadratically with the pixel pitch. This explains why a pixel pitch of 1 000 µm has a far worse resolution than the others.

12.2.2 Fixed Pixel Pitch with varying Electron Efficiencies

Figure 12.3 shows the p_T resolution with a pixel pitch of 50 µm for the selected electron efficiencies. One can clearly see the deterioration in p_T resolution performance with decreasing electron efficiencies. Therefore, for the readout of the TPC should aim for the maximally achievable electron efficiency.

12.2.3 Comparison to the CDC

The TPC performance on the p_T resolution can be compared directly to the CDC. Figure 12.5 shows the p_T resolution of the CDC for simulated muons, where no other sub-detector is simulated. The p_T
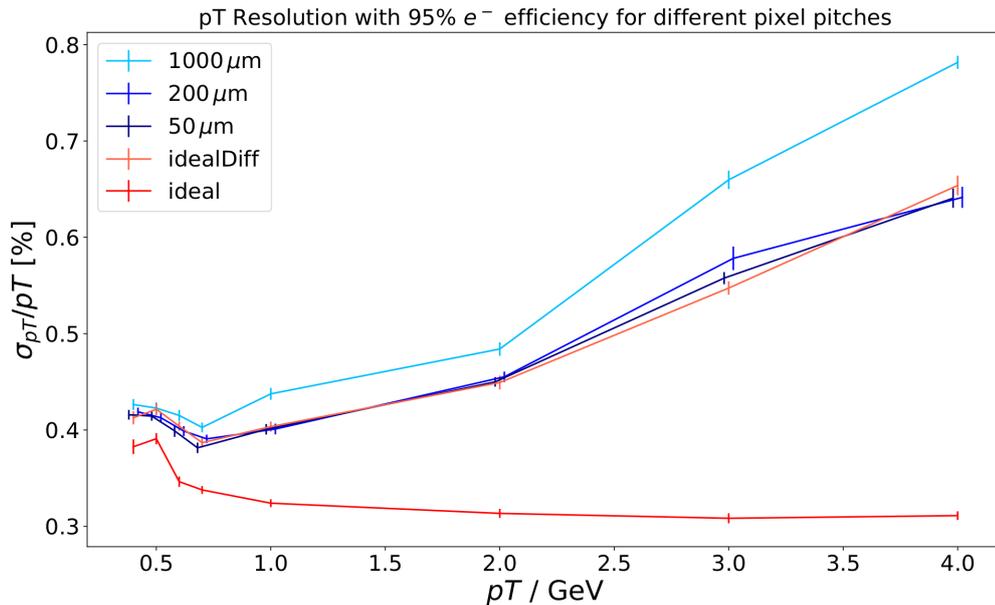
Figure 12.2: p_T resolution for varying pixel pitches and fixed electron efficiency compared to the *ideal* and *idealDiff* scenarios. The data points are slightly shifted with respect to the true p_T value for visualization purposes.
The *ideal* case has the best resolution. For low pixel pitches the p_T resolution is on par with the *idealDiff* case. Only for a large pixel pitch of $1\,000\,\mu\text{m}$ the p_T resolution becomes considerably worse. Staying below the effects of diffusion seems to be sufficient to achieve the best p_T resolution physically possible.

resolution for CDC is extracted identical to the TPC procedure, the track finding was also achieved by using the module which creates the ideal Monte Carlo tracks, in order to have a direct comparison to the TPC.

It is expected that the TPC performs worse in the measurement resolution term in the p_T resolution, since compared to the CDC the TPC should have two disadvantages with respect to the position measurement. For one, the spatial resolution of the TPC is limited by diffusion, whereas in the CDC diffusion does not play a large role. The effect of diffusion on the position measurement is illustrated by the *ideal* curve in the previous studies. Without diffusion the track fit is fitting directly to the trajectory of the muon thus achieving a high p_T resolution. For the *ideal* case the rise in p_T resolution due to uncertainties in reconstructing the curvature of an increasingly straight track at high p_T lies outside of the regarded momentum region.

Another disadvantage of the TPC is that it has a shorter lever arm than the CDC, because its inner radius is larger. This is illustrated in Figure 12.4. This leads to the fact that particles of same momentum have a shorter path in the TPC than in the CDC. Looking at Equation 4.4 one can see that the p_T resolution goes with (path length of the particle in the detector)$^{-2}$, meaning that the TPC should perform worse in the position measurement term of the p_T resolution.

In Figure 12.5 the CDC simulation is compared to the TPC in the same conditions (muons and no inner detector). The curve for the TPC the p_T resolution is shown for operational parameters of $50\,\mu\text{m}$ pixel pitch and $95\,\%$ electron efficiency, also shown is the *ideal* scenario for the TPC. One can see that
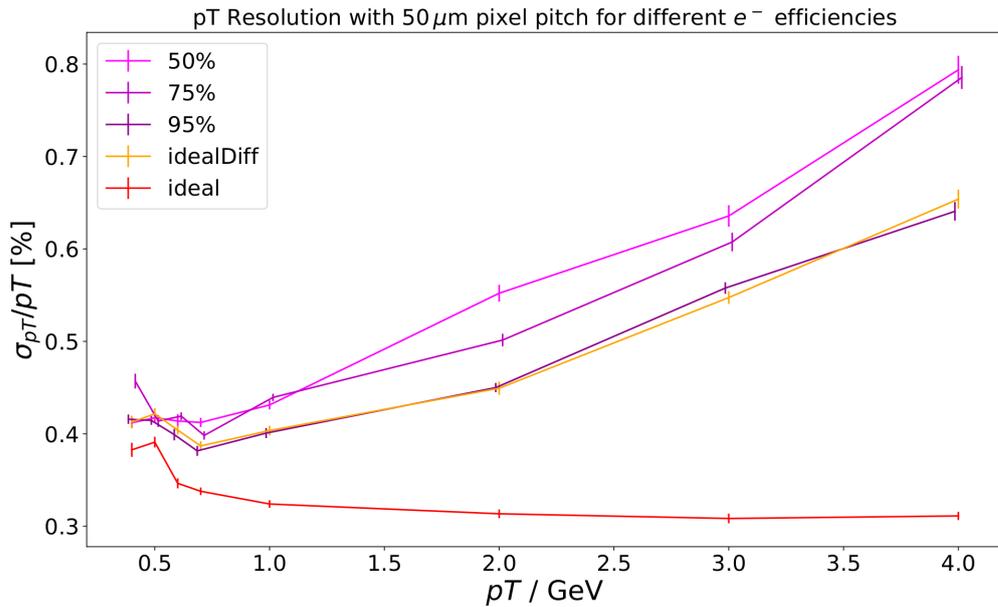
Figure 12.3: p_T resolution for varying electron efficiencies and fixed pixel pitch compared to the *ideal* and *idealDiff* scenarios. Again, the *ideal* case has the best resolution. With decreasing electron efficiency the deterioration in the p_T resolution becomes visible.

(a) $x - y$ projection of TPC

(b) $x - y$ projection of CDC [17]
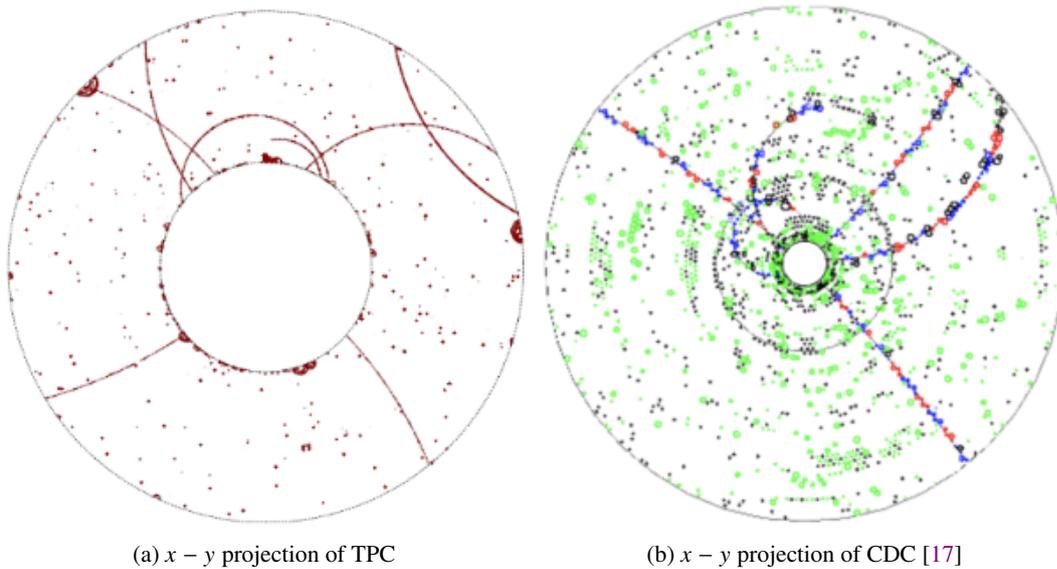
Figure 12.4: Showcase of the shorter lever arm of the TPC leading to worse p_T resolution. Inner region of TPC to be filled with VTX.

the values for the operational example do not reach the same level of p_T resolution as the CDC at low p_T, however they have similar values at large p_T.

Despite the disadvantages the TPC actually performs better in the position measurement term which can be seen by the more shallow rise compared to the steep rise of the CDC. The CDC mainly
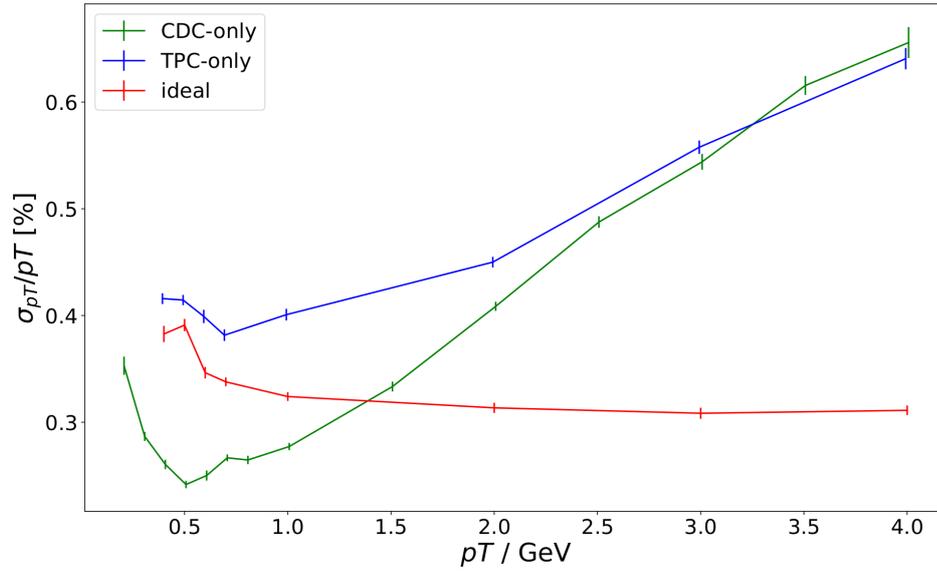
Figure 12.5: Comparison of p_T resolution for TPC-only with CDC-only. The CDC has a far better resolution at low p_T, mainly due to a constant multiple scattering term. They have a similar value at large p_T. Effect of diffusion on the position measurement can be seen by comparing to the *ideal* curve.

performs better due to a lower MS term. Partly this is contributed by a thinner wall for the CDC. The TPC vessel is simulated with aluminum of 2 mm thickness as inner wall, whereas the CDC consists mainly of 0.1 mm aluminum and 0.46 mm of carbon-fiber-reinforced polymers [49].

The thickness of the TPC walls will need to be investigated in a structural analysis, which is not in the scope of this thesis.

12.2.4 Conclusion

From the study of the p_T resolution it can be conducted that the size of the pixels in the readout should not exceed the width of a track after diffusion, while the electron efficiency should be targeted as high as possible. A pixel pitch of roughly 50 μm, as is the case for the Timepix3 chip [27], is more than sufficient to achieve the best physically possible transverse momentum resolution. However, also a pixel size of 200 μm would be sufficient and as sections 10.7.1 and 10.7.3 showed there is no downside in regards to hit efficiency. This pixel size would decrease the number of readout channels by a factor of 16.

The TPC alone does not match the p_T resolution of the CDC especially at low p_T, but performs overall better on the position measurement contribution. This performance might be enhanced by including the VTX as upgrade of the inner silicon detectors in the simulation, which is part of the upgrade proposal. The results can then be compared to the current Belle II detector, i.e., CDC+VXD. The MS should roughly stay the same since the VTX has a comparable radiation length as the VXD [40]. However, there could be a considerable contribution in the position measurement term due to the extension in the lever arm. The lever arm for CDC+VXD and TPC+VTX are then approximately equal. Therefore, the impact of the VTX on the p_T resolution is studied next.

Layer	r/cm
1	1.41
2	2.21
3	3.51
4	6.01
5	9.01
6	11.50
7	13.50
8	22.50
9	29.00
10	37.00

Table 12.1: Radii r of the VTX layers extended almost to the inner radius of the TPC

12.3 TPC + VTX

In this scenario the VTX was simulated with 10 layers, the radii are listed in Table 12.1. The TPC was simulated with a fixed pixel pitch of 50 μm and 95 % electron efficiency.

12.3.1 Comparison to TPC-Only

Including the VTX into the simulation increases the total lever arm of the tracking points from 64.95 cm to 108.19 cm. The effect on the p_T resolution can be seen in Figure 12.6. Mainly for high p_T particles the VTX improves the p_T resolution, while in the other regions it performs same or slightly worse. This is exactly the expected effect from MS and the longer lever arm.

12.3.2 Comparison to CDC+VXD

Comparing the TPC+VTX scenario to the CDC+VXD (Figure 12.7) the aforementioned effects of the VTX on the p_T resolution become even more apparent. There is little contribution at low p_T where the CDC mostly dominates in performance. At high p_T the extension of the lever arm due to the VTX greatly improves the resolution for the upgrade scenario with the TPC. That this improvement is mainly due to the contribution from the lever arm can be seen by comparing the p_T resolution to a CDC+VXD upgrade scenario. In this simulation the SL0 of the CDC and the VXD were replaced with a 7-layer VTX. This is not directly an competitor to the TPC upgrade, since SL1 and SL2 are also impeded at design luminosity, but it can give first hints for a possible CDC+VTX upgrade, where the first three superlayers are replaced.[2] In this scenario the VTX does not cause a shallower rise in σ_{p_T}/p_T.

12.3.3 Conclusion

The VTX contributes at high p_T to the p_T resolution such that better performance than the CDC is reached for the TPC above 2.5 GeV. At low p_T the MS term in the p_T resolution dominates. It is still unclear how large this term will be for the final TPC as this will have to be subject to a structural

---

[2] Simulating CDC+VTX with three superlayers removed was not practical within the scope of this thesis.
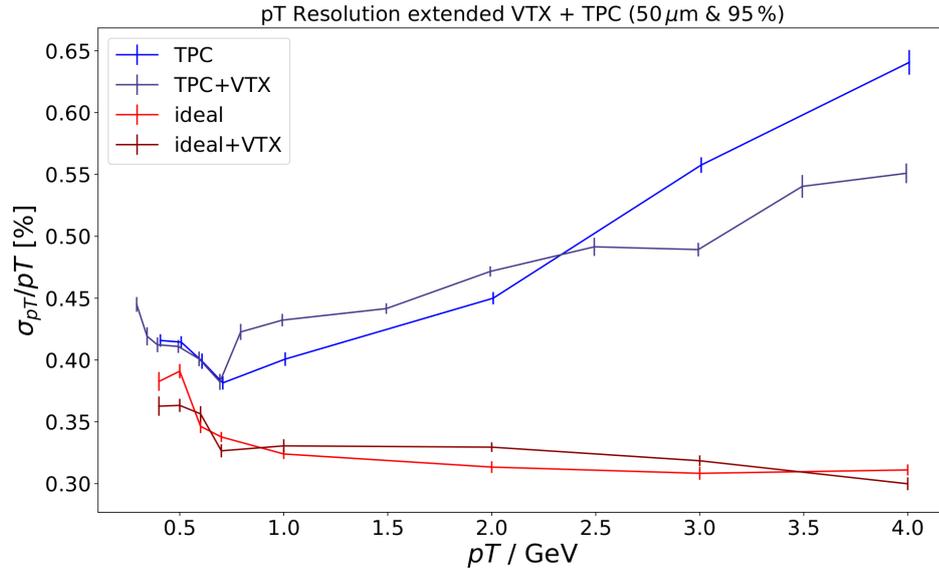
Figure 12.6: p_T resolution for TPC+VTX scenario compared to TPC-only case. VTX has a slight negative impact for low p_T particles, but improves resolution for higher p_T. The curves for *ideal* and *ideal* +VTX are consistent with each other. The VTX does not improve on the *ideal* case, since without diffusion the lever arm contribution lies outside of the regarded momentum range.
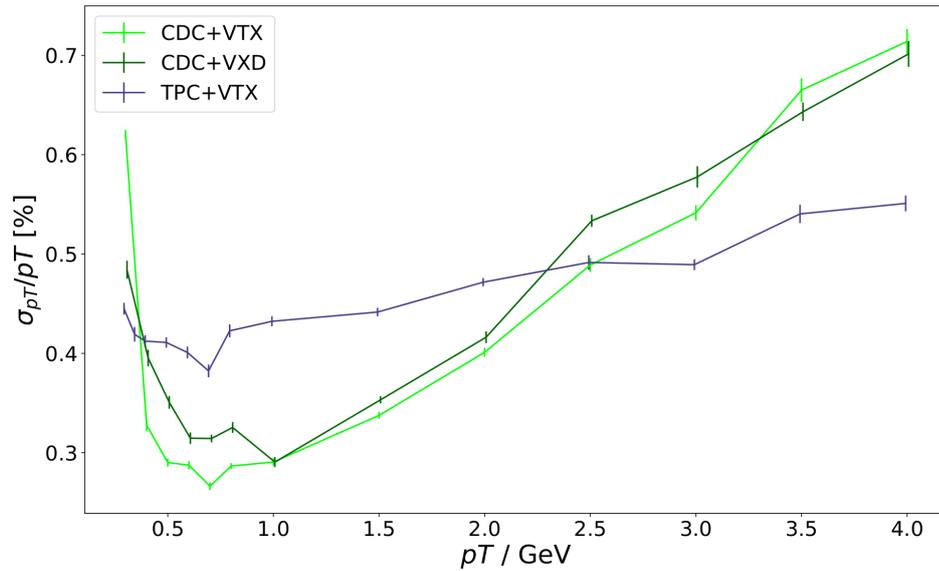
Figure 12.7: p_T resolution for TPC+VTX scenario compared to CDC+VXD and CDC+VTX. The extension of the lever arm due to the VTX causes a better p_T resolution for the TPC at high p_T.

analysis. Nevertheless, the TPC alone and especially TPC+VTX outperform the CDC(+inner silicon) in the intrinsic detector resolution.

This is the case when comparing the track fitting from Monte Carlo matched tracks. The p_T resolution performance using a TPC track finder is yet to be studied. However, the conditions for track
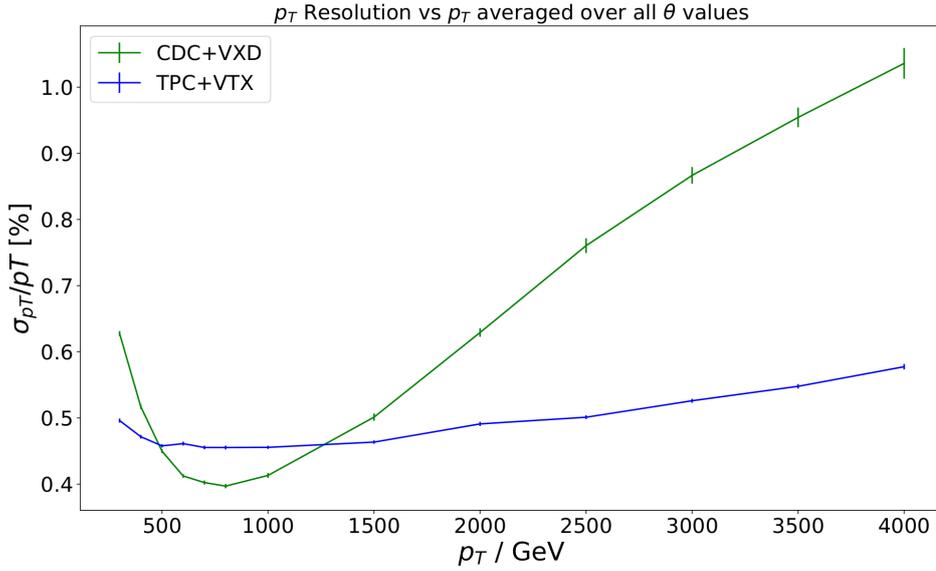
Figure 12.8: p_T resolution vs p_T for TPC+VTX compared to CDC+VXD averaged over all θ values. The shape of the curves is largely the same with a few deviations for the p_T resolution

finding in a TPC are favorable. Based on the results from the event overlap (section 10.4) it can be expected that it is rare for tracks to be directly intersected. Therefore, the TPC should excel in track finding for tracks from different events in the same volume. Due to the large amount of voxels a track finding algorithm should have no problems to separate two close tracks. This also means that the TPC should in principle have a good resolution for distinguishing tracks from different event in the same volume. Implementing a track finding algorithm should be one of the next steps for further studies of the TPC.

12.4 θ Dependence

Since the p_T resolution is impacted by diffusion, which depends on the drift length of the electrons, the p_T resolution can be investigated more in-depth for various θ values. For this purpose, the p_T resolution of the TPC+VTX was scanned over $p_T \in \{300, 400, 500, 600, 700, 800, 1000, 1500, 2000, 2500, 3000, 3500, 4000\}$ MeV and $\theta \in \{30, 45, 60, 75, 90, 105, 120, 135\}\,°$ for 1 000 muons for each combination. The same was done for CDC+VXD.

12.4.1 Averaged over one Parameter

First, one can compare the results from this simulation with the previous simulations where θ was distributed uniformly in $[40, 140]\,°$. This is achieved by averaging over all θ values for each p_T. The result of this can be seen in Figure 12.8. Overall, the shape of the p_T resolution stays the same compared to Figure 12.7, the values for σ_{p_T}/p_T are slightly changed presumably due to the use of different θ values.

This can also be done for averaging over p_T for the θ values. Here it is expected that for low θ values (forward region in Belle II) the resolution of the TPC is limited by the diffusion due to drift
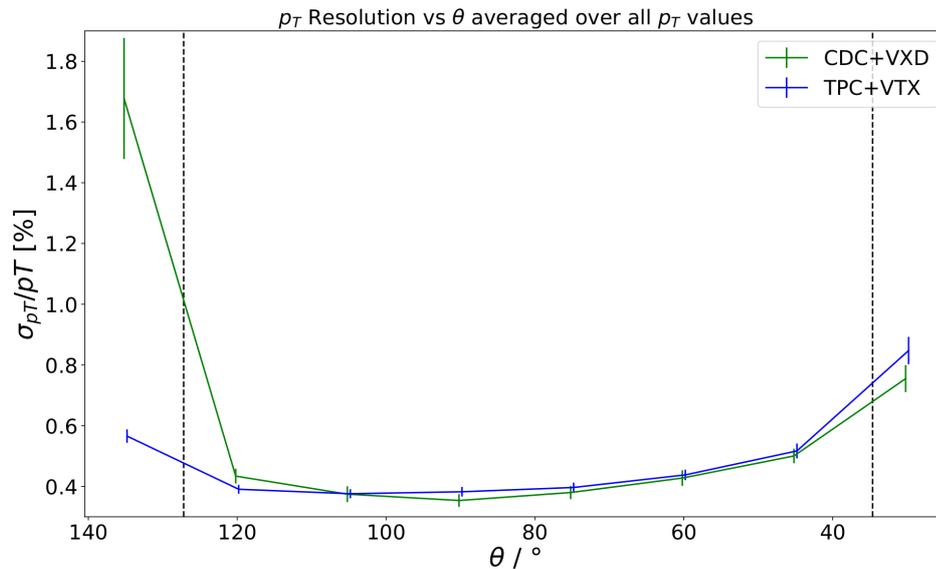
Figure 12.9: p_T resolution vs θ for TPC+VTX compared to CDC+VXD averaged over all p_T values. Outside the dotted lines is the region in which the muons exit the TPC through the endcap, thus not reaching the outer wall which causes a short lever arm. The x axis is inverted such that the forward region (low θ) is on the right side of the plot, consistent with preceding plots. Errors are multiplied with 10 for visualization.
The effect of particles leaving through the endcaps is visible. The effect of diffusion becomes apparent for the low θ tracks.

length. Figure 12.9 shows the p_T resolution as a function of θ averaged over p_T. The x axis is inverted such that the forward region of the Belle II detector is on the right side of the plot. The vertical lines represent the θ range for which particles with large enough momentum reach the outer wall of the TPC without leaving through the endcaps. For particles which do leave the TPC in forward or backward region the p_T resolution becomes notably worse. The same is true for the CDC which has an angular acceptance of $[17, 150]\,°$ in its inner region with slanted walls, but due to its geometry, the muons leave the chamber without reaching the outer superlayers. In the backward region (135°) the TPC performs better than the CDC, probably due to an excellent position measurement since there is almost no diffusion of the track. In forward region (30°) the TPC performs slightly worse, which might be the effect of diffusion.

For the θ values within the acceptance of the TPC[3] the does not seem to be a strong dependence on θ. The TPC performs on the same level as the CDC which does not have a θ dependence in its spatial resolution. Since it is not clear what causes this behavior, the θ dependence has to be investigated further.

12.4.2 Separating Parameters

The first way the θ dependence can be showcased is by plotting the p_T resolution vs. p_T for each value of θ individually. This is shown for the TPC+VTX in Figure 12.10. This plot also shows the

---

[3] Acceptance meaning here that the outer radius is reached provided the muon's p_T is large enough.
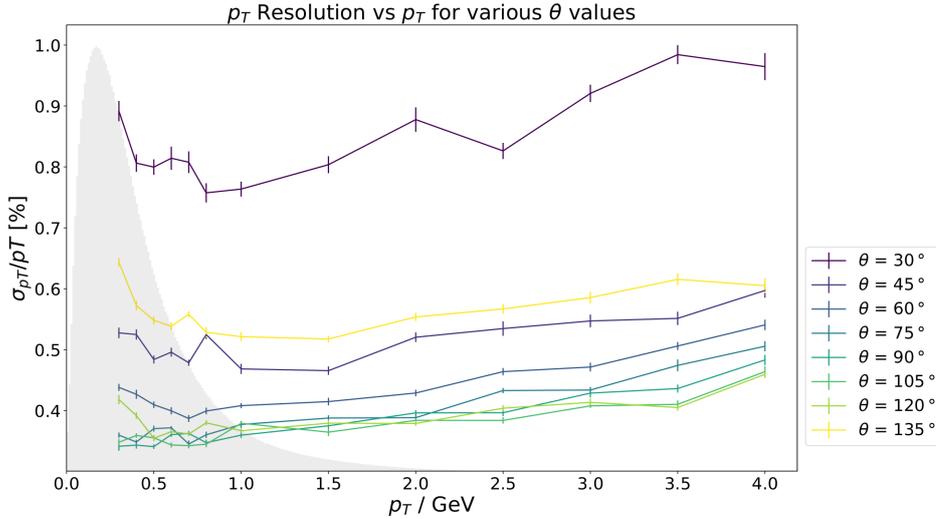
Figure 12.10: p_T resolution vs. p_T with individual curves for θ. Worst resolution is achieved for muons which exit through endcaps. Rise in p_T resolution for large p_T independent of θ. Therefore, it is likely that the lever arm dominates the position measurement term in the p_T resolution. The gray histogram shows the p_T distribution of stable charged particles from $\Upsilon(4S)$ events for $17° \leq \theta \leq 150°$.

distribution of p_T, which is expected in Belle II for stable charged particles in a θ acceptance range corresponding to that of the CDC. This histogram was created by simulating $1\,000\,000$ $\Upsilon(4S)$ events.

As indicated in Figure 12.9 the resolution is worst for tracks that exit the detector through one of the endcaps, whereas for the intermediate region the values are largely the same. It is interesting to see the linear rise of σ_{p_T}/p_T at large p_T independently of θ. This indicates that perhaps the diffusion of the track is not contributing all that much to the position measurement term in σ_{p_T}/p_T. This also means that it is mainly the lever arm which contributes to this term which is extended by the VTX. It is therefore unlikely that contribution can be improved upon. However, in the high p_T range not a large amount of particles is expected.

Figure 12.11 shows the p_T resolution as function of θ for all p_T values. In this plot the p_T resolution of the CDC+VXD as function of θ is also shown, averaged over the momenta 300 to 800 MeV since most particles are expected in this momentum region. Therefore, the performance of the TPC+VTX to this value is of great interest. Also shown is the θ distribution of charged stable particles from $1\,000\,000$ $\Upsilon(4S)$ decays.

As expected the resolution is worse for the largest p_T due to the smaller curvature of the track. However, it is worth noting the θ dependence is the same for all p_T. The θ dependence of the CDC curve is much stronger in this plot than in Figure 12.9. The only difference is that here only the low transverse momenta ($p_T \leq 800$ MeV) are averaged. This indicates that this θ dependence could be caused by MS. Indeed, one would expect a symmetric increase from MS around $\theta = 90°$ due to particles entering the chamber wall at an oblique angle instead of entering perpendicular such that the path is the material in increased by $1/\sin\theta$. For the CDC the θ dependence is indeed symmetric around $90°$ and only becomes asymmetric for the endcap region, which can also be seen in the data points listed in Table 12.2.

For the TPC the same behavior would be expected. However, the curves in Figure 12.11 do not show such a strong increase due to MS. Instead two effects can be seen. For one, the p_T resolution
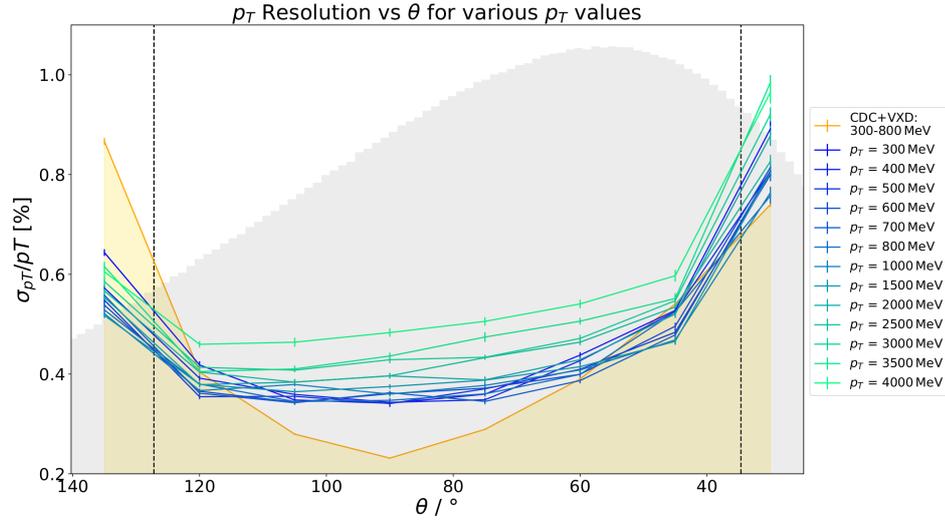
Figure 12.11: p_T resolution vs. θ with individual curves for p_T. Average for CDC+VXD for p_T below 900 MeV is also shown. Effect of MS is visible for the CDC, but does not have large impact on the TPC. More details in the text. The gray histogram shows the θ distribution of stable charged particles from $\Upsilon(4S)$ events.

$\theta/°$	$\sigma_{p_T}/p_T[\%]$
30	0.740±0.005
45	0.540±0.003
60	0.390±0.003
75	0.289±0.001
90	0.231±0.001
105	0.280±0.002
120	0.404±0.003
135	0.867±0.007

Table 12.2: Data points for the p_T resolution of CDC+VXD averaged over p_T for 300 to 800 MeV

is not symmetric around $\theta = 90°$, but is slightly slanted towards low θ. This is likely the effect of diffusion on the position measurement. At low θ the tracks are mainly in the forward region where the drift length becomes large.

The fact that the p_T resolution is not as significantly affected by the MS due to the angle as the CDC can be explained by the number of measurement points. For the CDC the number of data points stays largely in $\mathcal{O}(56)$ which is the number of wire layers. In the TPC however, the number of hits depends on the traversed volume. With a slanted track the number of hits increases by a factor of $1/\sin\theta$ compared to a track with $\theta = 90°$ (until the track intersects with the endcap), which is beneficial in reconstructing the position of a track at any given point. This is done by determining the charge density of ionization electrons perpendicular to the track direction. Due to diffusion this distribution should resemble a Gaussian to which a curve can be fitted to determine the mean position of the track. This is illustrated in Figure 12.12.
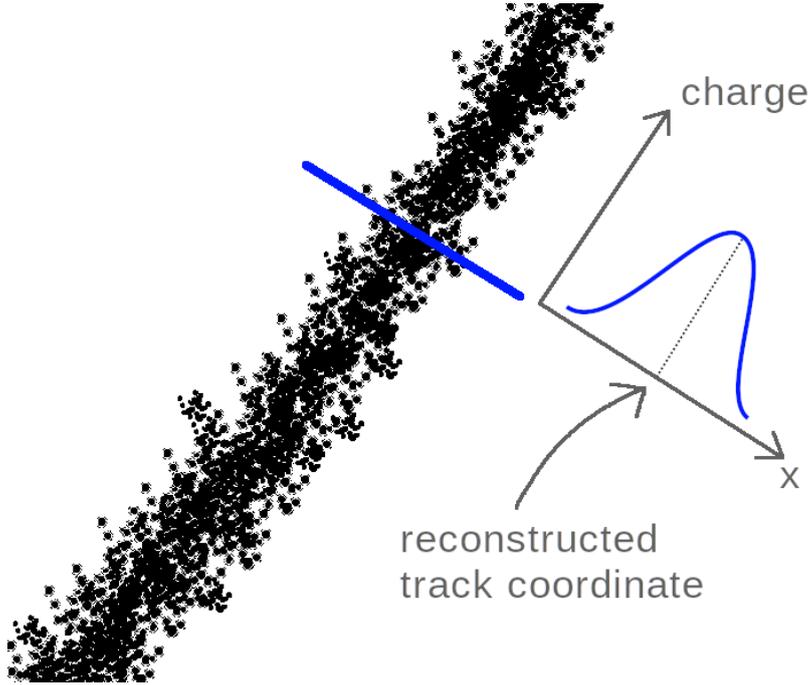
Figure 12.12: Reconstruction of a track position using the charge density perpendicular

The Standard Error on the Mean σ_μ (SEM) is then an estimate of the spatial resolution $\sigma_{r\phi}$ with which the track is reconstructed. It depends on the number of measurement points n via [50]:

$$\sigma_\mu = \frac{\sigma}{\sqrt{n}}$$

where σ is the width of the distribution, i.e., the track width. n increases with respect to a perpendicular track with n_0 hits via $n = n_0/\sin\theta$. From this and the fact that the track width depends on the drift length z_D, it follows:

$$\sigma_\mu \propto \sqrt{z_D \sin\theta}$$

The $\sqrt{\sin\theta}$ term is what causes an improvement at $\theta \neq 90°$ and effectively counteracts the MS contribution.

Since the track fit is only done with the first arc of the track, additional curling in the TPC does not yield a better momentum resolution of particles close to $\theta = 90°$ [40].

Figure 12.13 shows that for low p_T the effect of MS becomes larger which is consistent with the hypothesis that MS is responsible for the bowl-like shape in the p_T resolution.

In general, the TPC covers the θ range in which most particles are expected very well with regards to the p_T resolution. At the outer region, where fewer particles are expected, the resolution becomes worse due to particles exiting the detector through the endcaps.

Appendix C shows plots in which for each value of p_T and θ individually the p_T resolution performance is compared between TPC+VTX and CDC+VXD.
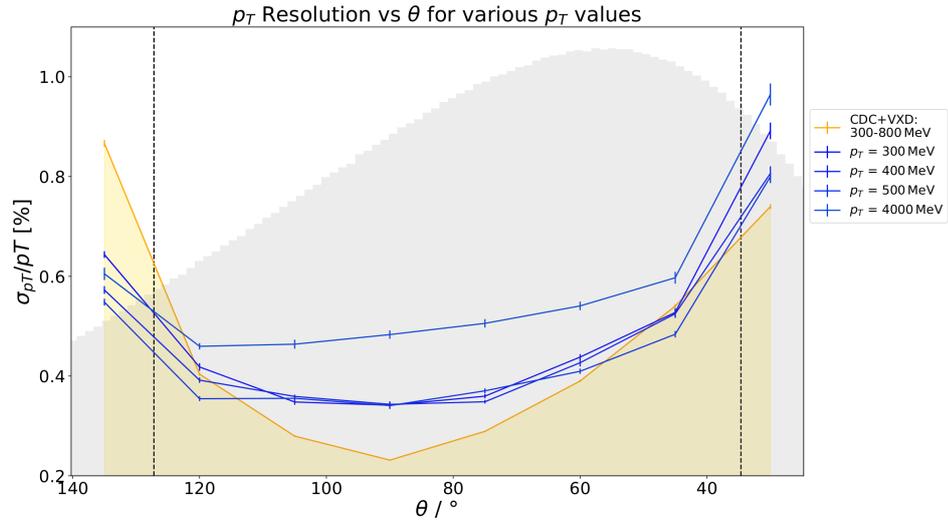
Figure 12.13: p_T resolution vs. θ with curves for low p_T values. Scattering effect becomes more dominant for low p_T particles.

12.5 Conclusion

It was shown that the p_T resolution of the proposed upgrade can perform on the same level as the current Belle II detector. In the intrinsic detector resolution for measuring the tracks, the TPC+VTX performs better than CDC+VXD and CDC+VTX. With a study on the θ dependence it could be shown that the resolution of the TPC is not limited by the drift length of a track. The observations for the θ dependence are consistent with expectations, however, in order to prove these hypotheses further studies are needed.

Readout Chip Requirements

The studies of p_T resolution of the TPC serve as first results for the parameters of a readout chip. These studies showed that a pixel pitch of 200 μm is sufficient which cuts down on the number of readout channels compared to Timepix3. Section 10.7.1 showed that the TPC can tolerate several μs of pixel dead-time while still operating at high hit efficiency.

With a threshold passing time resolution of 25 ns a z resolution of $\sigma_z = 2$ mm can be achieved (based on the drift velocity of electrons in the T2K gas). This requires a clock of 40 MHz, which is comparable to existing readout chips [27].

The data throughput of the TPC is a large concern due to the high amount of pixels. Initially, is was assumed that the TPC would operate in continuous readout in anticipation of the event overlap. To calculate the produced data rate in this case, one needs the amount of hits per second which are expected in the TPC. For this, the results of section 10.6 for the number of hits in 30.75 μs (one TPC volume) can be used. Using 2.5×10^6 for this value, the number of hits per second is 8.13×10^{10}.

The number of bytes per hit can be estimated by using the layout of Timepix3 which has 256×256 pixels on one chip with 55 μm pixel pitch [27]. Therefore, 1 byte is sufficient for each x and y coordinate, using 200 μm pixels. Assuming that the position of readout board is programmed into the Field Programmable Gate Array (FPGA) of the board, only 2 B are then needed for the entire $x - y$ information. With $\sigma_z = 2$ mm and a maximal drift length of 2 426.9 mm at least 2 B are needed to encode the z information (1 214 possible voxel IDs). In total that makes 4 B for the position of the hit. Including 1 B for safety, this amounts to 4.06×10^{11} B s^{-1} or roughly 379 GB s^{-1}. This quick calculation was done without including the effect of the `SimpleBackgroundRejection`. Using the number for hit efficiency and background rejection efficiency from section 10.7 (0.75 and 0.93 respectively) this number reduced to around 6.5 GB s^{-1}. With an improved background rejection this can even be reduced further.

Assuming a triggered readout the same calculation can be done for a trigger rate of 30 kHz (maximal design rate for Belle II [16]). With 30 000 triggers per second and a TPC maximal drift time of 30.75 μs the total amount of drift time to be read out by the TPC in 1 s is 0.9225 s. This means that compared to the continuous readout the data throughput only decreases slightly to 349 GB s^{-1} without and 6 GB with the `SimpleBackgroundRejection` assuming that there is no overlap between the drift volumes, which could potentially reduce the data throughput further.

A data throughput of around 6 to $7\,\mathrm{GB\,s^{-1}}$ for the TPC is comparable to the $7.2\,\mathrm{GB\,s^{-1}}$ data throughput of the PXD [16]. While there are further data reduction steps for the PXD, this shows that the data throughput of the TPC is feasible.

Conclusion

Overall, these studies have shown that a tracking TPC is a viable candidate for a new tracker in case the CDC performance is compromised by beam background in the future. The dE/dx resolution offered by the TPC looks promising in first studies (section 9.1). The loss of dE/dx information for low momentum particles which do not reach the TPC due to its larger inner radius compared to the CDC can be compensated for with the STOPGAP detector described in Appendix A, which can also act as a replacement for the CDC trigger.

The tracking conditions for the TPC regarding the overlap between events is still manageable, based on the result for the number of tracks in one TPC volume belonging to untriggered events from section 10.4. The filtering of beam background hits works effectively, since beam backgrounds mainly produce micro-curlers which are easy to identify. A first simple algorithm for rejection shows that many hits can already be discarded at the hardware level (section 10.7). Remaining beam background hits should be very easy to reject in online analysis. Using the simple method of rejection still comes at a cost of hit efficiency. It should be investigated if the rejection can be optimized with respect to hit efficiency. There might be an additional improvement if the amount of hits created by beam background can be reduced, either by studying the effects of the electric field in a suited simulation environment or by investigating if shielding against beam background is possible for the TPC. Once a track finding algorithm is created, which should be one of the next steps, it is possible to verify the expectation that intersecting tracks are rare such that differentiating between tracks from different events should be unproblematic. A method for assigning a track to the correct event by using the diffusion width of the track, which should be part of the track finding algorithm, has been outlined in section 10.5.

Chapter 12 shows promising results in the p_T resolution performance of the TPC. In the measurement resolution term in σ_{p_T}/p_T it performs better than the CDC despite diffusion and a shorter lever arm. Including the inner silicon detectors in the simulation of both gaseous chambers improves the achieved p_T resolution of the TPC more than for the CDC due to a greater extension of the lever arm. The constant multiple scattering term in the p_T resolution is yet to be a subject of an in-depth structural study, which might cause an improvement to the p_T resolution. In a study it could be shown that the p_T resolution performance of the TPC is not limited by the drift length of the track. The TPC shows a weaker θ dependence than the CDC due to effects which counteract a deterioration of performance at θ outside the region of 90°. While this agrees with expectations, further studies are needed to confirm the reasons given in section 12.4.

First requirements on the TPC readout could be set in this thesis. It was shown that a pixel pitch of 200 µm is sufficient for reaching high p_T resolution while having no considerable downside regarding hit efficiency due to pixel dead-time. In the current simulation the calculated ion density in the drift volume seems to stay within reasonable limits, however, this should be validated once the amount of beam background hits has been confirmed. These new results should shine a light on the question of gating for the readout of the TPC. If the ion density stays in the same order of magnitude it should be possible to operate the TPC in continuous readout, however, this has to be confirmed by a study using a simulation specialized on charge transport and electric field distortions due to space charge. An estimate for the data throughput in chapter 13 shows that the rate stays within reasonable limits, assuming the background rejection is implemented at hardware level.

A simulation anomaly currently prevents further studies on the beam background. An effort is made to present this problem to the collaboration. It should be possible to determine whether this is a `basf2` or GEANT4 problem by implementing a gaseous detector in stand-alone GEANT4. Unfortunately this was out of scope for this study.

Apart from the aforementioned studies which are still remaining, one of the next steps for investigating the tracking TPC should be to implement the event overlay into `basf2`, since having it in stand-alone code makes it difficult for other people to validate. Additionally, it is generally not desirable having to maintain code in two different places.

In general, there is plenty of reason to be optimistic about a tracking TPC for Belle II. Since the TPC is a very large-scale project, the Tracking TPC team will need significant extension in personnel and funding in order to make the project feasible by 2030.

Bibliography

[1] https://en.wikipedia.org/wiki/Standard_Model, [Online; Date: August 2021]
     (cit. on pp. 3, 4).

[2] P. D. Group et al., *Review of Particle Physics*,
     Progress of Theoretical and Experimental Physics **2020** (2020), 083C01, ISSN: 2050-3911,
     eprint: https://academic.oup.com/ptep/article-
     pdf/2020/8/083C01/34673722/ptaa104.pdf,
     URL: https://doi.org/10.1093/ptep/ptaa104 (cit. on pp. 5, 6).

[3] N.Wermes, H.Kolanoski, *Particle Detectors*, Springer, 2020
     (cit. on pp. 5, 8, 9, 16–18, 20, 21, 48, 55, 64).

[4] V. Bertacchi et al., *Track finding at Belle II*,
     Computer Physics Communications **259** (2021) 107610, ISSN: 0010-4655,
     URL: http://dx.doi.org/10.1016/j.cpc.2020.107610 (cit. on pp. 6, 15, 31).

[5] B. Abelev et al., *Production of K∗(892)0 and φ(1020) in pp collisions at $\sqrt{s}$ = 7 TeV*,
     The European Physical Journal C **72** (2012), ISSN: 1434-6052,
     URL: http://dx.doi.org/10.1140/epjc/s10052-012-2183-y (cit. on p. 6).

[6] N.Wermes, B.Ketzer, *Physics of particle detectors*, lecture, 2018/2019 (cit. on pp. 7, 9, 10).

[7] https://openpress.usask.ca/physics155/chapter/8-3-motion-of-a-charged-
     particle-in-a-magnetic-field/, [Online; Date: August 2021] (cit. on p. 7).

[8] W.Demtröder, *Experimentalphysik 1*, Springer, 2005 (cit. on p. 9).

[9] E. Kou et al., *The Belle II Physics Book*,
     Progress of Theoretical and Experimental Physics **2019** (2019), ISSN: 2050-3911,
     URL: http://dx.doi.org/10.1093/ptep/ptz106 (cit. on pp. 11, 37, 38).

[10] K. Akai, K. Furukawa and H. Koiso, *SuperKEKB collider*,
     Nuclear Instruments and Methods in Physics Research Section A: Accelerators, Spectrometers,
     Detectors and Associated Equipment **907** (2018) 188, ISSN: 0168-9002,
     URL: http://dx.doi.org/10.1016/j.nima.2018.08.017 (cit. on pp. 11, 12, 37, 40).

[11] T. Browder, *Snowmass 2021 Letter of Interest: Belle II/SuperKEKB Upgrades and Overview*,
     https://www.snowmass21.org/docs/files/summaries/AF/SNOWMASS21-
     AF5_AF0_T.Browder-106.pdf, 2021 (cit. on pp. 11, 40).

[12] https://cerncourier.com/a/kek-reclaims-luminosity-record/,
     [Online; Date: August 2021] (cit. on p. 11).

[13] https://www.belle2.org/, [Online; Date: July 2021] (cit. on p. 12).

[14] I. Adachi et al., *Detectors for extreme luminosity: Belle II*,
Nuclear Instruments and Methods in Physics Research Section A: Accelerators, Spectrometers,
Detectors and Associated Equipment **907** (2018) 46, Advances in Instrumentation and
Experimental Methods (Special Issue in Honour of Kai Siegbahn), ISSN: 0168-9002,
URL: https://www.sciencedirect.com/science/article/pii/S0168900218304200
(cit. on pp. 12, 22).

[15] Y. T.Hara T.Kuhr, *Belle II Coordinate System and Guideline of Belle II Numbering Scheme*,
https://indico.mpp.mpg.de/event/2308/contributions/4092/attachments/
3414/3799/Belle2NumberingScheme.pdf, [Online; Date: August 2021], 2011
(cit. on p. 12).

[16] T. Abe et al., *Belle II Technical Design Report*, 2010,
arXiv: 1011.0352 [physics.ins-det] (cit. on pp. 12–15, 22, 23, 40, 77, 78).

[17] P. Rados, *Performance of Belle II tracking on collision data*,
https://indico.cern.ch/event/773049/contributions/3474751/attachments/
1940572/3217515/Belle2_TrackPerf_CHEP_7Nov2019.pdf,
24th International Conference on Computing in High Energy and Nuclear Physics, 2019
(cit. on pp. 14, 38, 67).

[18] N. Taniguchi, *CDC operation*, Belle II General Meeting, Presented on 04. 02. 2021, 2021
(cit. on p. 15).

[19] C. Niebuhr, *Summary from CDC task force*, Upgrade Working Group Meeting,
Presented on 20. 05. 2021, 2021 (cit. on pp. 15, 16).

[20] N. Taniguchi, *Report on Gain Degradation*, CDC Task Force Meeting,
Presented on 06. 07. 2021, 2021 (cit. on p. 16).

[21] P. Lewis, private communication (cit. on pp. 16, 54).

[22] M. Ball et al., *Technical Design Study for the PANDA Time Projection Chamber*, 2012,
arXiv: 1207.0013 [physics.ins-det] (cit. on p. 17).

[23] V. Lepeltier, *Review on TPC's*, Journal of Physics: Conference Series **65** (2007) 012001,
URL: https://doi.org/10.1088%2F1742-6596%2F65%2F1%2F012001 (cit. on p. 19).

[24] https://flc.desy.de/tpc/basics/gem/index_eng.html, [Online; Date: July 2021]
(cit. on p. 20).

[25] J. Adolfsson et al., *The upgrade of the ALICE TPC with GEMs and continuous readout*,
Journal of Instrumentation **16** (2021) P03022, ISSN: 1748-0221,
URL: http://dx.doi.org/10.1088/1748-0221/16/03/p03022 (cit. on pp. 18, 22).

[26] G. Charpak et al., *Micromegas, a multipurpose gaseous detector*, Nuclear Instruments and
Methods in Physics Research Section A: Accelerators, Spectrometers, Detectors and
Associated Equipment **478** (2002) 26, Proceedings of the ninth Int.Conf. on Instrumentation,
ISSN: 0168-9002,
URL: https://www.sciencedirect.com/science/article/pii/S0168900201017132
(cit. on pp. 18, 20).

[27] M. Lupberger, *The Pixel-TPC: first results from an 8-InGrid module*,
Journal of Instrumentation **9** (2014) C01033, ISSN: 1748-0221,
URL: http://dx.doi.org/10.1088/1748-0221/9/01/C01033
(cit. on pp. 19, 20, 28, 29, 33, 50, 52, 68, 77).

[28] Y. Iwasaki et al., "Level 1 Trigger System for the Belle II Experiment", vol. 58, 2010 1
(cit. on p. 21).

[29] B. Schwenker, *Upgrade of the vertex detector of the Belle II experiment*,
https://indico.cern.ch/event/995633/contributions/4259526/attachments/
2210850/3741618/schwenker-VXDupgrade-Belle2_v_1_2.pdf,
2021 International Workshop on Future Linear Colliders (LCWS2021), 2021
(cit. on pp. 22–24).

[30] J. B. Carlos Marinas,
Proposal of an all-layer monolithic pixel vertex detector for the Belle II upgrade,
https://confluence.desy.de/display/BI/Upgrade+EOI+Submission,
Expression of Interest, 2021 (cit. on p. 24).

[31] C. Wessel, *Optimisation of the data reduction for the Belle II pixel detector and tracking
studies for high luminosity operation of the SuperKEKB accelerator*, to be published,
PhD thesis: Physikalisches Institut, 2022 (cit. on pp. 24, 35, 50, 52).

[32] T. Kuhr et al., *The Belle II Core Software*, Computing and Software for Big Science **3** (2018),
ISSN: 2510-2044, URL: http://dx.doi.org/10.1007/s41781-018-0017-9
(cit. on p. 25).

[33] D. Y. Kim et al., *The simulation library of the Belle II software system*,
Journal of Physics: Conference Series **898** (2017) 042043,
URL: https://doi.org/10.1088/1742-6596/898/4/042043 (cit. on p. 25).

[34] L. Collaboration,
The Linear Collider Time Projection Chamber of the International Large Detector,
https://prc.desy.de/sites2009/site_prc/content/e38/e59184/e59185/
infoboxContent67368/tpc2010LOI17.pdf, Report to the DESY PRC 2010, 2010
(cit. on pp. 26, 50).

[35] T. Radermacher, *Measurements and simulation of drift gas properties for the time projection
chambers of the T2K experiment and for future neutrino experiments*,
PhD thesis: RWTH Aachen U., 2019 (cit. on p. 26).

[36] R. Diener, private communication (cit. on p. 26).

[37] J. Kaminski, private communication (cit. on pp. 27, 48, 51, 59).

[38] C. Pulvermacher and M. Feindt,
dE/dx particle identification and pixel detector data reduction for the Belle II experiment,
Presented on 01 06 2012, PhD thesis: Karlsruhe, KIT, 2012 (cit. on p. 32).

[39] A. Vogel, *Beam-Induced Backgrounds in Detectors at the ILC*,
PhD thesis: Departments Physik, 2008 (cit. on pp. 33, 35, 52).

[40] C. Wessel, private communication (cit. on pp. 38, 59, 68, 75).

[41] A. Paladino, *Background evaluation at SuperKEKB and Belle II*,
https://docs.belle2.org/record/1912/files/BELLE2-CONF-PROC-2020-008.pdf, 2020
(cit. on p. 44).

[42] A. Piwinski, *The Touschek effect in strong focusing storage rings*, (1998),
arXiv:physics/9903034: `physics/9903034` (cit. on p. 44).

[43] A. Fodor, *Design and Simulation of Beam-Background Monitors in the Vicinity of the
Electromagnetic Calorimeter for the Belle II Experiment*, McGuill University, 2017
(cit. on p. 45).

[44] A. Cortez et al., *Experimental ion mobility measurements for the LCTPC Collaboration*,
Nuclear Instruments and Methods in Physics Research Section A: Accelerators, Spectrometers,
Detectors and Associated Equipment **936** (2019) 451, Frontier Detectors for Frontier Physics:
14th Pisa Meeting on Advanced Detectors, ISSN: 0168-9002,
URL: `https://www.sciencedirect.com/science/article/pii/S0168900218316243`
(cit. on p. 49).

[45] F. Böhmer et al., *Simulation of space-charge effects in an ungated GEM-based TPC*,
Nuclear Instruments and Methods in Physics Research Section A: Accelerators, Spectrometers,
Detectors and Associated Equipment **719** (2013) 101, ISSN: 0168-9002,
URL: `https://www.sciencedirect.com/science/article/pii/S0168900213004166`
(cit. on pp. 49, 50).

[46] K. Wichmann,
Beam backgrounds: Simulation and Effects on Reconstruction at ILDReconstruction at ILD,
`https://bib-pubdb1.desy.de/record/90271/files/kwichmann_beijing10.pdf`,
International Linear Collider Workshop 2010, 2010 (cit. on p. 54).

[47] `https://geant4-userdoc.web.cern.ch/UsersGuides/ForApplicationDeveloper/`
`html/Detector/electroMagneticField.html`, [Online; Date: July 2021]
(cit. on pp. 55–58).

[48] S. Bacher, *Investigation of magnetic field inside Belle II spectrometer*, (2020) (cit. on p. 56).

[49] `https://github.com/belle2/basf2/blob/main/cdc/data/CDC.xml`,
[Online; Date: August 2021] (cit. on p. 68).

[50] D. G. Altman and J. M. Bland, *Standard deviations and standard errors*, BMJ **331** (2005) 903,
ISSN: 0959-8138, eprint: `https://www.bmj.com/content/331/7521/903.full.pdf`,
URL: `https://www.bmj.com/content/331/7521/903` (cit. on p. 75).

[51] O. Hartbrich, *Snowmass 2021 Letter of Interest: STOPGAP - a Time-of-Flight Extension for
the TOP Belle II Barrel PID System as a Demonstrator for Fast Timing CMOS Sensors*,
`https://www.snowmass21.org/docs/files/summaries/IF/SNOWMASS21-`
`IF3_IF0_Oskar_Hartbrich-192.pdf`, 2021 (cit. on p. 85).

[52] O. Hartbrich, *STOPGAP - a Time-of-Flight Extension for the TOP Belle II Barrel PID System
as a Demonstrator for Fast Timing CMOS Sensors*,
`https://indico.fnal.gov/event/46746/contributions/210525/attachments/`
`141361/178052/2021_03_22_CPAD_STOPGAP.pdf`,
CPAD Instrumentation Frontier Workshop 2021, 2021 (cit. on pp. 85, 86).

STOPGAP - a Time-of-Flight Extension for the TOP Belle II Barrel PID System as a Demonstrator for Fast Timing CMOS Sensors

The STOPGAP is a proposed extension for the TOP which is the PID detector of Belle II in the barrel region [51]. In its current mechanical design the quartz bars of the TOP leave gaps in azimuthal direction. These gaps account for 6 % of missing coverage, which is illustrated in Figure A.1. Additionally, particles which only traverse the edge of the bars experience a degradation in PID which effectively broadens the missing coverage to 7 %.
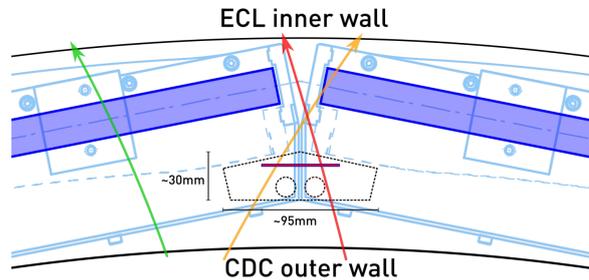
Figure A.1: Sketch of a possible STOPGAP instrumentation module between to bars of the TOP (blue) [51]

The Supplemental TOP Gap Instrumentation (STOPGAP) aims to recover the PID hermeticity by covering the dead area between the TOP bars with time-of-flight sensors. Due to limited space of installation one or multiple layers of silicon, with short signal collection time and excellent time resolution, are suited to fill the gap. Detailed studies on the STOPGAP have shown that the required time resolution is 50 to 70 ps for MIPs in order to separate pions and kaons in the typical momentum region of Belle II [52]. This may be achieved by novel fast Monolithic Active Pixel Sensors (MAPS).

Installing a STOPGAP double timing layer in the inner region of the detector instead of directly between the quartz bars could provide a trigger based on the time coincidence and reduce the fake trigger rate with respect to the current Belle II trigger (Figure A.2). Additionally, it can provide excellent pion/kaon separation for low p_T if installed in the inner region. Thus, the STOPGAP can make up for some of the shortcomings of the TPC: provide a trigger and recollect some PID for particles which do not reach the TPC due to low p_T.
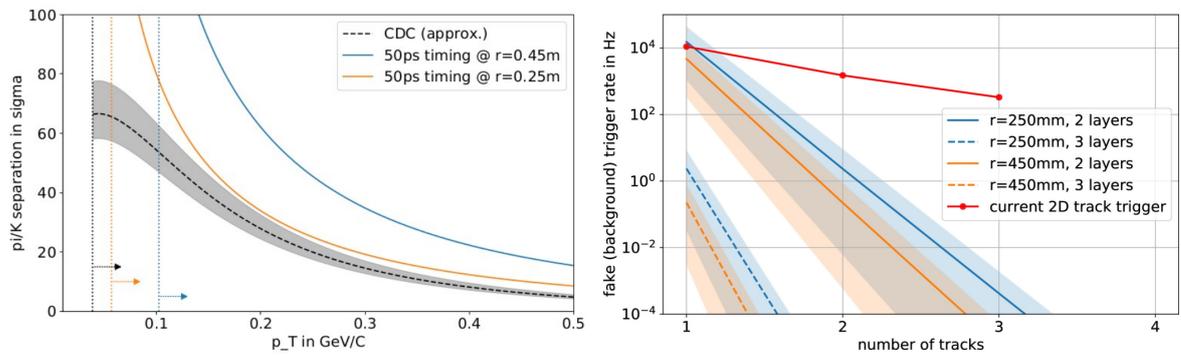
Figure A.2: Left: pion/kaon separation power for timing layers installed in inner region. Right: fake trigger performance of timing layers installed in inner region. [52]

Examples of Event Overlays without Beam Background

All events

All events

All events

All events

All events

All events
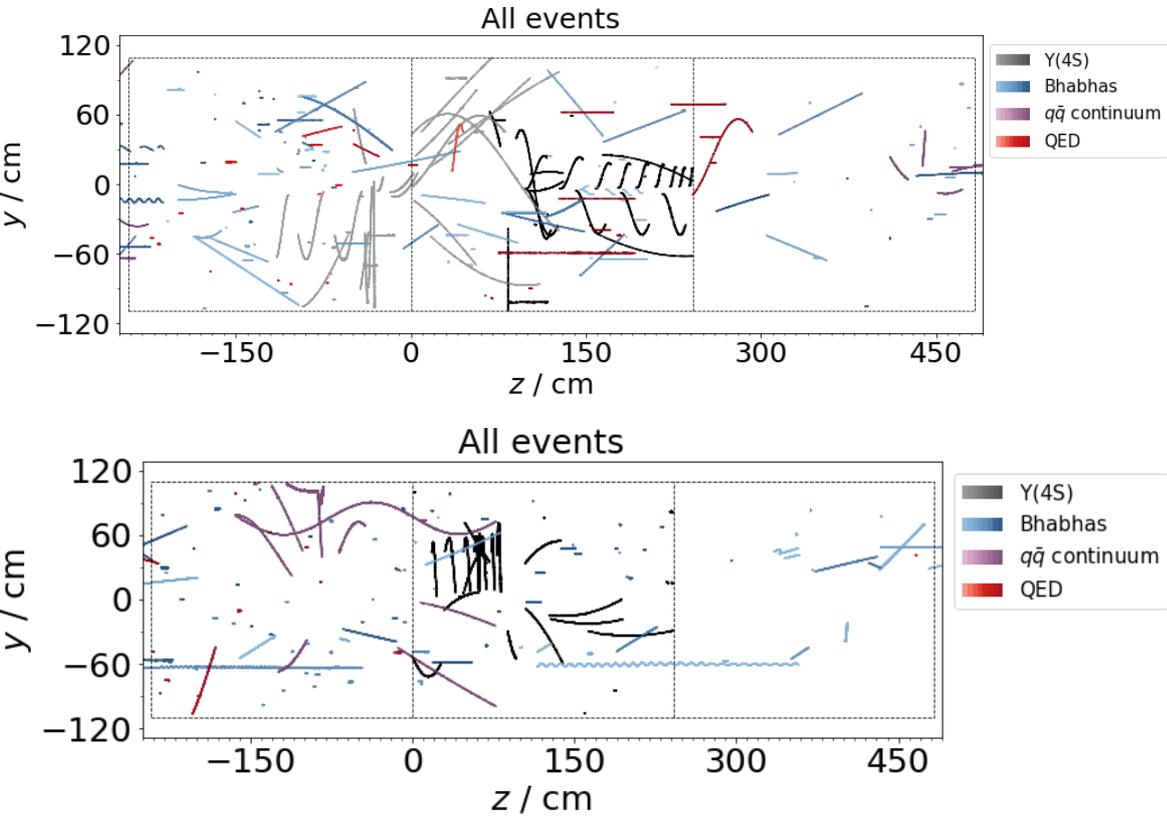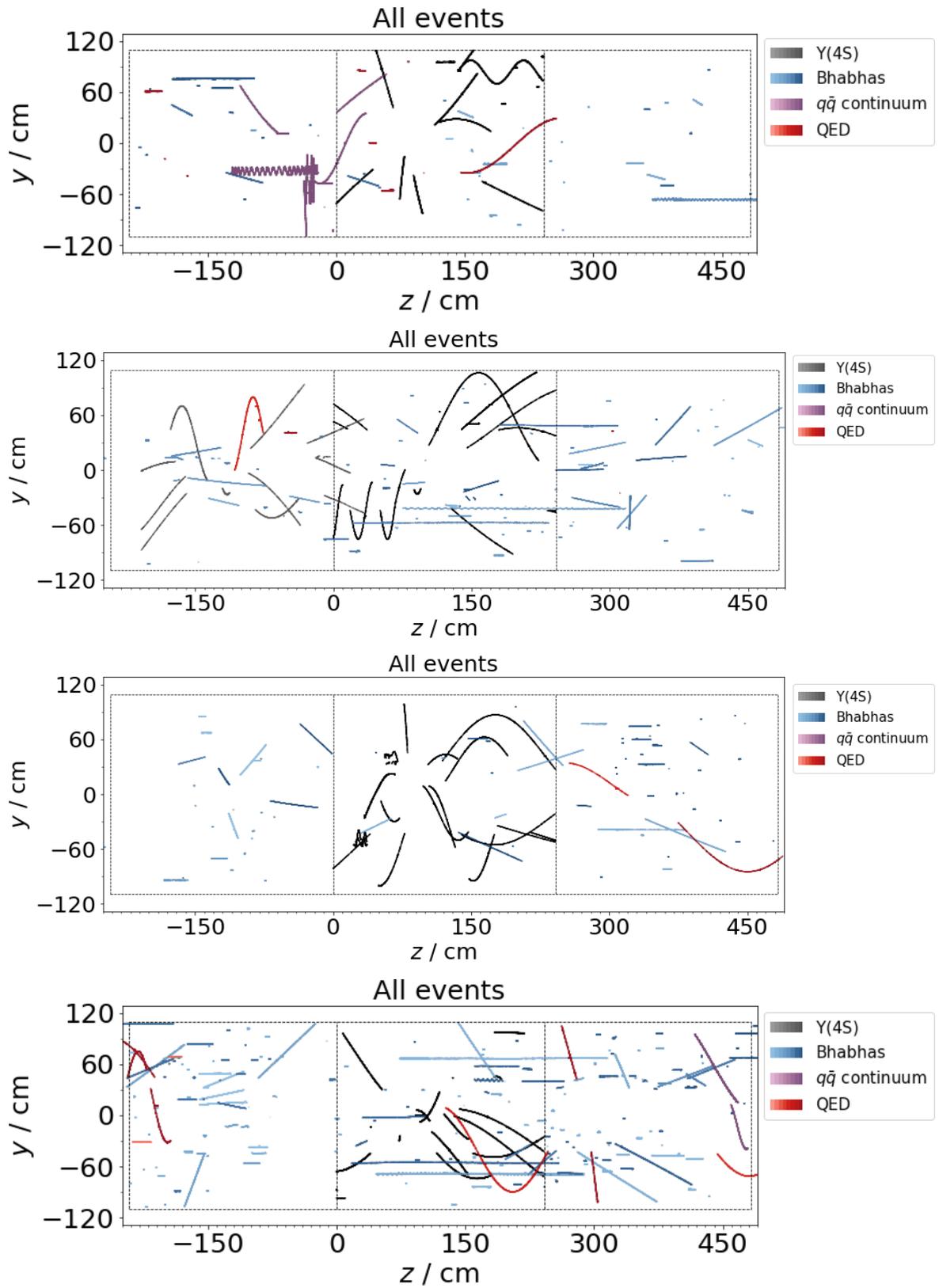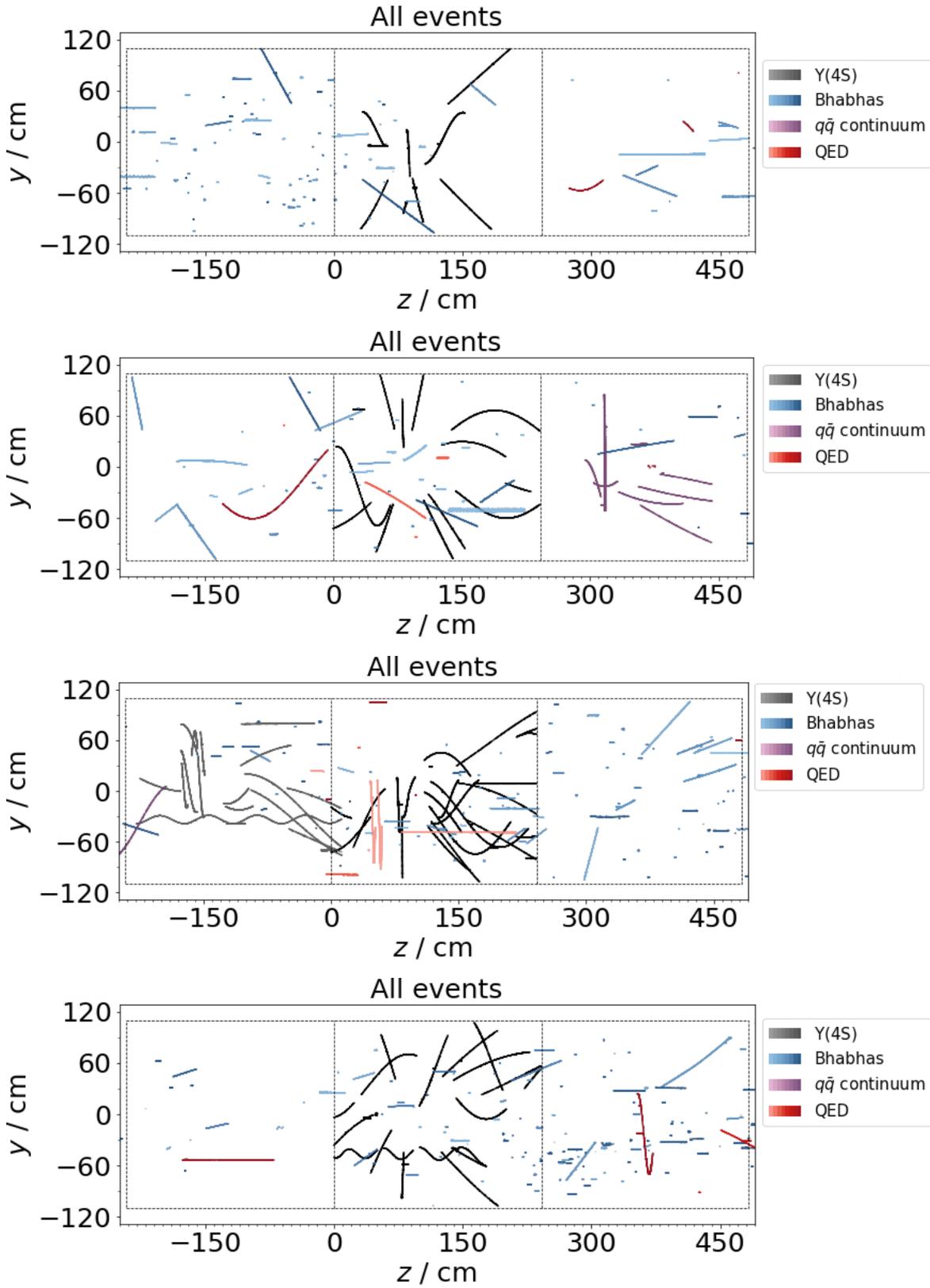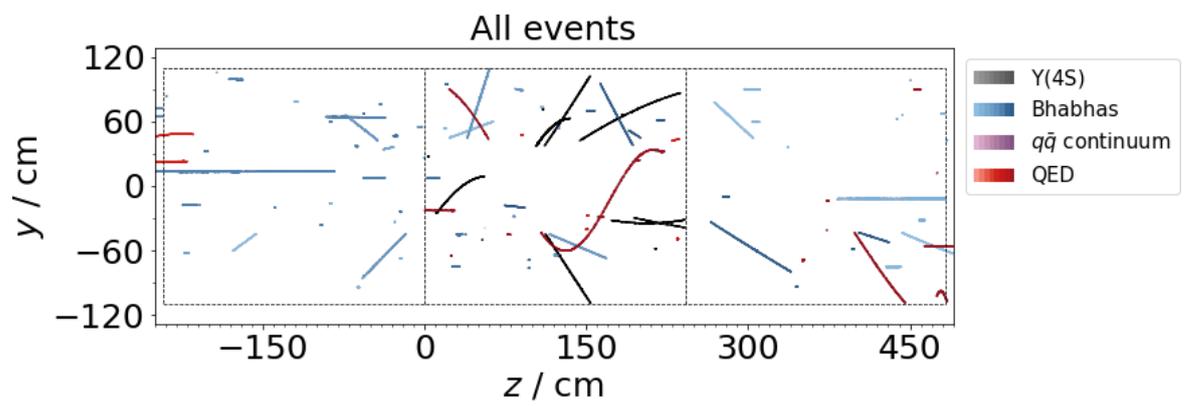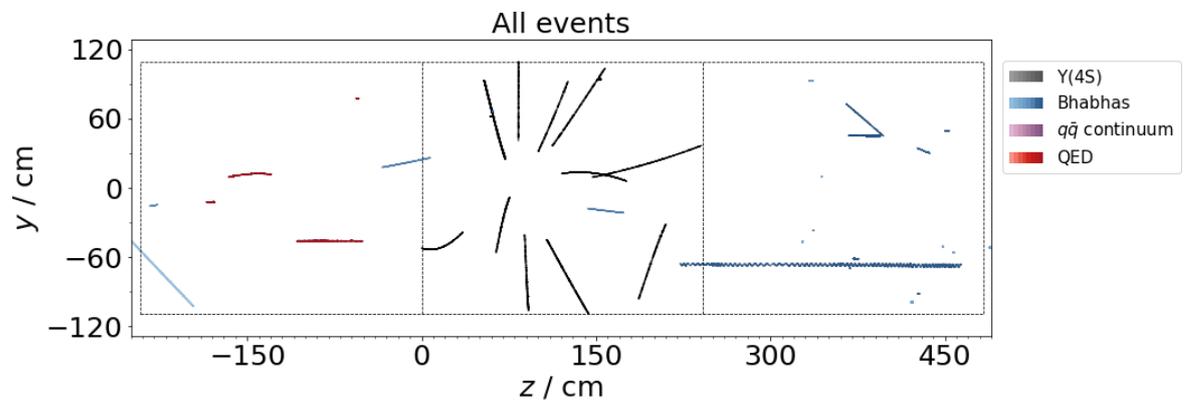
Comparison in p_T Resolution Performance between TPC+VTX and CDC+VXD for individual Parameters

C.1 p_T Resolution vs p_T for all θ

p_T Resolution vs p_T for $\theta = 45°$

p_T Resolution vs p_T for $\theta = 60°$

p_T Resolution vs p_T for $\theta = 75°$

p_T Resolution vs p_T for $\theta = 90°$

p_T Resolution vs p_T for $\theta = 105\,^\circ$

p_T Resolution vs p_T for $\theta = 120\,^\circ$

p_T Resolution vs p_T for $\theta = 135°$

C.2 p_T Resolution vs θ for all p_T

p_T Resolution vs θ for $p_T = 300\,\text{MeV}$

p_T Resolution vs θ for $p_T = 400\,\text{MeV}$

p_T Resolution vs θ for $p_T = 500\,\mathrm{MeV}$

p_T Resolution vs θ for $p_T = 600\,\mathrm{MeV}$

p_T Resolution vs θ for $p_T = 700\,\mathrm{MeV}$

p_T Resolution vs θ for $p_T = 800\,\mathrm{MeV}$

p_T Resolution vs θ for $p_T = 1000$ MeV

p_T Resolution vs θ for $p_T = 1500$ MeV

p_T Resolution vs θ for $p_T = 2000\,\mathrm{MeV}$

p_T Resolution vs θ for $p_T = 2500\,\mathrm{MeV}$

p_T Resolution vs θ for $p_T = 3000\,\text{MeV}$

p_T Resolution vs θ for $p_T = 3500\,\text{MeV}$

p_T Resolution vs θ for $p_T = 4000\,\text{MeV}$

List of Figures

List of Tables